INVERSE PROBLEMS, NON-UNIQUENESS AND SYMMETRIES IN GEOLOGY

Jie Xiao

Thesis Submitted for the Degree of

Doctor of Philosophy (PhD)

Department of Earth Sciences

Royal Holloway, University of London

July, 2020

Acknowledgements

I would like to express my sincere gratitude to my supervisor Prof. Dave Waltham who motivated me in geology, maths and coding. Though this unusual combination of skills was hard to achieved, the invaluable guidance, support and feedback he gave me has made things go smoothly throughout my PhD.

I am extremely grateful to my advisor Dr. Saswata Hier-Majumder for his vital assistance at all stages of my research and for his great efforts in initiating me to the areas of seismology and petrology. Dr. Benoit Tauzin of Australian National University and Prof. Yunpeng Wang of Guangzhou Institute of Geochemistry, Chinese Academic of Sciences are highly acknowledged for their contributions to the co-authored work presented here. Dr. Rebecca Fisher of my department and Prof. Gary Hampson of Imperial College London are acknowledged for their thorough examination of this work. A special mention goes to Dr. Mfon Udofia, who also looked at the problem of non-uniqueness during her PhD and whose thesis was a good start for my research.

Many thanks to Dr. Christina Manning and Prof. Martin King for participating as independent people in my annual review and/or MPhil to PhD upgrade meeting and offering critical inquiries and insightful comments. Thanks also to Prof. Jürgen Adam, Dr. Domenico Chiarella, Prof. Margaret Collinson, Prof. Javier Hernandez-Molina, Dr. Dave Lowry, Dr. Ian Watkinson and many others for the useful discussion on various aspects of geology and for the many pieces of advice for future career. I sincerely

appreciate the support from the technical and administrative staff in the department, in particular Ms. Julie Brown, Mr. Kevin D'Souza, Mr. Frank Lehane, Mr. Mark Longbottom, Mr. Dan Parsonage, Ms. Nisha Patel and Ms. Lynne White.

I would like to thank Prof. Martin Menzies who is an emeritus at Royal Holloway, University of London and Prof. Yigang Xu who is the head of Guangzhou Institute of Geochemistry, Chinese Academic of Sciences for establishing the RHUL-GIGCAS collaboration scheme by which my doctoral research was sponsored. I acknowledge my scholarship awarded by Chinese Scholarship Council. Many thanks to EU-FLOWS and NERC for their fabulous short training courses where I gained additional exposure to modelling, statistics and field research.

Thanks to my fellow postgraduate students: Kayode Adeoye-Akinde, Aalia Al-Shalan, Gavin Anthony, Ivan Antonov, Salim Ayomaya, Semra Bakkaloglu, Sandy Drymoni, Elham Jonade, Gerardo Gaitan, Alex Hughes-Wharton, Lucky Imagbe, Liang Liu, Zhi Lin Ng, Yasir Said, Yizhuo Sun, Paul-Ross Thomson, Seehapol Utitsan, Thomas Vandyk, Shuang Zhang to name a few. Thanks also to my close friends Xuanyu Chen, Arif Hussain Moosvi, Noah Okuonghae, Aidan Poles, Yunting Qi, Tat-in Tam, Xiangming Tao and Shuo Zhang.

Finally, I owe my deepest gratitude to my parents and my girlfriend Songshi Liang for their unfailing support and continuous encouragement throughout my years of study and throughout the way to approaching the degree. I love you!

Jie Xiao

Abstract

Most research in geology requires solving inverse problems. A geological inverse problem could be, for example, to extrapolate conditions in the past given limited observations today, or to unravel properties of the Earth's interior given incomplete measurements gathered at the surface. Unfortunately, inverse problems usually have non-unique solutions. However, these solutions are often linked by quite simple relationships even when problems are non-linear. These relationships express the symmetry for a problem since predictions are unaltered given proper changes in a solution obeying the rules. Symmetries are powerful tools since they enable an existing solution to be directly transformed into an alternative solution. This property leads to a novel inversion procedure based on numerical models, i.e. find a simple solution that produce the desired model and then have all additional solutions derived from the initial solution. Calculation of multiple solutions allows properties common to all solutions to be deduced and hence allows end-member hypotheses to be examined. Hence, it is possible to determine what is physically reasonable and what is not for an inverse problem, even though a unique solution is not available. The principle of symmetry is quite general and can be widely applied in various fields of geology. Synthetic and real-data examples presented in this thesis cover sedimentology, thermochronology and geophysics.

List of Illustrations

Contents

1 Introduction

Almost every aspect of geology involves an inverse problem. In general, an inverse problem is to interpret the cause of a particular effect, whereas a forward problem is to predict the effect of a particular cause. Two types of inverse problems are frequently encountered in geology. First, geological outcomes at present are observed and conditions in the past deduced. Secondly, measurements are gathered at the ground surface and structure at depth revealed. These are in stark contrast to experimental sciences, such as Physics, that involve the much easier forward problem of predicting outcomes given well controlled initial conditions. Inverse problems are not only inherently more difficult, but they suffer from the fundamental challenges of non-uniqueness and ill-conditioning as well. The non-uniqueness arises because more than one cause could give rise to the same effect, whilst the issue of ill-conditioning occurs as small errors in the observations produce large changes in the interpretation. The concepts of non-uniqueness and ill-conditioning were often confused in the literature. This thesis primarily deals with the former issue in the absence of errors. As will be shown in the later chapters, any inverse problem has non-unique solutions even if error-free data are available, though the problem of ill-conditioning makes this even more challenging (Tetzlaff, 2004).

Owing to advances in computer techniques, inverse problems frequently end up with quantitative models in practice. Compared to conceptual models that emerged

prior to the digital era, computer models are more quantitative as they are built upon mathematics of exact theories that prescribe the laws of geology. Using numerical techniques, the continuous functions are represented discretely in computers. Arguments associated with the functions are known as input parameters. Prediction of the end product in response to a set of input parameters is referred to as forward modelling. The reverse process of inverse modelling thus corresponds to the search of parameters that would generate the desired model to a good match with the reality. Though it is not unusual that a computer model fails to replicate the entire complexities of the real world, this is not an issue to worry about. All models are simplifications and no model can ever hope to match reality perfectly. The objective of this work is to determine the key controls that dominate the geological system, instead of more accurately visualizing the observations.

However, as Tarantola (2006) pointed out, a forward model can only exclude the parameter sets that are incompatible with the observations but not to identify the correct combination. Examination of a parameter set typically relies on an objective function (e.g. the root-mean-square error) that characterizes how well a model fits the observed data. A good-fit model can be generated by finding a local minima in the objective function, which is referred to as 'model optimization' (Press et al., 2007). Existence of solutions can be confirmed by finding at least one good-fit model. Failure to discovering any local minima is rarely the case. Instead, there are likely continuously connected regions of locally low values, forming a trough in the objective function. Each of the low value in the trough corresponds to a different solution that accounts

for a sufficiently good model. In addition, there may be may many such troughs in the objective function, leading to extra non-uniqueness in the inverse problem.

Though being aware of the non-uniqueness, geological studies still tend to seek particular solutions. Geologists are often (rightly) delighted to have found even one reasonable interpretation of their imprecise and incomplete data. For more quantitative problems, a single 'best' solution is often obtained by introducing additional constraints (e.g. the smoothest solution (Constable et al., 1987) to avoid over-interpretation of the results). Both of these ways attempted to solve an inverse problem by restricting a model until a single solution is found. Unfortunately, however, these are fundamentally wrong. As highlighted in Gubbins (2004), a solution should be predetermined by the knowledge upon which the model is built, rather than by the modellers' expectation. The ideas of using particular solutions to explain observed data have been criticised as long ago as late 19th century by Chamberlin (1890) who suggested, instead, the method of multiple working hypotheses.

In terms of computational geology, application of the multiple working hypotheses is referred to the discovery of multiple solutions to a single model. Calculating complete solutions for a model has remained challenging. The method of trial-and-error is frequently used for problem solving but can be slow and tedious when applied to real data. Likewise, an exhaustive search through all possibilities may seem straightforward but can be extremely time-consuming if not impossible. Optimization methods, such as gradient descent, are fast but can be easily trapped in local minima. Stochastic algorithms that generate and use random variables were

expected to find all solutions using tentative starting guesses. However, there has not been any published example ever succeeding. See Chapter 2 for more detailed discussion on inverse methods applied in specific geological problems.

This thesis approaches the issue of non-uniqueness by generating the whole set (or a representative ensemble) of possible solutions. This would be done through the principle of symmetry. In the same way that rotating a square by 90° leaves its geometry unchanged, a symmetry could be any operation on any object that preserves appearances. The operations and objects involved can be more abstract than rotation of geometric figures. For example, an important symmetry in physics is that its laws are unaltered by translation in time or space and by rotation of coordinates; these symmetries lead, directly, to the conservation of energy, momentum and angular momentum respectively (Noether, 1918). In the context of inverse modelling, a symmetry is any manipulation of a forward model's parameters that leaves the model output unchanged. In other words, symmetries specify trajectories in the parameter space that produce identical model outputs. A simple, frequently encountered, example is that model results are usually unaltered by the transformation $rate[i] \rightarrow a \cdot rate[i]$ ($i = 1, \ldots, N$), where N is the number of rates in the model) plus $time \rightarrow time / a$ where a is any constant, i.e. all processes are speeded up (or slowed down) by a constant factor and then the duration is altered to compensate.

The close relationship between non-uniqueness and a generalized concept of symmetry has been rarely applied in geology. An exception of these is a geochemical research undertaken by Waltham and Gröcke (2006) on the seawater Sr-isotope

fluctuations in the Early Jurassic, of which the multiple interpretations are similar to each other. Although the term ‘symmetry’ was not explicitly used, the correlation between multiple solutions can be thought of as an underlying symmetry. The rules of symmetry can enable a solution, once found, to be directly transformed into another solution that gives the same model. Using this insight, it is possible to derive all possible solutions given an initial solution. A significant advantage of the above geochemical problem is that it has analytic symmetry, i.e. the problem can be stated in a precise, mathematical form. However, an analytic symmetry only exists in simple problems and may not apply in complex, process-based models.

Nevertheless, as will be presented in this thesis, all inverse problems have symmetries; it’s just that these have to be revealed using numerical methods. To better understand non-unique inverse problems, a numerical method is proposed here for discovering, exploiting and utilizing their symmetries. The method is used to tackle inverse problems in three inverse problems from very different fields of geology. These are: a problem of interpreting sequence architectures, a problem of reconstructing thermal histories and a problem of evaluating mantle properties. Application of the symmetry method and resulting benefits in each specific inverse problem are demonstrated. Bringing the individual examples together shows the general applicability of symmetry concepts.

The remaining part of this thesis engages a literature review in Chapter 2 in order to provide context of the specific inverse problems to be explored and previous attempts to address these problems. Chapter 3 outlines the principle of symmetry and

its applications in numerical models. Chapters 4 to 6 present three published (or pending to submit) examples showing the symmetry method applied to a model of sequence stratigraphy, a model of thermal maturity and a model of mantle petrology. Chapter 7 consolidates the principle of symmetry and emphasizes how the method is superior to conventional methods. Finally, conclusions drawn from the theoretical and model work are presented in Chapter 8.

2 Literature Review

Extracting reliable information from the geological record, for example to better understand paleoclimate or structure of the Earth, depends on successful application of the inverse method. Geological data such as the sequence architecture of an outcrop, thermal indicators for a borehole or seismic travel-times are observed, and controlling factors deduced. However, inverse methods usually produce non-unique solutions because more than one set of parameters could account for identical results. Non-uniqueness is a fundamental issue that widely exists in geology. This chapter reviews the inverse problems where non-unique solutions arise. The literature discussed here covers three different aspects of geology (i.e. sedimentology, thermochronology and geophysics). A series of examples are discussed here for the purpose of providing an overview on key challenges to address later. The review focuses on the non-uniqueness in specific inverse problems and the strength and weakness of existing inversion schemes, in particular applications of quantitative modelling techniques.

2.1 Inverse Problems in Sequence Stratigraphy

Sequence architectures formed on continental margins are primarily determined by the sediment supply and accommodation (e.g. Schlager, 1993; Helland-Hansen and Gjelberg, 1994; Carvajal et al., 2009; Catuneanu and Zecchin, 2013). Interpreting stratal

geometries of sequence architectures observed on outcrops or seismic images corresponds to the studies of sequence stratigraphy (Vail, 1977; Posamentier et al., 1988). However, interpretations of stratal geometries are non-unique due to the difficulties in distinguishing individual effects of the dual controls (Posamentier et al., 1992). Other factors, for example the initial paleogeography (e.g. Uličný et al., 2002), extensional faulting (e.g. Hardy et al., 1994) and deltaic lobe switching (e.g. Ritchie et al., 2004), can also leave strong impacts on stratal geometries. These complications, if taken into account, can lead to additional possibilities and hence significantly extra non-uniqueness in interpretations.

Analogue and numerical experiments have shown that a variety of stratal patterns may be created in more ways than one. For instance, maximum flooding surfaces can be generated either by a decrease in the rate of accommodation availability creation or by a decrease in the rate of sediment supply (e.g. Schlager, 1993; Flemings and Grotzinger, 1996). Similarly, sequence bounding unconformities may be a consequence of sediment supply variations rather than erosion during subaerial exposure of marine strata (e.g. Schumm, 1993; Flemings and Grotzinger, 1996; Best and Ashworth, 1997; Martin, 2011). Moreover, Burgess and Prince (2015) suggested that the identical progradational to retrogradational shoreline trajectories can form at different phases of relative sea-level changes. Likewise, whilst aggradational stacking patterns are frequently interpreted as relative sea-level rise, it has been suggested that topset aggradation may occur either during relative sea-level

fall or stillstand (e.g. Burgess et al., 2006; Swenson and Muto, 2007; Prince and Burgess, 2013).

Though the interplay between sediment supply and accommodation space has been well understood, previous work usually supposed that stratal geometries are dominated solely by the creation of accommodation. In practice, it was often assumed that there is a constant sediment flux through time (e.g. Posamentier et al., 1988; Van Wagoner et al., 1990; Plint and Nummedal, 2000; Neal and Abreu, 2009) or there is an idealized cycle of eustatic sea-level oscillations (e.g. Helland-Hansen and Hampson, 2009). Such methods allow possible histories of relative or even eustatic sea-level for observed strata to be generated from simple, conceptual models of system tracts and depositional sequences (Burgess et al., 2006). However, these assumptions are no longer tenable since variations in sediment supply have proved to be complex (Frostick and Jones, 2002). The information extracted in this way has large uncertainties and can be misleading if adopted to predict stratigraphy at depth for less well-known areas with limited subsurface data. Due to the high demands for extracting robust signals of eustasy, for example for paleoclimate studies, there is a widespread interest on alternative sedimentation scenarios of the strata formation that does not depend on simplifying assumptions.

For more quantitative research, numerical forward models are frequently used to help determine stratal controls. A variety of software packages are available for this task, for example SEDSIM (Tetzlaff and Harbaugh, 1989), STRATA (Granjeon and Joseph, 1999), Dionisos (Granjeon and Joseph, 1999) and SEDTEC (Boylan et al., 2002).

Stratigraphic forward models allow simulation of various depositional settings (e.g. siliciclastic delta and carbonate platform). The forward modelling products are manifested as synthetic strata in 2-D or 3-D for a set of input parameters describing variations in stratal controls through time. Non-uniqueness in stratigraphic forward modelling has long been highlighted since Burton et al. (1987). In spite of this, forward models have the advantage in that it is capable of showing different mechanisms by which selected strata can be produced. Using a simple geometric model, Heller et al. (1993) suggested that discovery of multiple solutions of a forward model can allow universal properties of all solutions to be deduced. In other words, it is possible to encapsulate variations in stratal controls once all possible solutions are found.

However, calculation of multiple solutions for more sophisticated stratigraphic forward models has been elusive. Inverse stratigraphic modelling was often incorrectly treated as an optimization problem assuming a unique solution can be determined by searching for the best match to the observations. A number of optimization methods, such as the genetic algorithm (Bornholdt et al., 1999), model ranking approach (Wijns et al., 2004) and Bayesian statistics (Charvin et al., 2009b), were developed to meet the best-fit models. These techniques, however, are unable to approach the non-unique problems because even the best-fit models could be reproduced by more than one set of parameters. Other studies were in favor of particular solutions that are thought to represent the realities most closely in a geological sense (e.g. Cross and Lessenger, 1999; Burgess et al., 2006; Burgess and Steel, 2017). Whilst multiple scenarios of model generation were considered in these cases, such methods tended to presume

that the real solution can eventually be discovered. In brief, stratigraphic modelling research lacks a quantitative inversion scheme that is able to produce multiple interpretations of stratal controls and yet is simple enough to be widely applicable in sophisticated, process-based models.

2.2 Inverse Problems in Thermochronology

Subsurface temperature is a key control on reactions of organic matter buried underground. Precise reconstruction of the thermal history in sedimentary basins can offer critical implications for petroleum exploration in that it enables the timing and volume of hydrocarbon generation to be predicted (Waples, 1994). Thermal structure beneath a basin varies with the depth of burial, thermal conductivities of rock, surface temperature and heat flow (or heat flux density) into the basin from below (Welte et al., 2012; Allen and Allen, 2013). Thermal history reconstruction is hampered by non-uniqueness as there are too many free parameters to deduce. Though the challenge of non-uniqueness has been known since the early stage of quantitative basin modelling by McKenzie (1978), explorationists are usually delighted to have found even one scenario that is consistent with the thermal indicators. In reality, however, there are likely to be many, each of which has large uncertainties leading to substantial risk in exploration and development of fields.

A common way to tackle non-uniqueness is to reduce the number of unknowns using supplementary knowledge. For instance, the burial history of sedimentary basins can be reconstructed using a general subsidence model (e.g. McKenzie, 1978) or a

backstripping approach (e.g. Sclater and Christie, 1980). Lithologies of the subsurface can be estimated in the field (e.g. Beck et al., 1971; Conaway and Beck, 1977), in a laboratory (e.g. Sass et al., 1984) or through an empirical model (e.g. Vasseur et al., 1995). Temperature at the seafloor may be estimated from paleoclimate change. Moreover, heat flow in the near surface (≤ 5 km depth) can be effectively thought of as vertically constant, except for in geothermal areas or basin margins where vertical variations in heat flow may be more significant (Gallagher and Sambridge, 1992). Hence, inverse modelling of thermal history in 1-D (i.e. a borehole) is simply to deduce paleo-heat flow. However, such models are still heavily non-unique because more than one sequence of heat flow variations could account for the same results.

Non-uniqueness can exist in various types of thermal indicators. The one most commonly used in thermal history reconstruction is vitrinite reflectance, which is defined as the percentage of incident light reflected from the surface of vitrinite particles in sedimentary rock (Tissot and Welte, 1984). Others include apatite fission-track, fluid Inclusions, K-Ar dating estimates, biological markers and clay mineralogy (Tissot et al., 1987). However, not a single type of thermal indicators can adequately determine the complete thermal history. For example, the reflectance of vitrinite is largely determined by the highest temperature that a sample experienced during its thermal exposure (Price, 1983), whilst the fission-track length of an apatite results from the recent cooling stage rather than from the earlier periods (Gallagher, 1995). In practice, multi-source data were often combined to infer thermal histories (e.g. Bray et al., 1992; Zhao et al., 1996; George et al., 2001; Carrapa et al., 2009). Though these

methods can allow thermal conditions during particular periods in specific regions to be better constrained, they fail to address the fundamental challenge of non-uniqueness.

The key to thermal history modelling is to understand the dependence of thermal indicator reaction on both time and temperature. Quantitative forward models have been developed for various types of thermal indicators, such as vitrinite reflectance (e.g. Royden et al., 1980; Burnham and Sweeney, 1989; Sweeney and Burnham, 1990; Nielsen et al., 2017), apatite fission-track (e.g. Green et al., 1989; Crowley, 1993; Ketcham et al., 2000; Ketcham et al., 2007) and geochemical data (e.g. Mackenzie and McKenzie, 1983). The forward problem of predicting thermal indicators at present has been relatively well established. In contrast, inverse thermal history modelling receives ongoing concerns, most of which focus on the non-uniqueness. To prevent inessential complications in the interpretation, Gallagher and Sambridge (1992) suggested that the 'smoothest' solutions (e.g. a time-temperature with the least variations) should be used. However, such solutions are, by definition, untypical and may be misleading.

Despite this, an optimistic viewpoint was proposed by Shen et al. (1992) who argued that a representative solution can be determined if multiple solutions derived from a model are similar to each other. This provided a useful insight into the inverse problem although only a small number of solutions were examined. Similarly, it has been suggested that calculation of multiple solutions can enable the uncertainties in time and temperature to be quantified (e.g. Corrigan, 1991; Nielsen, 1996). However, the majority of thermochronological studies relied on stochastic algorithms (e.g.

Willett, 1997; Hopcroft et al., 2007; Gallagher, 2012) that likely escape from local minima. Inversion strategies built upon these algorithms hope to generate a wide range of solutions that are compatible with the observations. However, these studies typically ended up with what were thought to be the statistically 'best' solutions (e.g. solutions with the maximum likelihood or the highest possibility), rather than the entire range of solutions. For more reliable information of paleohistory and for more accurate assessment of petroleum perspective, extra work should be done to produce complete interpretations of thermal indicators, from which firm conclusions can be extrapolated.

2.3 An Inverse Problem in Geophysics

A seismically low-velocity layer (LVL) has been identified in the deep upper mantle, just above the mantle transition zone (MTZ), in numerous regions around the world with lateral thickness from 20 km to over a hundred kilometres (e.g. Revenaugh and Sipkin, 1994; Song et al., 2004; Courtier and Revenaugh, 2007; Jasbinsek and Dueker, 2007; Schaeffer and Bostock, 2010; Huckfeldt et al., 2013; Hier-Majumder and Tauzin, 2017). The seismic anomaly in this layer is characterized by sharp seismic velocity reductions (-5.3% to -1.0% for *P* wave and -7.0% to -3.0% for *S* wave) on its upper-boundary at approximately 350 km depth (Vinnik and Farra, 2007; Tauzin et al., 2010; Tauzin et al., 2013). As the velocity reductions and the associated impedance contrasts are unlikely produced solely by the thermal effects that usually give rise to

diffusive boundaries, the 350-km LVL has been suggested as a seismic signature of compositional heterogeneity.

More specifically, the seismic reductions are frequently ascribed to a small amount of volatile-induced melt triggered by subducting slabs (e.g. Revenaugh and Sipkin, 1994) or mantle plumes (e.g. Vinnik and Farra, 2007) in surrounding regions. Some others suspect that a partially molten LVL could exist throughout the 350 km depth due to the gradient in melt-bearing capacity across the transition zone (Bercovici and Karato, 2003; Leahy and Bercovici, 2007). However, the presence of the LVL does not show evident correlation with particular tectonic settings in a global scale (Tauzin et al., 2010). Interpretation of the LVL can benefit from quantifying the fraction of melt within the LVL. An accurate estimate of the melting extent in the LVL is also essential to advance understanding of the volatile-storage capacity of the layer, the sources and migration of volatiles and the nature of the MTZ that plays a crucial rule in the volatile cycle of the Earth.

Seismic velocities in the mantle are controlled by the interplay between thermal and compositional properties. Similar to other inverse problems, estimation of melting extent in the LVL suffers from non-uniqueness owing to the trade-off effect between the multiple factors. Whilst ideal seismic speeds at various depth of the mantle in the absence of melting are given by global predictive models, such as the Preliminary Reference Earth Model of Dziewonski and Anderson (1981), exact velocities can vary significantly in different regions. The petrologic model of Xu et al. (2008) indicates that a higher temperature typically leads to lower seismic velocities, whereas the influence

of bulk solid composition may differ at various depth in the mantle. Seismic velocity reductions in a melt-bearing aggregate depend upon the volume fraction, geometry and composition of the melt. In addition, these factors are strongly correlated with each other. The geometry of melt depends upon the dihedral angle at the grain-melt interface and the melt volume fraction (von Bargen and Waff, 1986; Takei, 1998, 2002). Whilst variations in melt composition leave a relatively insignificant impact on seismic velocities, it is known that the geometry of melt has notable dependence on the composition (Yoshino et al., 2005; Wimert and Hier-Majumder, 2012).

Previous studies have provided additional information regarding properties of the solid mantle and the melt. Numerical models indicated empirical calibration between thermal conditions in the LVL and the thickness of MTZ below (e.g. Courtier et al., 2007; Tauzin and Ricard, 2014). Experimental measurements suggested variations in dihedral angles for different types of melt, for example carbonated melt (e.g. Minarik and Watson, 1995) and hydrous basalt (e.g. Mei et al., 2002). Others proposed elastic properties of the melt, such as the bulk modulus, shear modulus and density for carbonated peridotite melt (e.g. Ghosh et al., 2007) and mid-ocean ridge basalt (e.g. Guillot and Sator, 2007). However, though the seismic and petrologic constraints provide a reasonable range for the unknown parameters, these are not known with much precision. As a consequence, there are still a large number of possible solutions within the range.

The key challenge in interpretation of the LVL is to simultaneously determine the multiple seismic controls. Having mantle temperature, bulk solid composition and

partial melting incorporated in a forward model enables seismic velocity reductions to be predicted (e.g. Hier-Majumder, 2017). Once the other parameters are specified with educated guesses, the corresponding melt volume fraction can be deduced by trying different values until the model fits the seismic observations. This method was used to estimate the melt volume fraction in the LVL beneath the South Pacific (Hier-Majumder and Courtier, 2011), the Hawaii Islands (Hier-Majumder et al., 2014), the Western US (Hier-Majumder and Tauzin, 2017) and Southeastern China (Ma et al., 2020). However, discoveries in these studies should be carefully examined since the melt volume fractions estimated are highly sensitive to the associated parameters and hence small errors in the assumptions can lead to large changes in the results (Hier-Majumder et al., 2014). An alternative estimation strategy that hopes to overcome these drawbacks should involve constructing a good-fit model, unravelling the competing effect of the multiple controls and encapsulating variations in the mantle properties.

3 Methodology: Determining Symmetries in Numerical Models

A quantitative inverse method, based upon forward modelling techniques and the principle of symmetry, is proposed for tackling non-unique inverse problems. The inversion procedure can begin with any arbitrary solution that produces the desired model. Correlations between multiple solutions can be linearized by considering small differences in the solutions. Using this insight, any solution can be directly modified into another solution that gives exactly the same model. The general procedure of the symmetry method can be described as follows:

(1) First, give a tiny increment into the parameters of a forward model, which gives rise to a residual in the model output.

(2) As the increment is small enough, the residual can be approximated as a linear function (e.g. using the 1st order Taylor's expansion).

(3) The linear approximation enables calculation of required changes in other parameters to compensate the residual.

(4) Having the required changes resolved from the linear function allows parameters to be properly modified and hence the original model restored.

(5) The modified parameter set gives a new solution to the same model. Now give another increment to the parameters and repeat the procedure.

Iterations of the procedure can produce a range of solutions in addition to the initial solution. A significant advantage of the proposed method is that the principle of

symmetry is entirely general. That is, the iterative inversion procedure can be adapted to any forward models, even if a model is non-linear. Applications of the symmetry-based method to a diverse range of geological inverse problems will be given in the following chapters.

Calculation applied in step (3) requires understanding of the compensation effect between multiple parameters of the model. This can be mathematically expressed as follows given a general function

$$z = F(x, y) \tag{3.1}$$

, where x and y are variables for the model, z is model output and F can by any non-linear function. Both x and y can vary through time, subject to the constraints imposed by $x = \varphi(t)$ and $y = \psi(t)$, where t is time. For instance, x can be sediment supply history and y can be the relative sea-level history, whereas z can be strata formation in response to tectono-sedimentary processes F in a depositional system. An alternative solution to the model can be found by a different set of variables $x' = \varphi'(t)$ and $y' = \psi'(t)$ that reproduce the same results, i.e. $F(x', y') = F(x, y)$. In the context of numerical modelling, x, y and z should be parameterized with discrete values. The time-dependent variables x and y may be represented by a pair of *M*-length vectors $\boldsymbol{x}$ and $\boldsymbol{y}$, where

$$\boldsymbol{x}^{\mathrm{T}} = (x_1, x_2, \dots, x_M) \tag{3.2}$$

and

$$\boldsymbol{y}^{\mathrm{T}} = (y_1, y_2, \dots, y_M) \tag{3.3}$$

Similarly, the modelling result z may be represented numerically by an *N*-length vector $\boldsymbol{z}$, where

$$\boldsymbol{z}^{\mathrm{T}} = (z_1, z_2, \dots, z_N) \tag{3.4}$$

Now the forward model can be rewritten in matrix notation

$$\boldsymbol{z} = F(\boldsymbol{x}, \boldsymbol{y}) \tag{3.5}$$

Having a small enough change ($\delta\boldsymbol{y}$) introduced into variable $\boldsymbol{y}$, a residual $\Delta\boldsymbol{z}$ is caused in the modelling result $\boldsymbol{z}$. To compensate the residual, a proper change $\delta\boldsymbol{x}$ is required in variable $\boldsymbol{x}$ to replicate the original result, i.e. $F(\boldsymbol{x} + \delta\boldsymbol{x}, \boldsymbol{y} + \delta\boldsymbol{y}) = F(\boldsymbol{x}, \boldsymbol{y})$. This can be represented in a linear form

$$\Delta\boldsymbol{z} = \mathrm{A}\delta\boldsymbol{x} \tag{3.6}$$

, where A is a *N* × *M* matrix of coefficients of which the elements are partial derivatives of F with respect to $\boldsymbol{x}$, i.e.

$$\mathrm{A}_{ij} = \frac{\partial F_i}{\partial x_j} \tag{3.7}$$

, where i = 1, 2, …, *N* and j = 1, 2, …, *M*. The matrix element values can be derived from the forward model using a finite difference approach. That is, first run the default model and then run the model again with a small increase given to input parameters. The partial derivatives are calculated as the difference between the two model runs divided by the increase in parameters. Properly solving $\delta\boldsymbol{x}$ from eq. 3.6 can allow a new solution to the model to found as $\boldsymbol{z} = F(\boldsymbol{x} + \delta\boldsymbol{x}, \boldsymbol{y} + \delta\boldsymbol{y})$. Solutions to eq. 3.6 depend upon the number of constraints and the number of unknowns:

(1) When *M* = *N*

The number of equations is the same as the number of unknowns in eq. 3.6 and the question is said to be equi-determined. Solution to eq. 3.6 can found by

$$\delta \boldsymbol{x} = \mathrm{A}^{-1}\Delta \boldsymbol{z} \tag{3.8}$$

, where A^{-1} is the inverse of matrix A. Note that the inverse of a matrix only exists if the matrix is square and it has a non-zero determinant. Clearly, matrix A is square when *M* = *N*. It is expected that the determinant of the matrix $\det(\mathrm{A}) \neq 0$. Otherwise the problem is actually under-determined (*M* > *N*), which will be discussed a little later in this chapter.

(2) When *M* < *N*

There are more equations than unknowns in eq. 3.6 and the problem is so called over-determined. In general, there is no solution to the problem as there are always misfits between the two sides of eq. 3.6. Hence, a term of errors $\boldsymbol{e}$ should be introduced into the equation, which gives

$$\Delta \boldsymbol{z} = \mathrm{A}\delta \boldsymbol{x} + \boldsymbol{e} \tag{3.9}$$

In this case, to solve eq. 3.6 is to find an optimal $\Delta \boldsymbol{z}$ by minimizing the sum of square errors. Writing eq. 3.9 in full gives

$$e_i = \Delta z_i - \sum_{j=1}^{M} \mathrm{A}_{ij}\delta x_j \tag{3.10}$$

, where i = 1, 2, …, *N*. As a consequence, the squared sum of errors is

$$E^2 = \sum_{i=1}^{N} {e_i}^2 = \sum_{i=1}^{N} \left(\Delta z_i - \sum_{j=1}^{M} \mathrm{A}_{ij} \delta x_j \right)^2 \tag{3.11}$$

E^2 can be minimized by setting $\partial E^2 / \partial \delta x_k = 0$ using unknowns $\{\delta x_k\}$ (k = 1, 2, …, *M*), leading to

$$2 \sum_{i=1}^{N} \left[\Delta z_i - \sum_{j=1}^{M} \mathrm{A}_{ij} \delta x_j \right] \mathrm{A}_{ik} = 0 \tag{3.12}$$

, which may be rearranged as

$$\sum_{j=1}^{M} \sum_{i=1}^{N} \mathrm{A}_{ik} \mathrm{A}_{ij} \delta x_j = \sum_{i=1}^{N} \mathrm{A}_{ik} \Delta z_i \tag{3.13}$$

Writing the above in matrix notation yields

$$\mathrm{A}^{\mathrm{T}} \mathrm{A} \delta \boldsymbol{x} = \mathrm{A}^{\mathrm{T}} \Delta \boldsymbol{z} \tag{3.14}$$

$\mathrm{A}^{\mathrm{T}}\mathrm{A}$ is invertible as it is square. Hence, the least square $\delta \boldsymbol{x}$ is given by

$$\delta \boldsymbol{x} = -(\mathrm{A}^{\mathrm{T}} \mathrm{A})^{-1} \mathrm{A}^{\mathrm{T}} \Delta \boldsymbol{z} \tag{3.15}$$

(3) When *M* > *N*

There are less equations than needed to solve the unknowns and thus the problem is under-determined. For any change in $\boldsymbol{y}$, there are more than one way to modify $\boldsymbol{x}$ in order to retain $\boldsymbol{z}$. A useful choice is to find the particular adjustment $\delta \boldsymbol{x}$ with the least length $|\delta \boldsymbol{x}|$ (i.e. the minimum-norm $\delta \boldsymbol{x}$). As such adjustment contains no unnecessary information, it is the smallest possible $\delta \boldsymbol{x}$ to compensate the residual $\Delta \boldsymbol{z}$. The smallest $|\delta \boldsymbol{x}|$ can be found by minimizing the length squared $\delta \boldsymbol{x}^{\mathrm{T}} \delta \boldsymbol{x}$ subject

to $\Delta \boldsymbol{z} = \mathrm{A}\delta \boldsymbol{x}$ using the method of Lagrange multipliers. First, the Lagrange multipliers are assembled into an *N*-length vector $\boldsymbol{\lambda}$. A Lagrange function $\boldsymbol{\mathcal{L}}$ is then formulated as

$$\boldsymbol{\mathcal{L}} = \delta \boldsymbol{x}^{\mathrm{T}} \delta \boldsymbol{x} + \boldsymbol{\lambda}^{\mathrm{T}} (\mathrm{A}\delta \boldsymbol{x} - \Delta \boldsymbol{z}) \tag{3.16}$$

Differentiating $\boldsymbol{\mathcal{L}}$ with respect to $\delta \boldsymbol{x}$ then gives

$$\frac{\partial \boldsymbol{\mathcal{L}}}{\partial \delta x_j} = 2\delta x_j + \sum_{i=1}^{N} \lambda_i \mathrm{A}_{ij} = 0 \tag{3.17}$$

, which may be rearranged as

$$\delta \boldsymbol{x} = -\frac{1}{2} \mathrm{A}^{\mathrm{T}} \boldsymbol{\lambda} \tag{3.18}$$

, subject to $\Delta \boldsymbol{z} = \mathrm{A}\delta \boldsymbol{x}$, such that

$$\Delta \boldsymbol{z} = -\frac{1}{2} \mathrm{A}\mathrm{A}^{\mathrm{T}} \boldsymbol{\lambda} \tag{3.19}$$

Matrix $\mathrm{A}\mathrm{A}^{\mathrm{T}}$ is square and hence its inverse exists. The Lagrange multipliers $\boldsymbol{\lambda}$ can be resolved as

$$\boldsymbol{\lambda} = -2(\mathrm{A}\mathrm{A}^{\mathrm{T}})^{-1} \Delta \boldsymbol{z} \tag{3.20}$$

Substituting from eq. 3.18 gives the minimum-norm solution of $\delta \boldsymbol{x}$

$$\delta \boldsymbol{x} = \mathrm{A}^{\mathrm{T}} (\mathrm{A}\mathrm{A}^{\mathrm{T}})^{-1} \Delta \boldsymbol{z} \tag{3.21}$$

An alternative way to solve eq. 3.6, when *M* > *N*, is to find the scenario that leads to the smoothest new solution $\boldsymbol{x} + \delta \boldsymbol{x}$, i.e. to seek an adjustment $\delta \boldsymbol{x}$ to minimize the roughness of vector $\boldsymbol{x} + \delta \boldsymbol{x}$, where $\delta \boldsymbol{x}$ subject to the constraint imposed by eq. 3.6. Calculation of the smoothest $\boldsymbol{x} + \delta \boldsymbol{x}$ has the advantage that it prevents unjustified

fluctuations from the new solution. The roughness of vector $\boldsymbol{x}$ is given by the finite difference of the first (R_1) and second (R_2) derivatives, in a similar way to the approach of Constable et al. (1987)

$$R_1 = \sum_{j=2}^{M} \left(\frac{x_j - x_{j-1}}{t_j - t_{j-1}} \right)^2 \tag{3.22}$$

and

$$R_2 = \sum_{j=2}^{M-1} \left(\frac{x_{j+1} - x_j}{t_{j+1} - t_j} - \frac{x_j - x_{j-1}}{t_j - t_{j-1}} \right)^2 \tag{3.23}$$

, where t_j is the time corresponding to x_j. In matrix notation, both R_1 and R_2 can be written as $\boldsymbol{x}^{\mathrm{T}}\mathrm{D}^{\mathrm{T}}\mathrm{D}\boldsymbol{x}$, where D is an $M \times M$ matrix of coefficients given by eq. 3.22 (for R_1) and eq. 3.23 (for R_2). As a consequence, the smoothest $\boldsymbol{x} + \delta\boldsymbol{x}$ can be found by minimizing its roughness where $\mathrm{A}\delta\boldsymbol{x} = \Delta\boldsymbol{z}$. Summing up the solution roughness and model misfit gives a trade-off function

$$T(\theta) = (\boldsymbol{x} + \delta\boldsymbol{x})^{\mathrm{T}}\mathrm{D}^{\mathrm{T}}\mathrm{D}(\boldsymbol{x} + \delta\boldsymbol{x}) + \theta(\Delta\boldsymbol{z} - \mathrm{A}\delta\boldsymbol{x})^{\mathrm{T}}(\Delta\boldsymbol{z} - \mathrm{A}\delta\boldsymbol{x}) \tag{3.24}$$

, where θ is an unknown scalar (also known as a penalty parameter) to replace the multiplier in eq. 3.20. Note that it is practically impossible to solve for θ because this ends up with inverting the singular matrix $\mathrm{D}^{\mathrm{T}}\mathrm{D}$ of which the determinant is zero (this happens because all elements in the first row of matrix D are zero). Instead, a large value (e.g. 10^3 - 10^6) is chosen for θ and hence to minimise T is to ensure the model misfit dominated by θ is small enough with the remaining degrees of freedom to reduce the solution roughness. Setting $\partial T / \partial \delta\boldsymbol{x} = 0$ gives

$$\mathrm{D}^{\mathrm{T}}\mathrm{D}(\boldsymbol{x}+\delta\boldsymbol{x})-\theta(\mathrm{A}^{\mathrm{T}}\Delta\boldsymbol{z}-\mathrm{A}^{\mathrm{T}}\mathrm{A}\delta\boldsymbol{x})=0 \tag{3.25}$$

The required $\delta\boldsymbol{x}$ is therefore found by

$$\delta\boldsymbol{x}=(\theta\mathrm{A}^{\mathrm{T}}\mathrm{A}+\mathrm{D}^{\mathrm{T}}\mathrm{D})^{-1}(\theta\mathrm{A}^{\mathrm{T}}\Delta\boldsymbol{z}-\mathrm{D}^{\mathrm{T}}\mathrm{D}\boldsymbol{x}) \tag{3.26}$$

All the treatments presented above are used to resolve vector $\delta\boldsymbol{x}$ from eq. 3.6, depending on the numbers of unknowns and constraints provided. The $\delta\boldsymbol{x}$ resolved indicates adjustment needed by vector $\boldsymbol{x}$ to compensate the residual $\Delta\boldsymbol{z}$ caused by changes $\delta\boldsymbol{y}$ in vector $\boldsymbol{y}$. As a consequence, an alternative solution to model $\boldsymbol{z}$ can be determined as $\boldsymbol{z}=F(\boldsymbol{x}+\delta\boldsymbol{x},\boldsymbol{y}+\delta\boldsymbol{y})$. Readers are referred to Appendix 1 for pseudocode scripts written in Python style demonstrating implementation of the numerical algorithm on computers.

4 Non-uniqueness and Symmetry in Stratigraphic Interpretations: A Quantitative Approach for Determining Stratal Controls

Jie Xiao[a, b, c] and Dave Waltham[a]

(a) Department of Earth Sciences, Royal Holloway University of London, Egham, Surrey TW20 0EX, UK (E-mail: Jie.Xiao.2016@live.rhul.ac.uk)

(b) State Key Laboratory of Organic Geochemistry, Guangzhou Institute of Geochemistry, Chinese Academy of Sciences, Guangzhou 510640, China

(c) University of Chinese Academy of Sciences, Beijing 100049, China

Author statement

This chapter is a reprint of the article as appears in: Xiao, J., and Waltham, D., 2019, Non-uniqueness and symmetry in stratigraphic interpretations: A quantitative approach for determining stratal controls, *Sedimentology*, v. 66, no. 5, p. 1700-1715. The thesis author was the primary investigator and lead author of this published work. His contributions to this work are summarized as follows:

(1) Methodology: development of the numerical approaches;

(2) Software: development of the computer programs;

(3) Investigation: analysis of subsurface data from Baltimore Canyon; application of the invented techniques to interpreting Baltimore Canyon stratigraphy;

(4) Writing: creation of a complete first draft.

4.1 Abstract

Different combinations of stratal controls could produce identical sequence architectures. Consequently, interpretations of the stratigraphic record, for example to infer palaeo-climate and eustatic sea-level history, suffer from non-uniqueness. However, variations in the multiple controls can be encapsulated through discovery of all possible solutions to an interpretation. As this paper demonstrates, a single solution can be directly transformed into an alternative solution that leaves the expected geological outcomes unaltered, which can be regarded as the existence of symmetry in the interpretation. Repetitive application of the symmetry method can therefore allow additional solutions to be rapidly derived given an existing solution. The proposed method has been adapted to a stratigraphic forward model for interpreting the Baltimore Canyon Trough (USA) stratigraphy. Modelling results have indicated the ranges of changes in relative sea-level, sediment supply and subaerial erosion from Oligocene to Mid-Miocene. Using these limits, it is possible to determine what appears to be true in the palaeo-history, even when a solution is not unique.

Keywords: Non-uniqueness, symmetry, sequence stratigraphy, stratal geometries, palaeo-climate

4.2 Introduction

It has long been understood that siliciclastic depositional systems are controlled on a large scale by subsidence, eustasy and sedimentation (Barrell, 1917; Sloss, 1962). With the increased use of seismic data to image basin margins, these concepts were

repackaged as sequence stratigraphy (Vail, 1977; Posamentier et al., 1988) which is an example of inverse observational methods; stratigraphic architectures are observed and stratal controls such as relative sea-level history deduced. However, such an inverse method usually yields non-unique solutions because more than one set of parameters could produce identical observations. The non-uniqueness in the inverse problems can be demonstrated through a metaphor of simple mathematic functions such as $\boldsymbol{x} + \boldsymbol{y} = \boldsymbol{z}$, from which one can never resolve $\boldsymbol{x}$ and $\boldsymbol{y}$ uniquely given only the value of $\boldsymbol{z}$. In the context of sedimentology, assuming $\boldsymbol{x}$ and $\boldsymbol{y}$ are sea-level and sediment supply, respectively, while $\boldsymbol{z}$ is the resulting stratal geometry, it could be hard, if possible, to distinguish the individual influences of the multiple controls.

What makes stratigraphic inverse problems even more challenging is that tectonic and sedimentary processes cannot be simplified as linear functions, and the stratal controls are likely to be strongly correlated rather than independent. Analogue and numerical experiments have shown numerous examples of non-unique stratal geometries. These include transgressive surfaces (e.g. Schlager, 1993; Flemings and Grotzinger, 1996), shoreline trajectories (e.g. Burgess and Prince, 2015), sequence bounding unconformities (e.g. Flemings and Grotzinger, 1996) and aggradational topsets (e.g. Burgess and Allen, 1996; Swenson and Muto, 2007; Prince and Burgess, 2013). Many of these examples were displayed by two-dimensional (2D, i.e. in cross-section) models; however, as strata grow in three-dimensions (3D), the third dimension also needs to be considered on some occasions. Simulating 3D processes can introduce significant extra complications (for example, lobe-switching that leads to

asymmetrical delta progradation) and significant additional ways in which the results can be non-unique.

To address the non-uniqueness, sequence stratigraphic studies typically assume accommodation space as the dominant control on any given sedimentary system; moreover, tectonic influences are simplified as monotonic steady subsidence, and sediment supply are considered as a simple function of time (e.g. Posamentier et al., 1988; Van Wagoner et al., 1990; Plint and Nummedal, 2000; Neal and Abreu, 2009). These simplifying assumptions have allowed application of simple models of systems tracts and sequences to reconstruct a relative and perhaps even eustatic sea-level history from selected strata that is then used as a predictive model for stratal patterns in other less well-known areas (Burgess et al., 2006). Numerous problems with this approach have been highlighted (e.g. Heller et al., 1993; Miall, 1997), and the significance of other controls has been recognized. Despite its obvious limitations, this method is still widely applied, either because of its assumed global predictive power or because few practical alternative approaches exist.

However, as evidence for complex tectonic and sediment supply variations mounts (Frostick and Jones, 2002), and as the need increases for robust stratigraphic evidence for palaeo-climate change, a new method is required for determining the multiple controls on stratal patterns that does not depend on simplifying assumptions. Using the principles of symmetry to generate multiple solutions could meet this requirement. This paper shows how the symmetry concept can be adapted to a stratigraphic forward model to produce many possible solutions accounting for the observed sequence architecture. Thus, the use of symmetry methods can provide a

more rigorous approach for identifying multiple controls on stratal geometries. To demonstrate the methodology, this paper initially examines 2D models. As a real-case study, the proposed method is applied to interpret the sequence architecture of Oligocene to Mid-Miocene stratigraphy from the Baltimore Canyon trough, New Jersey, USA.

4.3 Methodology

4.3.1 Forward model

In order to demonstrate and investigate the concept of non-uniqueness in sequence stratigraphy, a computer program, modified from SedTec 2000 (Boylan et al., 2002), has been used to simulate 2Dstratal architectures in response to tectonic and sedimentary effects. Compared with SedTec, an important modification in the new program is that it operates in increments of sediment supply instead of the more conventional approach of stepping forward in constant intervals of time. A source of sediment is assumed to be fixed on the left-hand side of the model. Sediments supplied to the depositional system are classified into coarse-grained and fine-grained. Proportions of the coarse and fine sediment fractions within the initial supply are specified as coarse to fine ratio through time. The abilities of coarse and fine grains to transport are characterized by a variable known as 'transport distance'. Fine grains have a large value of transport distance and travel a long way from the point of supply, whilst coarse grains have a small value of transport distance and settle rapidly. In the forward model, strata either fill up to the sea-surface when there is sufficient sediment to completely fill available accommodation, creating a delta topset, or repose to form

a delta foreset. Tectonic rotation effects are also included, of which the hinge point is fixed at the left-edge of the model. The erosion effect in the model is simplified as a subaerial erosion rate, i.e. erosion occurs only above the sea-surface. For more details of the algorithm and its numerical solutions, see Hardy and Waltham (1992), Hardy et al. (1994) and Waltham and Hardy (1995). It is worth noting that forward models applied in this work can be considered as general rather than specific and the methodology presented later for handling non-uniqueness can apply in any type of stratigraphic forward models.

4.3.2 Sea-level vs sediment supply

Figure 4.1 shows an example of strata generated when both sea-level and sediment supply vary through time in a simulated deltaic setting. The identical section can be equally produced by either of the two different solutions (i.e. fig. 4.1A and B). Erosion has not been included in this initial, simple case (but will be introduced later). Input sediment was set to be homogeneous in grain-size. Note that sediment supply is cumulative, and thus rate of supply is given by the gradient of the sediment supply curve. This gradient must be non-negative at all times. The remaining part of fig. 4.1 shows a 'sea-level versus sediment supply' cross-plot (an SS–SL curve). This can be generated simply by pairing corresponding sea-level and sediment supply values at each point in time. Note that this curve could alternatively be generated directly from observed strata because sea-level through time is indicated by the maximum height at which deposition is occurring whilst cumulative sediment supply is given by the cross-sectional area beneath the corresponding sea floor surface. Crucially, it is also possible

to do the reverse and generate the synthetic strata directly from the sea-level and sediment supply pairs. Thus, the cross-section and the SS–SL curves are interchangeable; they are simply two different ways of displaying the same information.

Fundamental to the issue of non-uniqueness is the observation that identical SS–SL curves and therefore, by the argument of interchangeability above, identical stratal architectures, can be generated from different combinations of sediment supply and sea-level curves. This point is illustrated by fig. 4.2 which shows how to derive a sea-level curve from an observed architecture given an arbitrary sediment supply. The arbitrary sediment supply curve was constrained only by the need to start at zero, finish at the same final sediment supply as before and to have a non-negative gradient at all times. Once an appropriate sediment supply curve is defined, the corresponding sea-level curve is found by noting that, by definition, the sediment supply curve defines a sediment supply to time conversion. Given this the known SS–SL curve from fig. 4.1 can be converted into the required sea-level curve simply by determining which value of sea-level corresponds to the values of sediment supply on the sediment supply curve. Note that there are an infinite number of sediment supply curves that satisfy the start, finish and gradient constraints described above and so there are an infinite number of sediment supply and sea-level combinations corresponding to any given SS–SL curve.

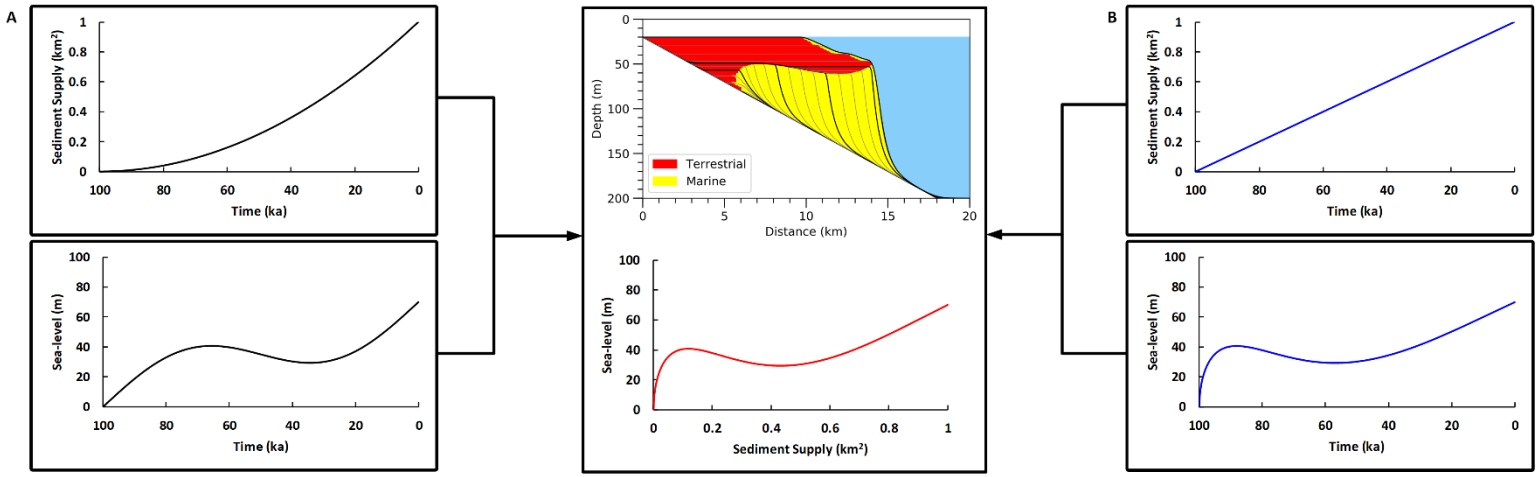

Figure 4.1 Two sets of sediment supply and sea-level curves (A) and (B) are plotted with the resulting strata geometry from a simple 2D forward model of delta formation, and a cross-plot of sediment supply versus sea-level (SS–SL curve). Note that ka = thousands of years ago (an age). Different histories of sea-level and sediment supply can generate exactly the same stratal geometry, demonstrating non-uniqueness.

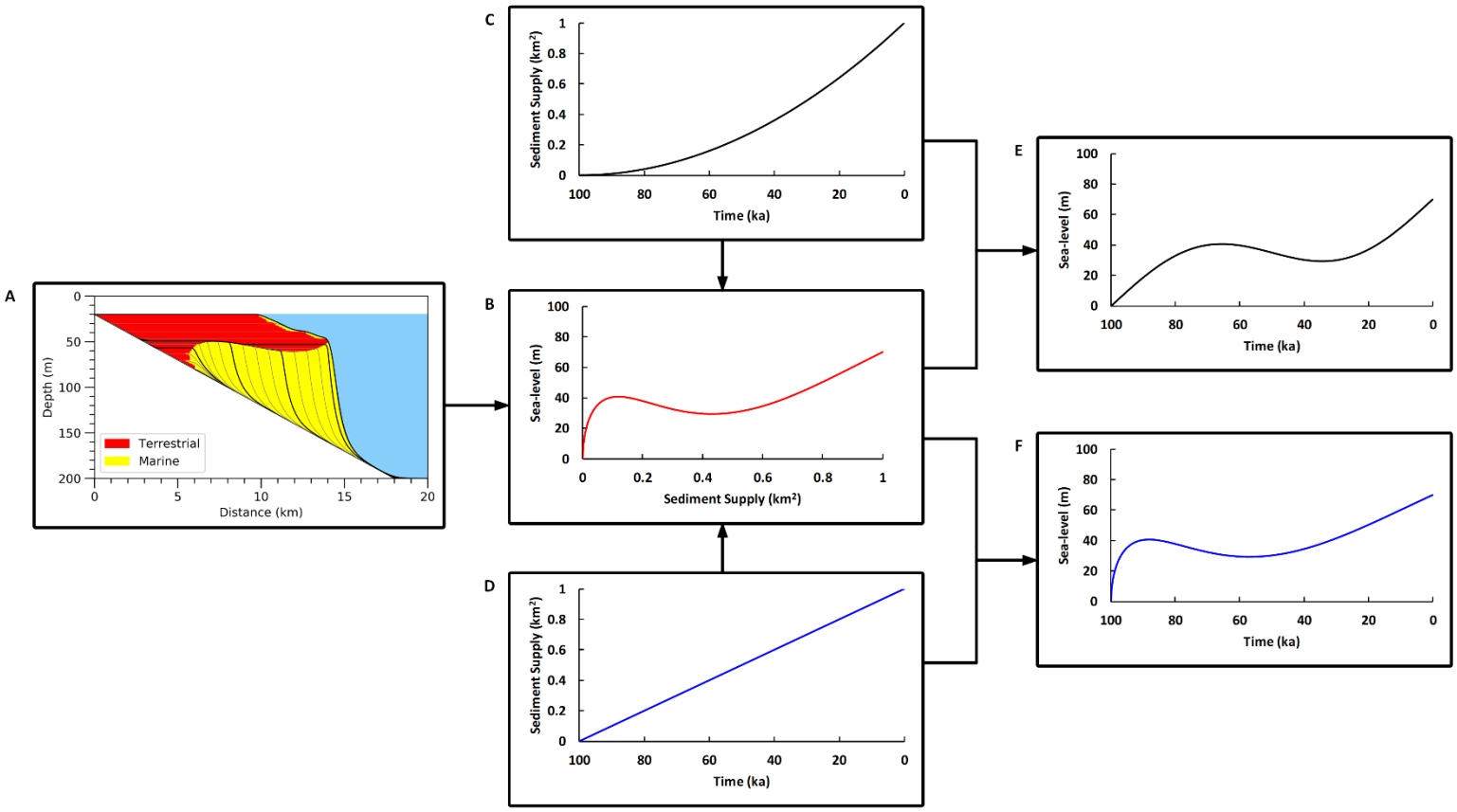

Figure 4.2 Principles of symmetry can be used to derive multiple interchangeable sediment supply and sea-level curves from a stratal geometry. Observation on stratal geometry (A) is used to derive a SS–SL curve (B). Two sediment supply curves (C) and (D) are derived from the observed geometry constrained by required sediment supply magnitude and by conservation of mass, and the symmetry encoded in the SS–SL curve is used to derive a sea-level curve for each of these sediment supply curves (E) and (F). The resulting pair of sediment supply curve and sea-level curve can generate identical stratal geometry as seen in (A).

4.3.3 Non-uniqueness and symmetry

The approach used above to generate multiple solutions to the delta-inversion problem can be thought of as exploiting a symmetry in the forward model since it illustrates how different combinations of sea-level and sediment supply can be directly derived whilst the stratal geometry is unaltered. This is similar to rotating a square through 90° and leaving it unchanged. The close relationship between non-uniqueness and a generalized concept of symmetry is widely understood in physics (e.g. Elliott and Dawber, 1979) but is not frequently used in geology. However, a similar analysis has previously been undertaken for a geochemical problem (Waltham and Gröcke, 2006) where it was shown that, although the problem of determining the cause of observed seawater Sr-isotope fluctuations through time has an infinite number of solutions, these are closely related to one another because there is an underlying symmetry.

Symmetry relationships can be used to transform any single solution, once known, into other solutions and therefore gives a practical method for finding large numbers of related solutions. More importantly, the symmetries encapsulate properties of all possible solutions. For example, in the delta-inversion problem discussed above, the symmetry (all solutions have the same SS–SL curve and a monotonic sediment supply curve) implies that all compatible sea-level curves have the same sequence of sea-level highstands and lowstands and only differ in the time-durations between these, i.e. all possible sea-level curves are just horizontally deformed versions of one another, as can be verified by close examination of fig. 4.1. Thus, the problem of estimating sea-level history from stratal architecture in the absence of dating information is under-

constrained rather than unconstrained, i.e. not all sea-level curves are compatible with the observations even though no single sea-level history can be extracted.

4.3.4 Multiple grain-sizes

Application of the symmetry method becomes more difficult if additional controlling factors are included in the model for delta formation. For example, if the factor of multiple grain-sizes is included then the resulting stratal architecture varies according to the relative supplies of each grain size. A coarse-grained delta may have a steeper foreslope than a fine-grained delta and, for a mixed supply, slope may vary with distance. Under these circumstances, the SS–SL curve does not contain sufficient information to allow a complete reconstruction of the architecture. However, the interchangeability argument of the forward model can be extended to include this complication. This can be done by introducing a coarse/fine ratio versus sediment supply cross-plot (SS–CF curve) into the method. Figure 4.3 shows that identical stratal architectures can be produced by different solutions of sea-level, sediment supply and coarse/fine ratio histories. Both solutions can produce the same SS–SL and SS–CF curves. Similar to the generation of the SS–SL curve, the SS–CF could also be retrieved directly from an observed architecture through careful examination. Thus, the combination of SS–SL and SS–CF curves is interchangeable with the architecture. The combination can then serve as a proxy from which infinite numbers of solutions of sea-level, sediment supply and coarse/fine ratio variations can be derived.

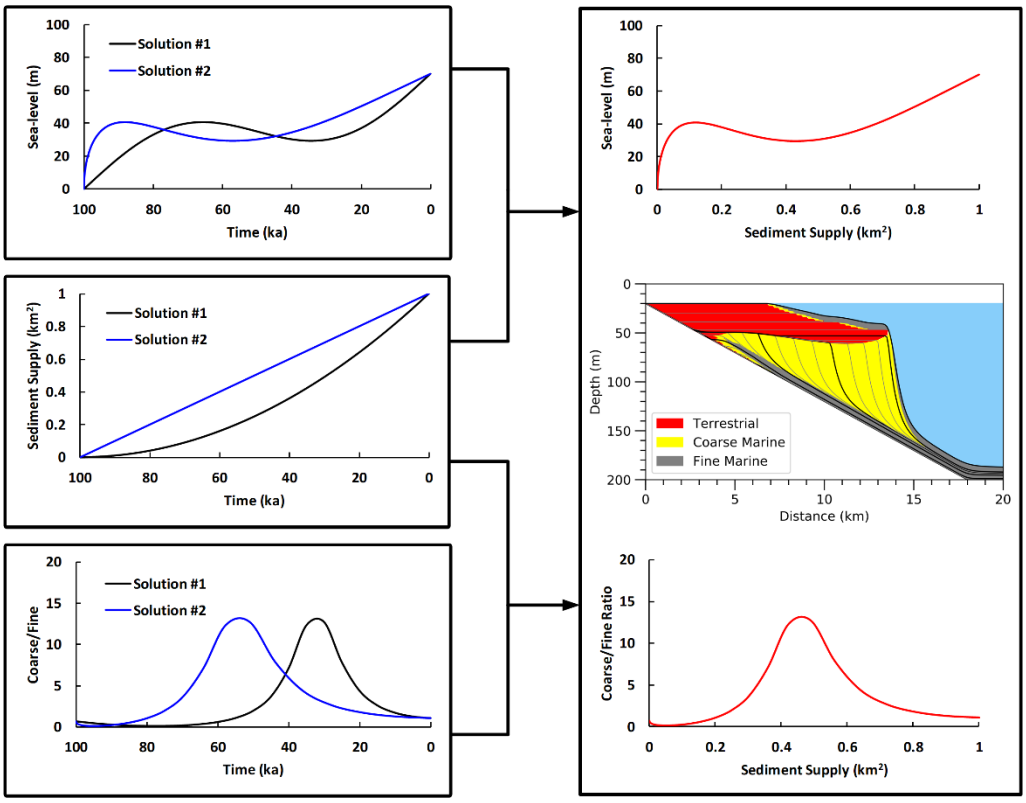

Figure 4.3 Non-uniqueness and symmetry in a more sophisticated model including multiple grain-sizes. The two solutions of relative sea-level curve, sediment supply curves and coarse/fine ratio curves can produce identical stratal geometry, SS–SL curve and cross-plot of sediment supply versus coarse/fine ratio (SS–CF curve). All additional solutions can be generated using the combination of SS–SL and SS–CF curves.

4.3.5 Subaerial erosion

All of the preceding examples are based on special cases of models in which the strata growth is controlled by variations in accommodation availability but not by the magnitude of sediment supply. A more difficult problem occurs if subaerial erosion is included since, during periods of sea-level fall, material on the delta top may be eroded and subsequently resettled on the delta foreset. As a consequence, maximum heights of sea-level rise are underestimated and much of the sediment reaches its final

resting-place with a significant time-delay compared to the time at which it was supplied. Thus, the apparent SS–SL and SS–CF curves produced from examining the architecture no longer agree with the true curves and thus the interchangeability argument breaks down.

However, given an erosive stratigraphic model where the interchangeability does not exist, symmetry of the model can still be exploited using linearization techniques and thus the general principles proposed here remain valid. The procedure can start with a simple solution that assumes no erosion (i.e. erosion rate = 0). A perturbation (i.e. a tiny increment) is then made to the erosion rate, which subsequently causes a residual in the model. The residual caused by the incremental change in erosion rate, however, may be compensated by adjustments in other controls. Successful calculation of the required changes in other parameters can allow the original solution to be modified appropriately and hence the model can be restored. Meanwhile, the original solution is transformed into an alternative solution whilst the model remains unchanged. The new solution can then be used as a basis of the next round of transformation. Repetitive application of the method can allow the original solution to be altered into an infinite number of additional solutions, each of which is associated with a different erosion rate. The workflow of the method is summarized in fig. 4.4. The algorithm of the method is given in Appendix 2, based on a model controlled by sea-level, sediment supply and subaerial erosion. However, the transformation process is completely general and can be extended to include additional factors (for example, multiple grain-sizes and a more realistic erosion effect as a function of water depth).

Note that the transformation method presented here also applies in the simplest deltaic model which involves only sea-level and sediment supply but not erosion. In fact, the non-uniqueness in the simplest model can be demonstrated either by the implicit interchangeability of SS–SL curve and the modelled section or by the transformation process.

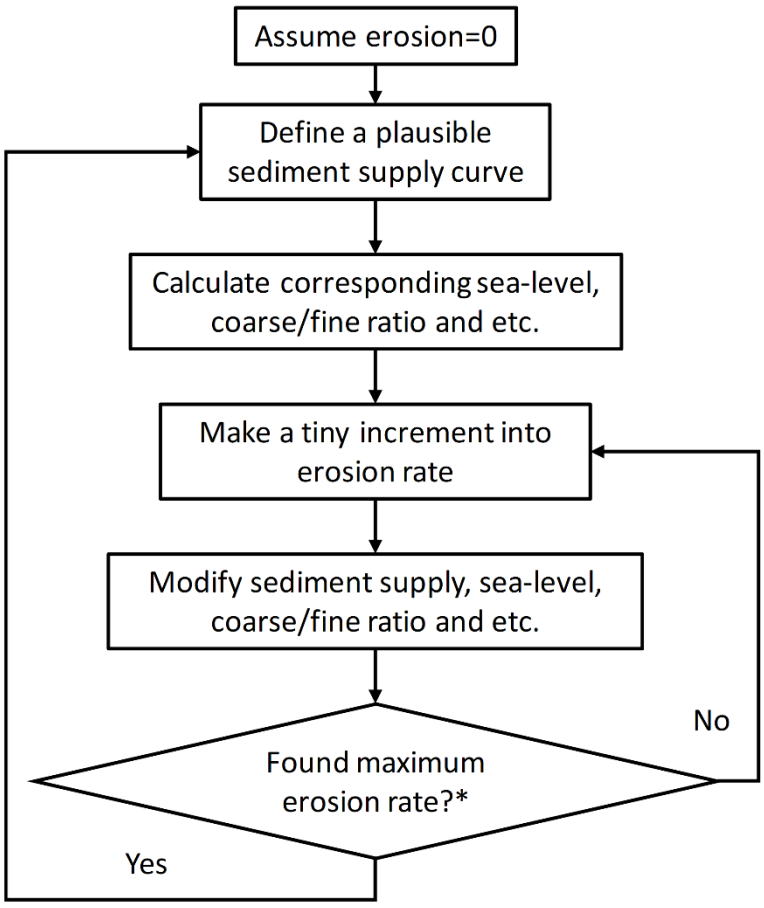

Figure 4.4 Generation of all possible solutions for a non-unique stratigraphic inverse problem. *The maximum erosion rate is defined by the assumed erosion rate in the solution where the gradient of cumulative sediment supply curve is 0 at a time. As the sediment supply rate must always be non-negative, no further increment could be made to the assumed erosion rate. Hence, the erosion rate in this solution is the highest possible subaerial erosion rate.

4.3.6 Encapsulating variations in the controls

An example shown in fig. 4.5 demonstrates how a starting solution that assumes no erosion can be transformed into a more realistic solution that assumes a plausible erosion rate. To compensate the erosion effect during subaerial exposure, higher sea-level and additional sediment were required before sea-level fall in order to produce a taller delta profile than the final observation. The additional sediment was then eroded when sea-level dropped below the delta top. Since the delta topset was mainly formed by coarse sediment, the majority of the additional supplies were coarse grains rather than fine grains. When the sediment was eroded from the delta top, it was then reworked and charged into the latter supply, which led to an overestimation of the latter coarse fraction. Consequently, modification is also needed in the coarse/fine ratio curve to leave the architecture unaltered. The three modified curves and the plausible erosion rate hence generate a new solution to the inverse problem. In addition, there could be an infinite number of sediment supply curves, as for the non-erosive case, and each of these give an infinite number of sea-level curves and coarse fraction curves which differ in their history of subaerial exposure episodes.

However, whilst there could be an infinite number of possible solutions to the problem, the problem is not completely unconstrained. As discussed earlier, the gradient of sediment supply curve must be non-negative. When a plausible erosion rate is introduced, increments are required in sediment supply rate during periods of sea-level rise to provide additional sediment. Because the final amount of cumulative sediment supply must remain unchanged, the sediment supply rate during sea-level

fall must decrease accordingly. The highest possible erosion rate during delta formation can be found in the solution where the gradient of sediment supply curve is zero at a point of time. Any solution that assumes a higher erosion rate than this value is geologically unfeasible. For the same reason, the sea-level curve in the solution indicates the maximum sea-level heights through time. As a result, upper-bounds can be placed upon the sea-level heights above the erosional surfaces and the associated subaerial erosion rate. Figure 4.6 shows an instance of how values of upper-bounds and the corresponding solutions are found. It should be noted that these values may vary when alternative (zero-erosion) starting solutions are applied, an example of which is given in fig. 4.7.

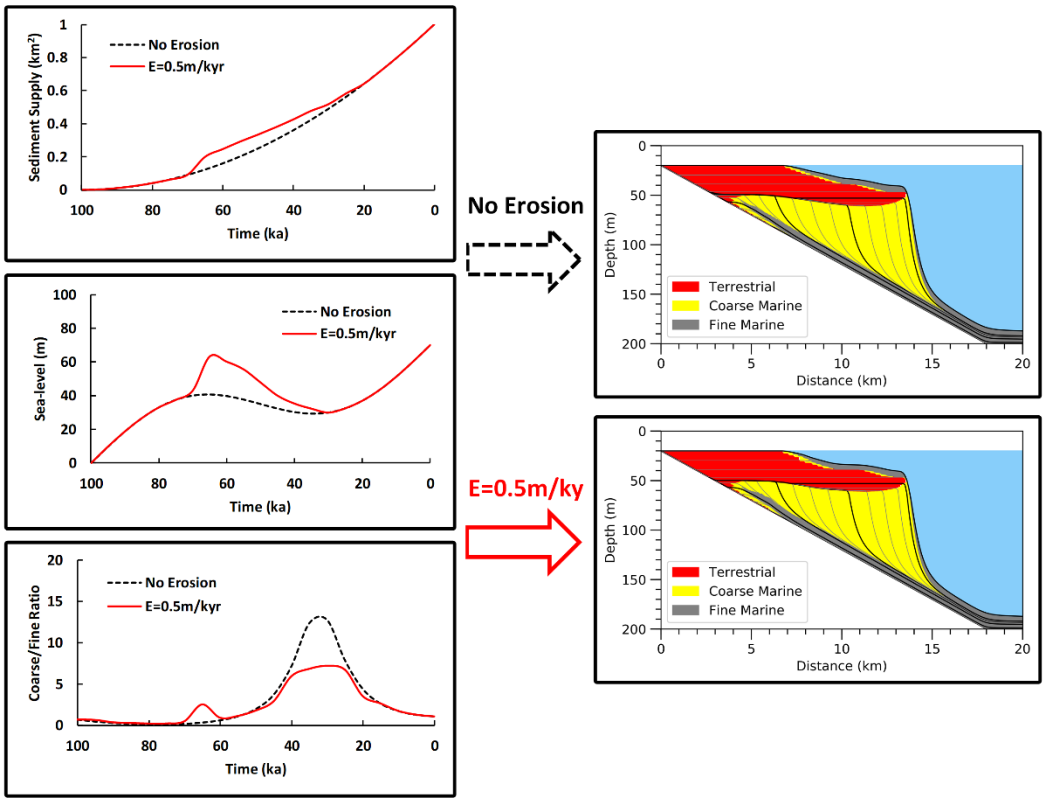

Figure 4.5 Using the symmetry method, a starting solution that assumes no erosion (black dotted curves) can be modified into an alternative solution with a plausible erosion rate (red solid curves). Note that kyr = thousands of years (a duration). Stratal geometries produced by the two solutions are identical.

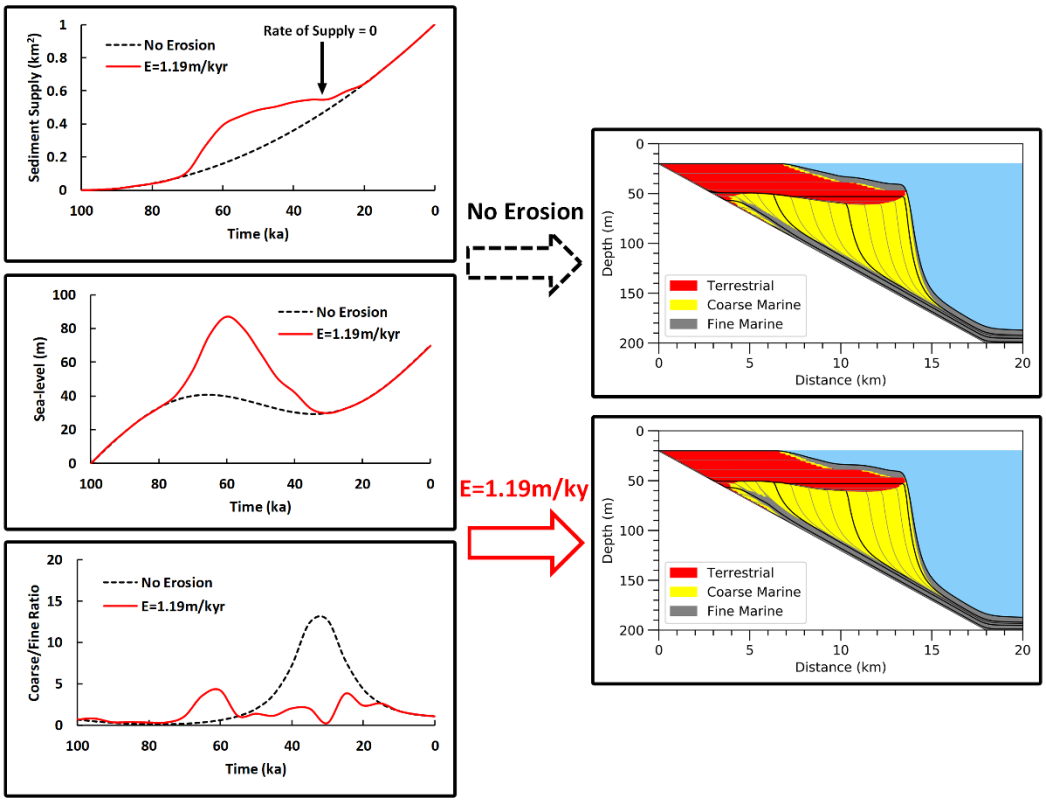

Figure 4.6 Another alternative solution (red solid curves) modified from the starting solution (black dotted curves). The gradient of the sediment supply curve in *ca* 35 ka of modelled period is shown to be 0, which suggests a sediment supply rate of 0 at this point of time. The erosion rate presented here is the highest possible erosion rate whilst the corresponding sea-level curve indicates the highest possible sea-level amplitude through time.

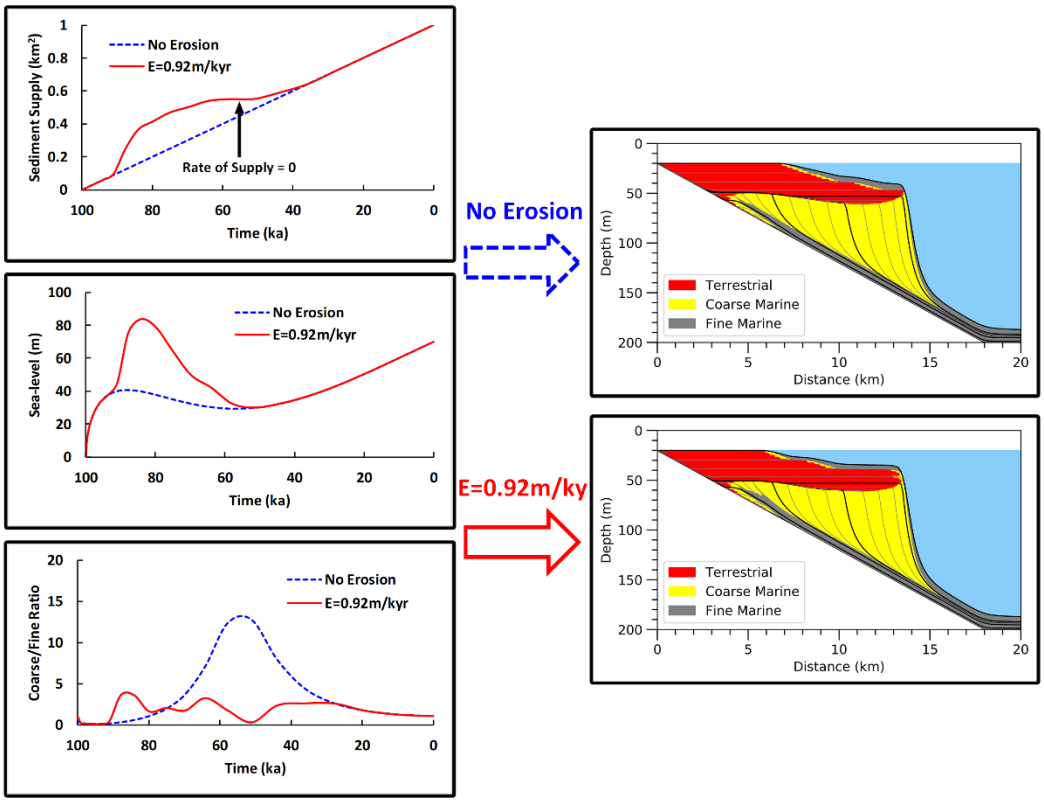

Figure 4.7 Using different starting solution can result in different sets of additional solutions. Note that upper-bounds upon sea-level height and upon associated erosion rate in each of the solution sets may also vary.

4.3.7 Using symmetry for determining multiple controls

The above theoretical treatment, based on a simple numerical forward model of deltaic sequence architecture, demonstrates the application of symmetry concept. It is also possible to determine relative sea-level heights, sediment supply and grain-size fractions from an observed sequence architecture. This would be done in a similar way to the back-stripping approach of Steckler et al. (1993):

i. Divide the architecture into a number of depositional packages, for example based upon well-defined stratal surfaces.

ii. Successfully strip off each layer by removing any effects due to compaction, rotation, faulting or folding.

iii. As each layer had been successively removed, the apparent (i.e. assuming zero erosion) sediment supply associated with the top depositional package can be estimated by measuring its area (2D) or volume (3D).

iv. The relative sea-level and sediment coarse/fine ratio associated with each package can also be estimated from analysis of stratal terminations like onlap and toplap, as well as from a shoreline trajectory analysis (Helland-Hansen and Hampson, 2009).

v. The successive sediment supply (from iii) and sea-level (from iv) pairs can be applied to produce an apparent SS–SL curve. Similarly, an SS–CF curve can also be generated using the sediment supply and coarse/fine ratio (from iv) pairs.

vi. The SS–SL and SS–CF curves can then be combined with an arbitrarily chosen sediment supply curve to give the corresponding sea-level curve and coarse/fine ratio curve. This step can be repeated for any number of appropriate sediment supply guesses.

vii. The initial (i.e. zero-erosion) models are then modified for finite erosion using the approach shown in fig. 4.4.

A diagram illustrating the back-stripping procedure [i.e. steps (i) to (iv) in the approach] can be found in (Steckler et al., 1993). A significant advantage of this method is that it allows generation of relative sea-level, sediment supply and

coarse/fine ratio values that can account for the observed strata. If dating estimates are available for the depositional packages, then it becomes possible to constrain the sediment supply curve used in step (vi). Consequently, the relative sea-level and coarse/fine ratio curves also become constrained. Note that the resulting histories are not based upon an unrealistic assumption of constant sediment supply.

Some of these steps in defining values of relative sea-level, sediment supply and coarse/fine ratio may not be straightforward. First, measurement of sediment amount in each stratal package relies on successful restoration of the strata and accurate identification of the depositional packages. Secondly, estimation of sea-level elevation through time requires careful identification of appropriate stratal terminations, and careful consideration of evidence for abnormal subaerial exposure of marine strata that occurs during forced regression, which is the only reliable indicator of relative sea-level fall. In the absence of abnormal subaerial exposure many stratal patterns can be equally well explained by sediment supply variations driving transgression and 'unforced' regression (Schlager, 1993). In addition, the process of determining coarse/fine ratio that accounts for each stratal package is iterative, which would be done by: (1) defining an initial guess for the coarse-grained proportion and running the forward model, (2) comparing the output with the observation and calculating the errors, (3) adjusting the initial values to reduce the errors, and then (4) running the model again and repeating this procedure until an acceptable match is achieved between the resulting model and observed architecture. Any inaccurate estimation of the controlling factors that account for the depositional packages can lead to the

production of an incorrect starting solution and hence an incorrect range of variations in stratal controls.

4.4 Baltimore Canyon: A Real-world Example

The techniques discussed above have been applied to interpret the Oligocene to Mid-Miocene stratigraphy from Baltimore Canyon Trough, offshore New Jersey. The Baltimore Canyon stratigraphy can be effectively viewed as a 2D system. A cross-section of the stratigraphy has been observed from a seismic reflection profile *Ewing* 9009, line 1003. The strata section is arranged into a series of 15 depositional packages according to the stratal line interpretation from Steckler et al. (1999), whereas the duration of the whole section is estimated to be 33.0 Ma to 11.5 Ma according to $\delta^{18}O$ record analysis from Miller et al. (1998). The seismic reflection profile of the stratigraphy, identification of depositional packages and the dating estimates are shown in fig. 4.8.

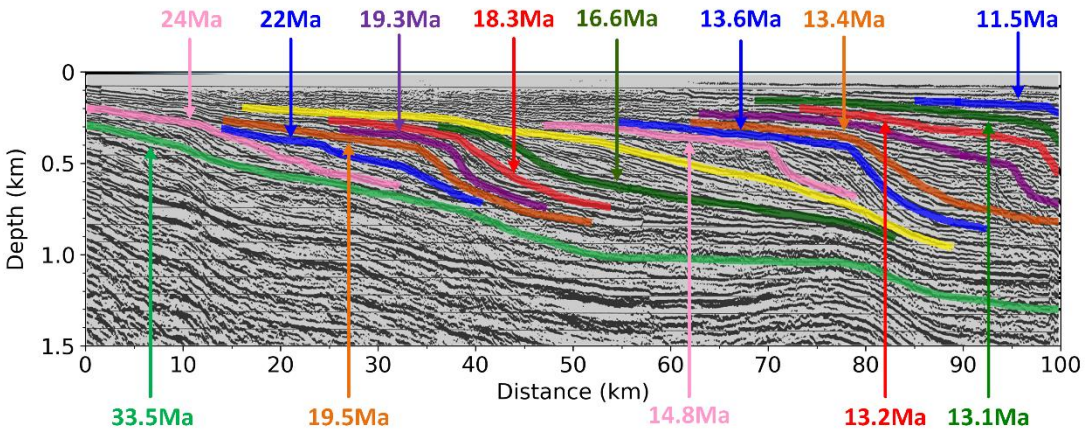

Figure 4.8 Sequence architecture of Baltimore Canyon Oligocene to Mid-Miocene stratigraphy observed from depth-converted seismic section Ewing 9009, line 1003 [modified from Steckler et al. (1999)].

The case study began with an arbitrary solution that assumes no erosion had occurred during the Baltimore Canyon stratigraphy development. The back-stripping approach was applied to remove the tectonic effects on the strata and to determine changes in relative sea-level, sediment supply and coarse/fine ratio through time. Dating estimates correlated with the depositional packages were then applied and therefore the curves of these controlling factors were produced (fig. 4.9A). Note that variations in the stratal controls during ages between each pair of the adjacent surfaces are still unknown. The three curves, incorporated with strata rotation angle though time determined from the back-stripping process, were then used to generate a synthetic architecture from the forward model (fig. 4.9B). Comparison of fig. 4.8 and Fig. 4.9B indicates that a good match has been achieved between the observed stratal geometry and the modelled section.

Next, subaerial erosion was introduced into the model and symmetry transformations were applied to adjust the input parameters for restoration of the resulting architecture. The increment of subaerial erosion rate in each step was set at 0.1 m/Myr. Figure 4.9C shows that when the erosion rate reached 30 m/Myr, the sediment supply rate at 15 Ma was found to be zero. This indicates the upper-bounds upon the subaerial erosion rate and upon the highest possible relative sea-level that could have existed during the strata growth. Compared with the original solution, differences in relative sea-level height can be up to 50 m during relative sea-level rising stage. This suggests that even a small change in the assumed subaerial erosion rate can leave a notable impact on the inferred palaeo-history. Note that, as discussed earlier, in the absence of dating estimated for the strata, the starting solution is also non-unique and can result in rather different solutions for the inference.

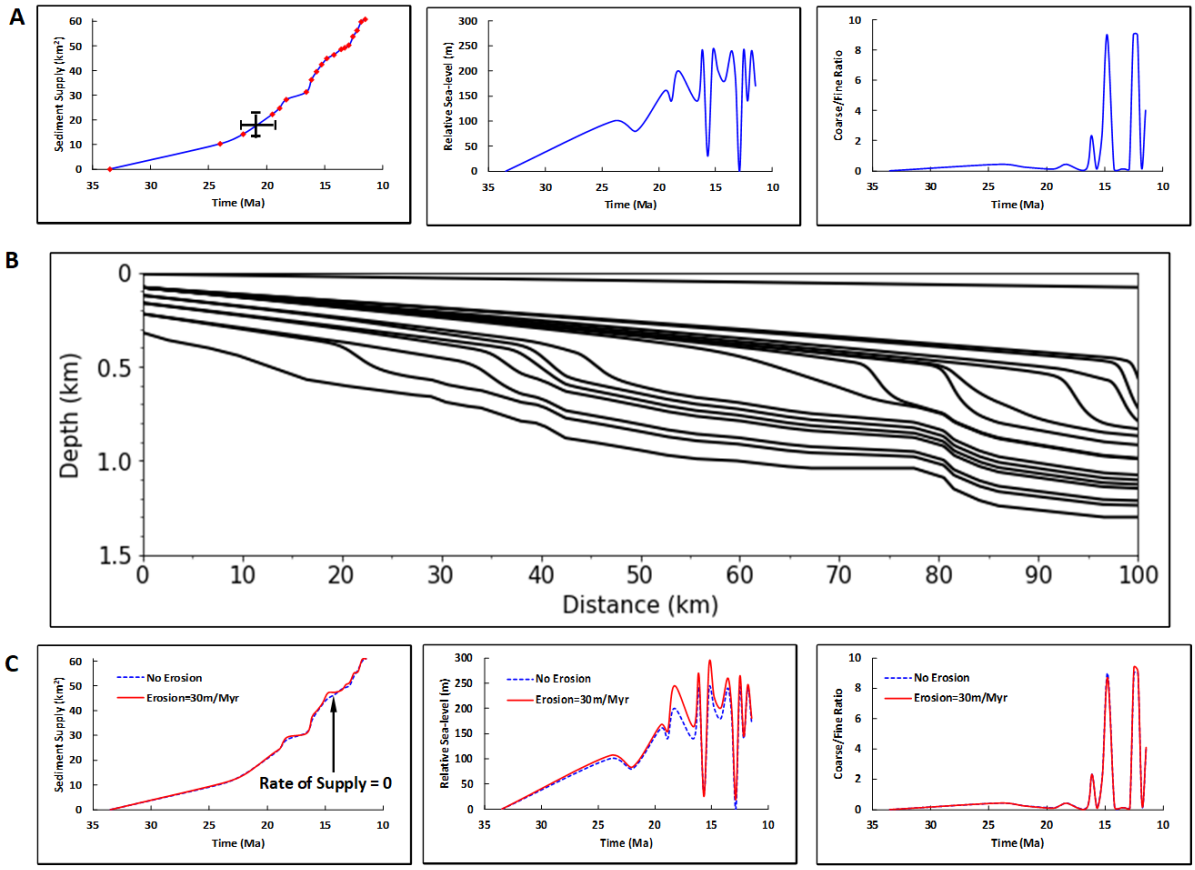

Figure 4.9 (A) A starting solution of sediment supply, relative sea-level and coarse/fine ratio from the Oligocene to Mid-Miocene reconstructed from Baltimore Canyon stratigraphy assuming no erosion. The inferred palaeo-history is constrained by dating estimates (makers shown on the sediment supply curve) for the strata. Conservative error bar on both timing and height are placed on the sediment supply curve to estimate the maximum variability one could infer from the observed data. (B) A synthetic architecture generated from a forward model using the starting solution. (C) An alternative solution that accounts for identical architecture is modified from the starting solution using the symmetry method. This solution indicates the upper-bounds upon relative sea-level height through time and upon the associated erosion rate. Note that Ma = millions of years ago (an age) and Myr = millions of years (a duration).

4.5 Discussion

Historically, geologists have realized that stratal geometries formed in siliciclastic shallow-marine environments are determined by the interaction of multiple controls, not just the accommodation. With the aid of quantitative forward models, stratal controls can be parameterized and then be used for stratigraphic simulations. Numerous attempts have been made to generate a solution that can produce a 'best-fit' model of the observed stratal geometry (e.g. Bornholdt et al., 1999; Cross and Lessenger, 1999; Wijns et al., 2004; Charvin et al., 2009a). However, any single solution found by these approaches can be considered a local optima (Burgess, 2012) and there are likely to be many others. Despite the awareness, entire exploration of the parameter space has not proved to be available, either using exhaustive searching approaches or by defining different starting guesses for the inversion algorithm.

This paper illustrates how to exploit the symmetry from a stratigraphic model and thus to transform an existing solution into the additional ones that can produce the same model outputs. However, as (Burton et al., 1987) claimed, it is impossible to determine the real solution from all possible solutions due to the absence of geological reason for distinguishing the effects of individual controls. Although all of these solutions appear to be possible, they may imply very different tectono-sedimentary processes and very different palaeo-history. Therefore, application of simple assumptions, such as constant sediment supply rate through time, is untenable. To rely on any single interpretation of a stratigraphy can lead to substantial uncertainties in the palaeo-history reconstruction. In an inverse problem, the conventional forward

modelling approach that a model conducts in constant time interval should also be avoided, since it implies an assumption that the time-steps between each of the stratal surfaces are identical. In comparison, a model that operates in cumulative sediment supply, same as the one employed in this work, is more appropriate in this context.

Nevertheless, discovery of useful information from stratigraphic inversion is possible. Transformation based on the principles of symmetry shows that all the solutions are closely related. In this work, for example, all sea-level curves produced from the same strata architecture have the same sequence of sea-level highstand/lowstand system tracts and only differ in their amplitude and durations. If dating estimates are available for the strata, the timing of highstands and lowstands also become constrained. Given the only requirement that sediment supply rate must be non-negative, quantitative limits can be placed on the relative sea-level amplitude and on the subaerial erosion rate. Properties calculated from the method that are common to all solutions must be true of the real solution whatever it is. This is similar to the conclusions of Heller et al. (1993) and Waltham and Gröcke (2006). However, although these investigated the joint effects of multiple controls and estimated the range of variations in the individual factors, both studies assumed that one of the multiple controls is dominant whilst the others either remain constant or change independently. Such an assumption is unlikely to be realistic in real-world geology since the various controls are often significantly correlated. Using symmetry transformation can overcome this problem well since multiple parameters can be

altered simultaneously and thus the competing effects of the stratal controls can be unravelled.

A real-case study has been conducted based on the subsurface data of Oligocene to Mid-Miocene deposits in Baltimore Canyon. Sequence architecture of the stratigraphy have been previously examined and several scenarios of eustasy, sediment supply history and tectonic history have been reconstructed (e.g. Posamentier et al., 1988; Van Wagoner et al., 1990; Miller et al., 1998). These interpretations have been verified using numerical models which prove that close matches were generated between the resulting model and the observation of strata (e.g. Lawrence et al., 1990; Schroeder and Greenlee, 1993; Poulsen et al., 1998; Steckler et al., 1999). However, model work presented here shows that an infinite number of alternative scenarios could be used to reproduce the same sequence architecture. Some differences can be observed between the inference herein and the scenarios of reconstruction in the previous studies, and the maximum relative sea-level and maximum erosion rate suggested here may not be necessary to explain the formation of the stratigraphic architecture. However, these make no contradiction to the issue that identical observations could be produced by different histories. Hence the whole range of solutions, rather than a single solution, should be considered in an interpretation. Nevertheless, several statements must be true according to the model work of Baltimore Canyon stratigraphy. Whatever the real solution is:

1. The stratigraphy has been shown to undergo a slight erosion subaerial erosion (erosion rate≤30 m/Myr) throughout the modelled period.

2. Two sharp changes (rapid fall followed by rapid rise) have been found in relative sea-level history, respectively at 16 Ma and 13 Ma.
3. Large proportions of coarse siliciclastic (coarse/fine ratio ≥8) have been shown to occur in 15 Ma and 12 Ma.

This paper also shows that increasing sophistication of a stratigraphic model could make the model less unique. In the simplest model (i.e. the one controlled only by sea-level change and sediment supply), given any appropriate sediment supply curve, there is a corresponding sea-level curve. If dating estimates for the stratal surfaces are available, then a particular sediment supply curve is defined and hence the corresponding sea-level curve can be found. However, once the subaerial erosion effect is introduced into the model, for each of the given subaerial erosion rates, there are an infinite number of apparent sediment supply curves, each of these has a corresponding sea-level curve. Therefore, the model becomes even less unique. Since the simulation of depositional system is significantly simplified compared with real-world geology, it is reasonable to suspect that stratigraphic interpretations could suffer from even more serious non-uniqueness when additional factors are included. As a useful tool, the principles of symmetry are general and simple enough to be widely applicable in higher dimensional and more sophisticated models. The symmetry method therefore bears great potential in the inference of palaeo-history from stratal geometries formed in various tectono-sedimentary settings observed from outcrop or subsurface.

4.6 Conclusions

Non-uniqueness is a key challenge in sequence stratigraphy. In this paper, a forward model of delta formation illustrates that the same stratal geometry can be generated using different combinations of parameters. The non-unique results suggest that the simplifying assumptions used in most current applications of the sequence stratigraphic method is untenable. However, the symmetry method proposed in this work here has been shown to be a useful tool for determining multiple controls on stratal geometries. In a stratigraphic model, symmetries provide rules for transforming model parameters in ways which leave the resulting geometry unaltered. Using this insight, it is possible to derive all possible solutions from an existing solution. Calculation of multiple solutions can allow properties common to all solutions, and hence to the unknown correct one, to be found. Consequently, application of the symmetry method offers more complete solutions to the interpretation of stratal geometries and hence more predictive power. Application of the method also allows more robust interpretation of the controls on strata geometries and hence generation of more reliable data, for example for palaeo-climate studies.

4.7 Acknowledgement

Associate Editor Mariano Marzo and two reviewers, Gary Nichols and Kerry Gallagher, are thanked for their valuable comments that greatly helped to strengthen the manuscript. The authors would like to thank Saswata Hier-Majumder and YunPeng

Wang for their useful discussions during the manuscript preparation. Jie Xiao acknowledges the support provided by China Scholarship Council (CSC).

5 Practical Insights into Non-unique Thermal Histories in Sedimentary Basins Reconstructed from Vitrinite Reflectance

J. Xiao[a, b, c], D. Waltham[b], and Y. Wang[a, *]

(a) State Key Laboratory of Organic Geochemistry, Guangzhou Institute of Geochemistry, Chinese Academy of Sciences, Guangzhou 510640, China

(b) Department of Earth Sciences, Royal Holloway University of London, Egham, Surrey TW20 0EX, UK

(c) University of Chinese Academy of Sciences, Beijing 100049, China

* Corresponding author (wangyp@gig.ac.cn)

Author statement

This chapter is written in a format of journal article and is in preparation for publication. The manuscript of this article has 39 pages in total, with 5,315 words (including the title, abstract and main text, but excluding the references and figure captions) and 11 figures. The thesis author was the primary investigator and lead author of this work. His contributions to this work are summarized as follows:

(1) Conceptualization: formulation of the overarching research objectives and aims;

(2) Methodology: development of the methodology; creation of the forward and inverse models;

(3) Software: designing the computer programs;

(4) Investigation: interpretation of geological and geothermal datasets from central Sichuan Basin, China; conducting the synthetic and real-data examples of thermal history modelling;

(5) Writing: creation of a complete first draft.

5.1 Abstract

Reconstructing thermal history in a sedimentary basin depends on successful application of the inverse method. Thermal indicators, for example downhole vitrinite maturation, are observed and subsurface temperature in the past deduced. However, inverse methods usually produce non-unique solutions because different histories could produce the same observations. This paper demonstrates a numerical approach to tackling the issue of non-uniqueness. Application of the approach begins with a simple solution that gives a close match between the model and the reality. The simple, initial solution is then transformed into alternative solutions that give the same model. Using the proposed method, a real-case study is carried out on the thermal history of central Sichuan Basin, SW China. Modelling results show that, the vitrinite maturation in the region nowadays can be either a consequence of a sharp, short-lived event in Permian or a consequence of slow, long-term paleo-heat flow evolution. However, calculation of end-member solutions confirms that the basin must have experienced unusually high temperature during Mid to Late Permian since a thermal anomaly is present, at that time, in every possible model scenario.

5.2 Introduction

The thermal history in a sedimentary basin is a key control on organic maturation and hydrocarbon generation (Waples, 1980; Tissot et al., 1987). Reconstruction of thermal history has been an ongoing concern in basin analysis and assessment of petroleum prospect. Vitrinite reflectance of organic matter buried in sediments is

perhaps the most frequently used thermal indicator (e.g. Bray et al., 1992; Zhao et al., 1996; Uysal et al., 2000; George et al., 2001), due to its close correlation with progressive organic maturities in response to temperature variations (McKenzie, 1981; Ritter, 1984; Pittion and Pradier, 1986; Barker and Pawlewicz, 1994). However, neither vitrinite reflectance nor other thermal indicators unequivocally reveals the thermal history because more than one history could give rise to identical measurements at present. That is, solutions to the thermal history are non-unique.

Subsurface temperature beneath a basin is determined by a variety of controlling factors, in particular the depth and lithologies of sedimentary layers, heat flow from below and temperature at the subaerial interface or seafloor (Welte et al., 2012; Allen and Allen, 2013). The non-uniqueness arises since there are a number of free parameters to deduce whereas the only observations available are the present-day vitrinite reflectance. Supplementary knowledge of the multiple factors is often adopted to reduce the number of unknowns. For instance, the tectonic evolution of a sedimentary basin can be inferred using general subsidence models (e.g. McKenzie, 1978). The thermal conductivities of rocks can be estimated either in the field (e.g. Beck et al., 1971; Conaway and Beck, 1977), in a laboratory (e.g. Sass et al., 1984) or from empirical calibration (e.g. Vasseur et al., 1995). In addition, the historical surface temperature can be deduced from paleoclimate. Having these factors specified, the inverse problem is simply to infer heat flow variations in the past. However, the problem is still challenging because what thermal indicators record is the cumulative thermal exposure of a sample, rather than the individual variations in temperature.

Resolving the thermal history uniquely proves to be impossible since different sequences of temperature variations could yield the same results.

Practically, reconstruction of thermal histories often ends up with quantitative basin modelling. Tectono-sedimentary processes in a depositional system are mathematically expressed by a forward numerical model and thermal indicator data in response are then predicted from prescribed geological and geothermal conditions. Embedded with an inverse scheme, a forward model can be alternatively used to deduce the thermal history from data observed. In stark contrast to the forward model that is built upon rigorous mathematical functions, an inverse problem is usually solved by stochastic algorithms. Example of these include the Constrained Random Search (Willett, 1997), Markov Chain Monte Carlo (MCMC, Ferrero and Gallagher, 2002), hierarchical Bayesian models (Wang and Zabaras, 2004), MCMC sampling (Gallagher et al., 2009) and Bayesian transdimensional MCMC (Gallagher, 2012). These methods have shown capabilities in generating particular solutions that account for the observations. In reality, however, there are likely to be many other solutions, each of which has large uncertainties leading to substantial risk in petroleum exploration and development of fields.

In an attempt to address the non-unique problems, it has been often suggested that a representative ensemble of solutions, rather than a single solution, should be used. Consideration of multiple solutions allows the properties that are common to the multiple scenarios to be found and, meanwhile, allows the interpretations that are physically unreasonable to be eliminated. This idea has been applied in many aspects

of geology such as sedimentology (Heller et al., 1993), thermochronology (Nielsen, 1995), geochemistry (Waltham and Gröcke, 2006), stratigraphy (Waltham et al., 2008) and seismology (Sambridge et al., 2013). Using a stratigraphic model, Xiao and Waltham (2019) demonstrated that the whole set of solutions are closely correlated and thus an existing solution can be directly transformed into another solution. The transformation between multiple solutions can be thought of as utilizing the implicit symmetry of a model, in the same way that rotating a square by 90 degrees gives exactly the same geometry.

In this paper, we present a novel application of the symmetry idea in geology by exploring the symmetry of a 1-D forward model of downhole vitrinite reflectance. Principle controls incorporated in the model include tectonic subsidence and uplift, heat flow variations, thermal conductivities and surface temperature. A simple, initial solution to the thermal history is first generated from which additional solutions are derived using the rules of symmetry. The model is then used to investigate thermal evolution in the Sichuan Basin, SW China, with a focus on a suspected heat flow spike during Mid to Late Permian.

5.3 The Forward Problem

A numerical forward model is employed here to estimate reflectance of vitrinite particles buried in a sedimentary basin. The forward modelling scheme can be divided into three steps. First, we calculate subsurface temperatures in the past at various depth beneath the basin. Organic reaction within sediments is then simulated and

thermal maturities at present predicted. Eventually, the results of organic thermal maturities are converted into vitrinite reflectance data using established empirical calibration. The forward modelling product is a profile of vitrinite reflectance along a sedimentary pile. The effects of convection and advection are excluded from the forward model as these are likely insignificant in the crust. Radiative heat transfer is also neglected since the impact it leaves on near-surface heat flow is less than a few $mW \cdot m^{-2}$ (Gallagher, 1988). Hence, the thermal maturation in the 1-D model only depends on vertical transfer of conductive heat. Crucially, as will be shown in later sections, the inverse method proposed does not rely on any characteristic of the forward model as the method is entirely general. Hence, the forward model can be recreated to be more sophisticated and to be spatially 2-D or 3-D.

Assuming a stationary temperature field with no source terms, the heat flow within a sedimentary pile at any time can be effectively considered to be depth-independent. This assumption is tenable for sedimentary basins with slow or moderate sedimentation rates (≤ 500 $m \cdot Myr^{-1}$) (Gallagher and Sambridge, 1992). Mathematically, the independence of heat flow can be expressed by the steady-state energy equation of Bullard (1954)

$$\frac{\mathrm{d}}{\mathrm{d}z}\left[k(z)\frac{\mathrm{d}T}{\mathrm{d}z}\right] = 0 \tag{5.1}$$

, where z is depth, $k(z)$ is thermal conductivity at z and T is temperature. Application of eq. 5.1 to sedimentary basin modelling requires specification of boundary conditions. The upper boundary condition at z = 0 of a sedimentary pile is

given by the surface temperature. The temperature at depth z in time t can then be approximated by an integration of heat flow over depth

$$T(z,t) = T_s + Q(t)\int_0^z \frac{dz'}{k(z')} \quad (5.2)$$

, where T_s is the surface temperature and $Q(t)$ is the heat flow in time t. The surface temperature is assumed to be constant over time. As the heat transfers from base to top of the sedimentary pile, the values of $Q(t)$ are set to be positive upwards. The depth of a sedimentary layer through time is given by the burial history in the basin. The thermal conductivities depend upon porosities and compaction factors of sedimentary rocks. To derive thermal variables of sedimentary layers, we follow the model of Beck (1976) that calculates the thermal conductivity as an average of the Maxwell model and geometric mean of solid and fluid thermal conductivities.

The subsurface temperatures calculated from eq. 5.2 are then used to predict thermal maturities of organic matters. This can be done by calculating the time-temperature index (TTI), a concept that was firstly proposed by Royden et al. (1980) for measuring the maturities of organic matters. The TTI of a sample is generally expressed as a time-temperature integral, where the thermal maturity shows a linear dependence on duration of time and an exponential dependence on temperature

$$\mathrm{TTI} = \int_0^t N^{[\alpha T(t')+\beta]}\, dt' \quad (5.3)$$

, where t is time in Ma, $T(t')$ is the temperature in °C in time t' ($0 \le t' \le t$) and α, β and N are constants. The constants α and β determine the significance of temperature to organic reaction rates. We set α = 0.1 and β = -10.5 as McKenzie

(1981) suggested, which implies organic reaction rate doubles for every 10°C rise in temperature and that rapid reaction occurs within the oil window (i.e. ~50° – 150°C). The constant N determines the relative dependences of TTI on temperature and on duration. In this paper, we set N = 2, presuming a dominant control of temperature on TTI.

The TTI estimated from eq. 5.3 then works as a proxy that allows prediction of vitrinite reflectance to be generated. The reflectance of vitrinite is defined as the percentage of reflected light intensity from the normal incident light intensity measured under oil (Stach et al., 1982). The general form of logarithm calibration between vitrinite reflectance and TTI can be written as

$$\ln(R_{\mathrm{o}}) = p \ln(\mathrm{TTI}) + q \tag{5.4}$$

, where R_{o} is the vitrinite reflectance in percentage, p and q are constants empirically derived. In this work, we set p = 0.173 and q = - 2.242 as proposed by De Bremaecker (1983). Using the above treatments, the forward numerical model is therefore set up. Numerical solutions of the forward model can be found in Gallagher and Sambridge (1992). For more details of the forward model, see the reference cited.

5.4 The Inverse Problem

5.4.1 Unique and non-unique thermal histories

In the context of thermal history modelling, a solution to an inverse problem is defined by a set of parameters that enable a good match from a forward model to observed data. The schematic in fig. 5.1 illustrates the simplest case of thermal history

reconstruction where sediment infill to the basin is continuous and erosion is absent. As shown in the schematic, two sedimentary layers, namely h_1 and h_2, are identified in the at depth z_1 and z_2 of a borehole. The ages of h_1 and h_2, namely t_1 and t_2 (t_0 as present day), can be estimated in case dating estimates are available, which allow burial paths of sediments to be reconstructed (fig. 5.1a). Vitrinite reflectance at z_1 and z_2 can be measured from a borehole, giving a vitrinite reflectance vs. depth profile (fig. 5.1b). For simplification, temperature at the seafloor is assumed to be constant in time, although in reality it may vary a few tens of °C in millions of years. With the burial history and surface temperature specified, the inverse problem is simply to infer paleo-heat flow in t_1 and t_2. This would be done by a simple approach, similar to the thermal backstripping of Lerche et al. (1984):

i. Since $R_o(z_1)$ is governed by heat flow variations from t_1 to date and provided that present-day heat flow $Q(t_0)$ can be estimated from the borehole, we can calculate the heat flow in t_1 by trying different values for $Q(t_1)$ in the forward model until the model prediction fits well with $R_o(z_1)$.

ii. Successful application of step (i) allows $Q(t_1)$ to be resolved. We then look at $R_o(z_2)$, which is determined by the rates of heat flow from t_2 until present. Given the heat flow values $Q(t_0)$ and $Q(t_1)$, we follow the same manner as in step (i) and deduce $Q(t_2)$ by iterations of model fitting.

iii. Having the heat flow in t_1 and t_2 resolved, the history of paleo-heat flow can be found by the trajectory through the heat flow vs. time nodes (i.e. $Q - t$ nodes).

As shown in fig. 5.1c, a heat flow vs. time curve can be produced by connecting $Q(t_0)$, $Q(t_1)$ and $Q(t_2)$.

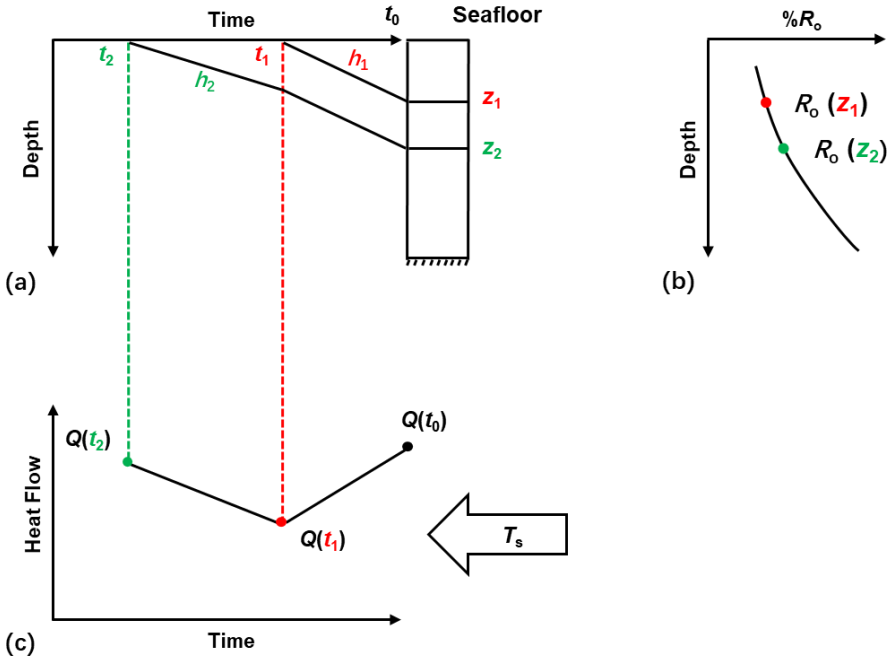

Figure 5.1 Reconstructing thermal history in a synthetic basin with continuous sediment infill but no erosion. (a) Burial paths of sedimentary layers $\boldsymbol{h_1}$ and $\boldsymbol{h_2}$ that originally deposited in time $\boldsymbol{t_1}$ and $\boldsymbol{t_2}$ and that are located at depth $\boldsymbol{z_1}$ and $\boldsymbol{z_2}$ today, respectively. (b) Downhole measurements of present-day vitrinite reflectance $\boldsymbol{R_o}$. (c) The heat flow history inferred from (a) and (b). The surface temperature $\boldsymbol{T_s}$ is set to be constant through time.

For the very simple example presented above, application of the conventional thermal backstripping approach may adequately solve heat flow in the past. However, the argument above breaks down for more realistic basins where erosion, uplift or depositional hiatus are involved. This idea is illustrated in fig. 5.2, with identical borehole observations to the previous example except for an unconformity located at

depth z_e ($0 < z_1 < z_e < z_2$), indicating a period of erosion from t_e to t_1 ($t_2 < t_e < t_1 < t_0$). It is not possible to unequivocally determine $Q(t_e)$ and $Q(t_2)$ that are constrained by the only measurement of $R_o(z_2)$, i.e. problem is under-determined.

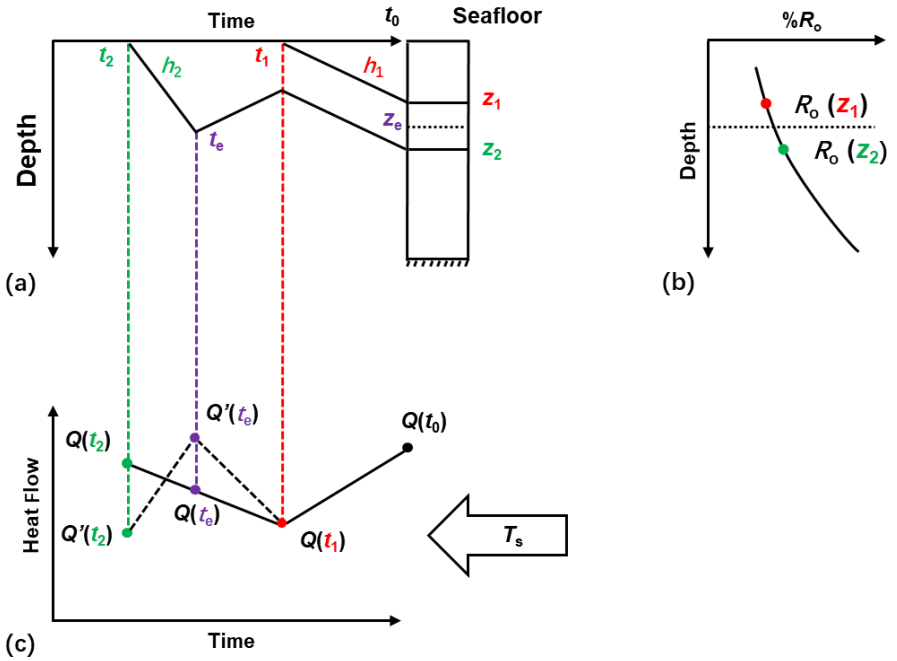

Figure 5.2 Non-unique solutions produced by backstripping the borehole data for a more realistic basin where erosion events took place. (a) Burial history of two sedimentary layers $\boldsymbol{h_1}$ and $\boldsymbol{h_2}$ that originally deposited in time $\boldsymbol{t_1}$ and $\boldsymbol{t_2}$, respectively. These layers subsided continuously except for an erosion event took place in time $\boldsymbol{t_e}$, forming an unconformity at $\boldsymbol{z_e}$. (b) A downhole profile of vitrinite reflectance. (c) Multiple histories of heat flow are found, indicating the non-uniqueness.

A new inversion procedure, revised from the thermal backstripping approach, is proposed in fig. 5.3. In order to retain the usefulness of the thermal backstripping, one may temporally ignore the influence of erosion, uplift and hiatus on paleo-heat flow,

assuming a constant gradient of heat flow change during t_2 and t_1. This simplifying assumption has the advantage that it allows the heat flow in t_2 and t_1 to be deduced as in the previous example. Connecting the heat flow rates in t_2, t_1 and t_0 then gives an apparent heat flow curve (fig. 5.3c). Subsequently, a new *Q* – *t* node for time t_e is created on the heat flow curve (fig. 5.3d), and hence a simple, initial solution to the inverse problem is generated. Note that this is not a unique solution because additional solutions may be derived by appropriately modifying the initial heat flow curve. This would be done by moving the *Q* – *t* nodes prior to t_e upwards (heat flow increases) or downwards (heat flow decreases).

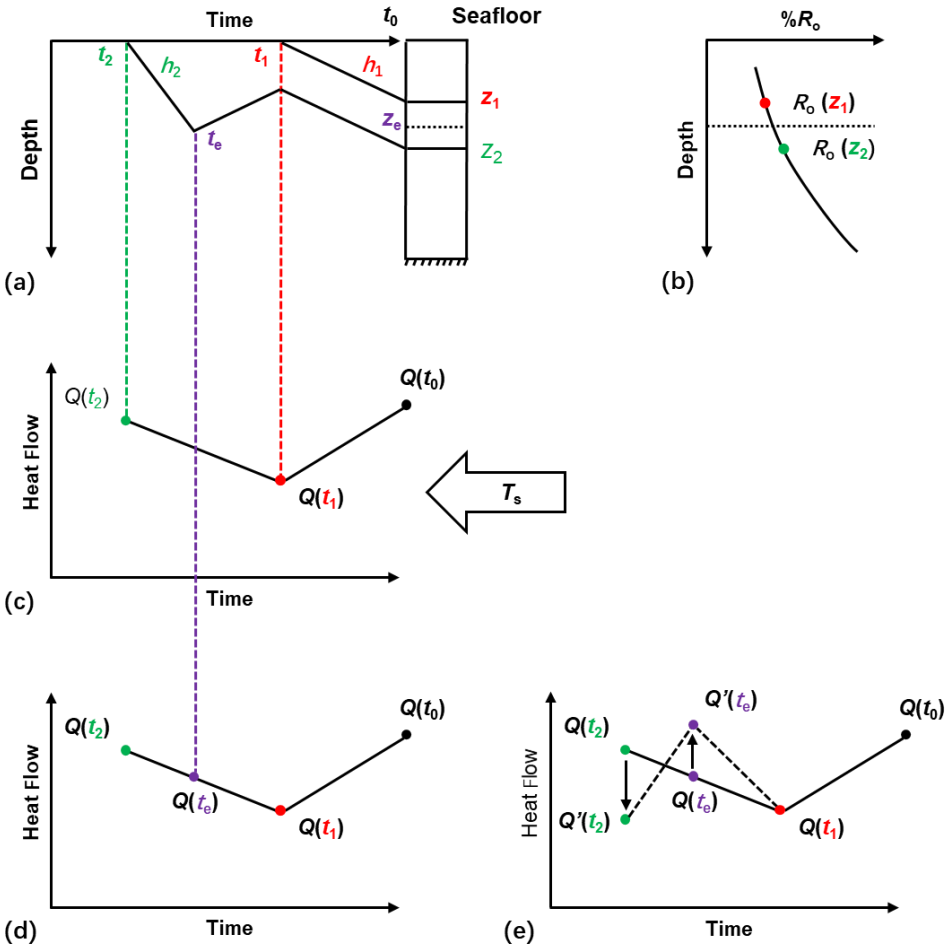

Figure 5.3 Determining non-unique heat flow histories from vitrinite reflectance data. (a) Burial paths of sedimentary layers same as in fig. 5.2a. (b) A downhole profile of vitrinite reflectance. (c) An initial heat flow (vs. time) curve where heat flow fluctuations during erosion event are ignored. (d) A new node $\boldsymbol{Q(t_e)}$ is inserted to the initial heat flow curve. (e) Additional heat flow curves can be found by properly modifying the initial curve.

5.4.2 Calculating multiple solutions: a numerical approach

We now investigate how to derive additional solutions, from an initial heat flow curve, to reproduce the identical model. No analytical tool is available for this task since the forward model is non-linear. Instead, a numerical approach is developed. Numerically, a heat flow history may be represented by a model vector of length *P*

$$\boldsymbol{x} = (x_1, x_2, \ldots, x_P)^{\mathrm{T}} \tag{5.5}$$

, where x_1, x_2, …, x_P are heat flow at different time and *P* is given by the total number of horizons plus unconformities. Similarly, the resulting vitrinite reflectance profile may be represented by a data vector of length *d*

$$\boldsymbol{y} = (y_1, y_2, \ldots, y_D)^{\mathrm{T}} \tag{5.6}$$

, where y_1, y_2, …, y_D are vitrinite reflectance data at various depth and *D* is given by the number of horizons. As discussed earlier, *P* = *D* in the simplest, non-erosive model while *P* > *D* in more sophisticated examples. For more realistic model work the latter case is expected. A general relationship between $\boldsymbol{x}$ and $\boldsymbol{y}$ may written as

$$\boldsymbol{y} = \boldsymbol{F}(\boldsymbol{x}) \tag{5.7}$$

, where $\boldsymbol{F}$ denotes a non-linear function. Therefore, once a good solution $\boldsymbol{x}$ (i.e. an initial heat flow curve that produces the desired model) is found, an alternative solution $\boldsymbol{x}'$ to the same model can be found by $\boldsymbol{F}(\boldsymbol{x}') = \boldsymbol{F}(\boldsymbol{x})$. We calculate $\boldsymbol{x}'$ using a linearization approach. The difference in model prediction $\boldsymbol{F}(\boldsymbol{x})$ can be approximated in a linear form by considering small changes $\delta\boldsymbol{x}$ in the parameters, i.e.

$$\boldsymbol{F}(\boldsymbol{x} + \delta\boldsymbol{x}) = \boldsymbol{F}(\boldsymbol{x}) + \mathrm{A}\delta\boldsymbol{x} \tag{5.8}$$

, where A is a matrix of partial derivatives indicating the changes in $\boldsymbol{F}(\boldsymbol{x})$ with respect to changes in $\boldsymbol{x}$, i.e.

$$A_{ij} = \frac{\partial F_i}{\partial x_j} \tag{5.9}$$

, where i = 1, 2, …, *D* and j = 1, 2, …, *P*. Elements of matrix A can be derived from the forward model using a finite difference approach. That is, we first run the default model $\boldsymbol{F}(\boldsymbol{x})$ and then run the model again for *P* times. For each time, we give small changes to the j-th element in $\boldsymbol{x}$ and determine changes occur in model prediction.

If $\boldsymbol{x}' = \boldsymbol{x} + \delta\boldsymbol{x}$ is another solution in addition to $\boldsymbol{F}(\boldsymbol{x})$, then vector $\delta\boldsymbol{x}$ is given by $\boldsymbol{F}(\boldsymbol{x} + \delta\boldsymbol{x}) = \boldsymbol{F}(\boldsymbol{x})$ subject to the constraint imposed by eq. 5.8 (i.e. $\mathrm{A}\delta\boldsymbol{x} = \boldsymbol{0}$). In order to prevent unjustified fluctuations in the new solution, $\boldsymbol{x}'$ with the least complications is chosen. The roughness of vector $\boldsymbol{x}$ can be estimated from the finite difference of the first (R_1) and second (R_2) derivatives, similar to the approach of Constable et al. (1987), i.e.

$$R_1 = \sum_{j=2}^{P} \left(\frac{x_j - x_{j-1}}{t_j - t_{j-1}} \right)^2 \tag{5.10}$$

and

$$R_2 = \sum_{j=2}^{P-1} \left(\frac{x_{j+1} - x_j}{t_{j+1} - t_j} - \frac{x_j - x_{j-1}}{t_j - t_{j-1}} \right)^2 \tag{5.11}$$

In matrix notation, the roughness of vector $\boldsymbol{x}$ may be written as $\boldsymbol{x}^{\mathrm{T}}\mathrm{D}^{\mathrm{T}}\mathrm{D}\boldsymbol{x}$, where D is a matrix of associated coefficients given by eq. 5.10 (for 1st derivative smoothing) or eq. 5.11 (for 2nd derivative smoothing).

The calculation of an additional solution can be treated as a compromise between reducing the solution roughness, accepting inaccuracy in the model, or reducing the model fitness, accepting complications in the solution. The trade-off between squared model misfit and solution roughness is expressed as

$$T(\theta) = (\boldsymbol{x} + \delta\boldsymbol{x})^{\mathrm{T}}\mathrm{D}^{\mathrm{T}}\mathrm{D}(\boldsymbol{x} + \delta\boldsymbol{x}) + \theta^2\delta\boldsymbol{x}^{\mathrm{T}}\mathrm{A}^{\mathrm{T}}\mathrm{A}\delta\boldsymbol{x} \quad (5.12)$$

, where θ is an unknown parameter determining the relative importance of the misfit and the roughness and is squared only to ensure it is non-negative. Large values (10^3 in this work) are suggested for θ to avoid large disagreement between $\boldsymbol{F}(\boldsymbol{x} + \delta\boldsymbol{x})$ and $\boldsymbol{F}(\boldsymbol{x})$. The minimum of the trade-off function can be found by setting

$$\frac{\partial T}{\partial \delta\boldsymbol{x}} = \mathrm{D}^{\mathrm{T}}\mathrm{D}(\boldsymbol{x} + \delta\boldsymbol{x}) + \theta^2\mathrm{A}^{\mathrm{T}}\mathrm{A}\delta\boldsymbol{x} = 0 \quad (5.13)$$

, which gives

$$\delta\boldsymbol{x} = -(\theta^2\mathrm{A}^{\mathrm{T}}\mathrm{A} + \mathrm{D}^{\mathrm{T}}\mathrm{D})^{-1}\mathrm{D}^{\mathrm{T}}\mathrm{D}\boldsymbol{x} \quad (5.14)$$

The above treatments allow the initial solution to be transformed into a new solution with smaller 1st (or 2nd) derivatives, namely 1st (or 2nd) derivative smoothing. The new solution would be used to form the basis of further transformation. The procedure may iterate until $\delta\boldsymbol{x}$ falls below a prescribed threshold (e.g. $\delta\boldsymbol{x}$ = 10^{-3} mW·m^{-2} as applied here), showing the failure to produce further changes in vector $\boldsymbol{x}$. For the k-th iteration, the new solution is given by $\boldsymbol{x}_{k+1} = \boldsymbol{x}_k + \delta\boldsymbol{x}_{k+1}$, where $\boldsymbol{x}_k$ is the current solution and $\delta\boldsymbol{x}_{k+1}$ denotes the required changes. Note that coefficients in matrices A and D must be recomputed for each iteration because the vector $\boldsymbol{x}$ has changed.

5.4.3 Determining universal properties of non-unique solutions

A forward modelling example is presented to demonstrate the transformation approach described above. As shown in fig. 5.4, we first run the forward model

outlined in Section 5.3, with synthetic geologic (fig. 5.4a) and geothermal (fig. 5.4b) histories during basin evolution. Corresponding subsurface temperature through time (fig. 5.4c) and downhole vitrinite reflectance nowadays (fig. 5.4d) are then estimated from the forward model. Next, we calculate other heat flow vs. time curves than that in fig. 5.4b. Using the numerical approach, an existing solution can be symmetrically altered into an alternative, smoother solution, whilst leaving the model prediction unchanged. Repetitive application of the approach allows inessential complications to be removed from the initial heat flow curves, and hence a range of additional solutions to be derived. Though these solutions differ with each other, they all reproduce the identical vitrinite reflectance profile.

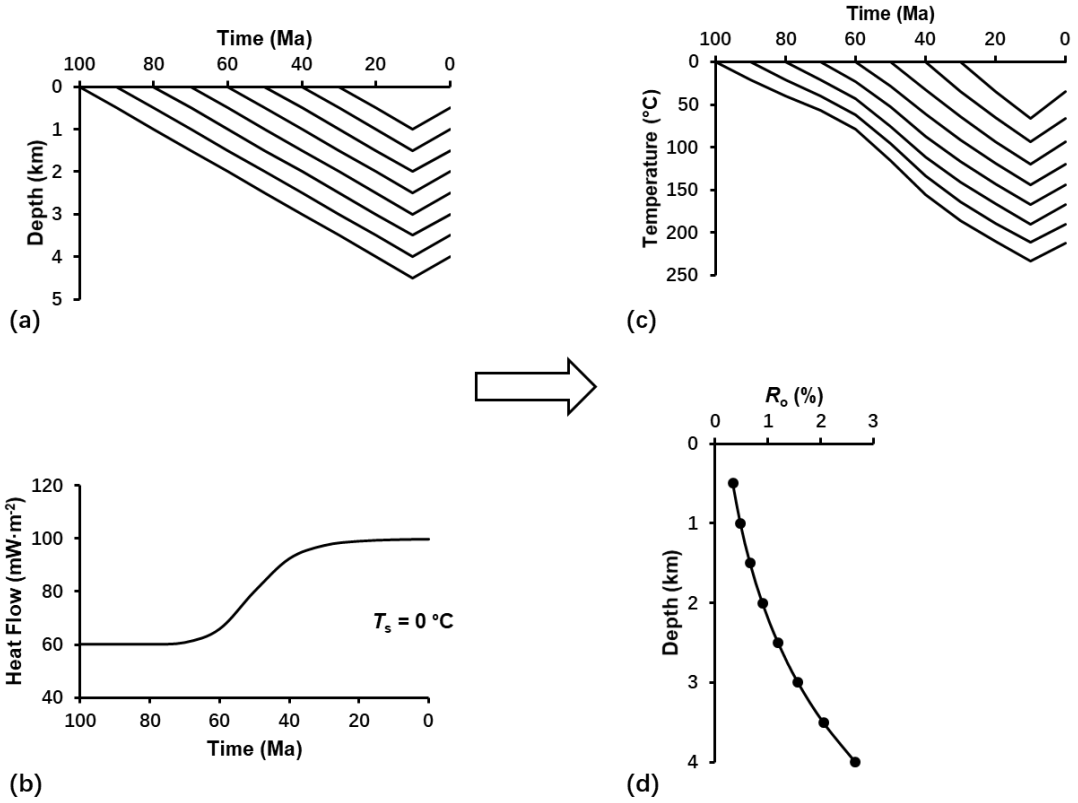

Figure 5.4 Forward modelling results for subsurface temperature and vitrinite reflectance. (a) Synthetic burial paths of sedimentary layers in a basin with continuous sediment infill since 100 Ma except for an erosion event in the recent 10 Ma. (b) Heat flow evolution in the basin through time and a constant surface temperature of 0 °C. (c) Prediction of subsurface temperature of the sedimentary layers. (d) Prediction of present-day downhole vitrinite reflectance at various depth.

Among the whole set of heat flow curves, the end-member solutions with the smallest 1st and 2nd derivatives, are displayed fig. 5.5 and fig. 5.6, respectively. Both end-member solutions show similar heat flow fluctuations to the initial heat flow curve in the recent 40 million years. However, these end-member solutions differ significantly in the earlier periods compared to the initial solution, where it is shown that the heat flow remained 60 mW·m^{-2} in the first 30 million years and rose sharply to

100 mW·m^{-2} between 70 and 30 Ma. In contrast, the 1st derivative smoothest solution (fig. 5.5) suggests the heat flow remained around 90 mW·m^{-2} throughout the 20 million years. In terms of the 2nd derivative smoothest solution (fig. 5.6), it is shown that the heat flow initiated at approximately 50 mW·m^{-2} in 100 Ma and increased gradually to nearly 100 mW·m^{-2} in 30 Ma. Nevertheless, all these solutions indicate that the heat flow in the synthetic basin has remained around 100 mW·m^{-2} in recent 40 Ma.

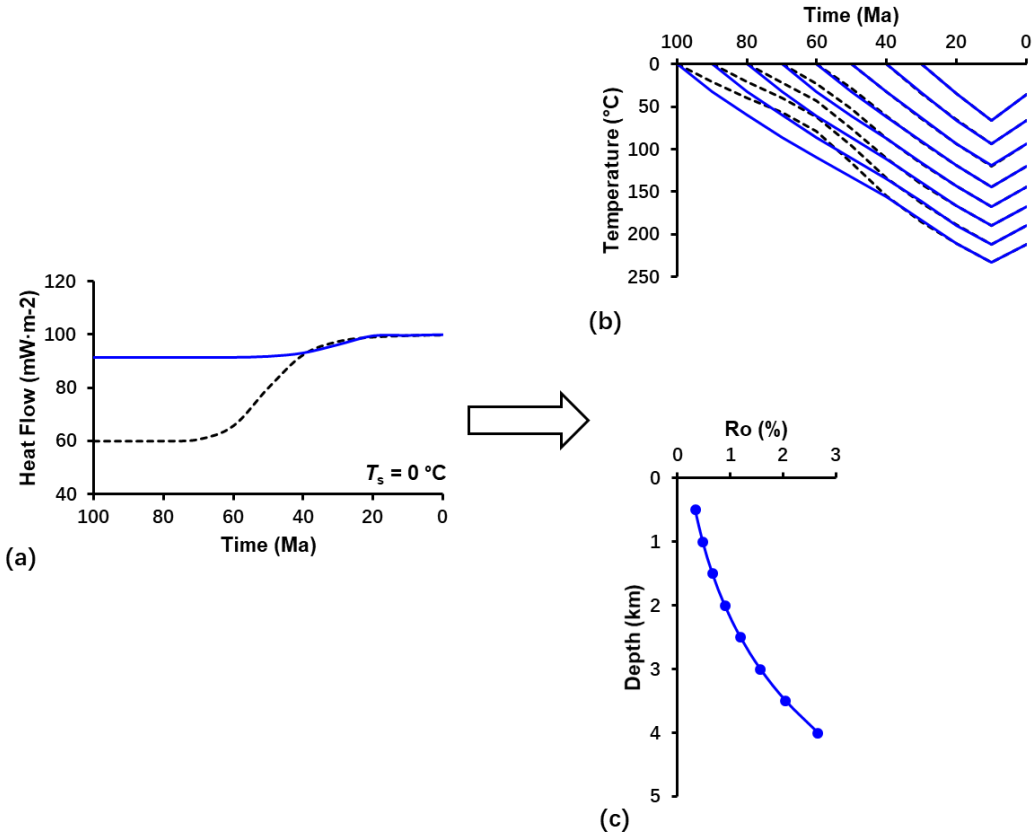

Figure 5.5 (a) An end-member solution (blue solid curve), with the smallest 1st derivative, derived from the initial solution (black dashed curve). (b) Subsurface temperature modelled from the end member solution (blue solid curve) and from the initial solution (black dashed curve). (c) Vitrinite

reflectance profile modelled from the end-member solution is exactly the same to that in fig. 5.4d. Other details as in fig. 5.4.

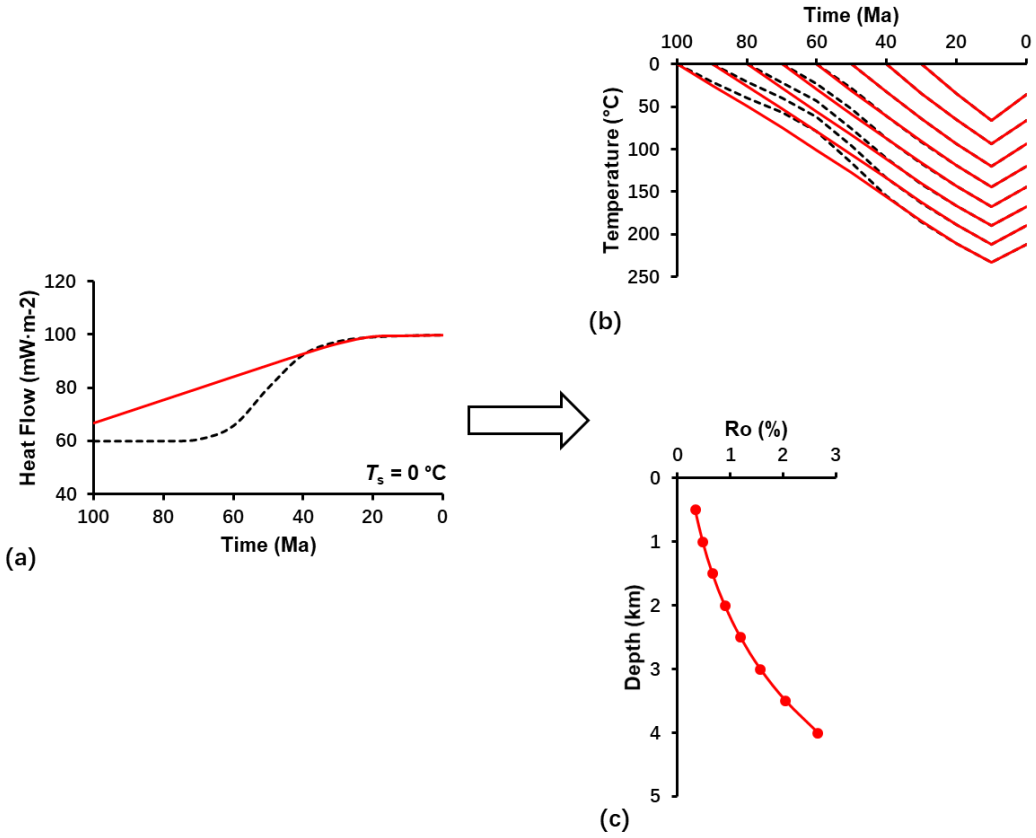

Figure 5.6 (a) An end-member solution (red solid curve), with the smallest 2nd derivative, derived from the initial solution (black dashed curve). (b) Subsurface temperature modelled from the end member solution (red solid curve) and from the initial solution (black dashed curve). (c) Vitrinite reflectance profile modelled from the end-member solution is exactly the same to that in fig. 5.4d. Other details as in fig. 5.4.

Using the ideas described above, a novel inverse method can be proposed as in fig. 5.7. The inversion procedure can begin with reconstructing the burial history in a sedimentary basin from borehole observations. With the influence of erosion, uplift

and hiatus temporally neglected, an initial heat flow curve is then generated using the thermal backstripping approach. Combination of the burial history and the initial heat flow curve would make the synthetic vitrinite reflectance generated from the forward model conform closely to real data. Next, the symmetry transformation approach is applied iteratively to calculate alternative heat flow curves that can reproduce the same model work. The iterations finally allow end-member solutions that have the smoothest structures to be discovered. Such end-member solutions, by definition, contain no unwarranted fluctuations to explain the present-day thermal indicators. In other word, application of the transformation approach can unravel paleo-heat flow variations that must be true to the unknown, real history, despite the solutions are non-unique.

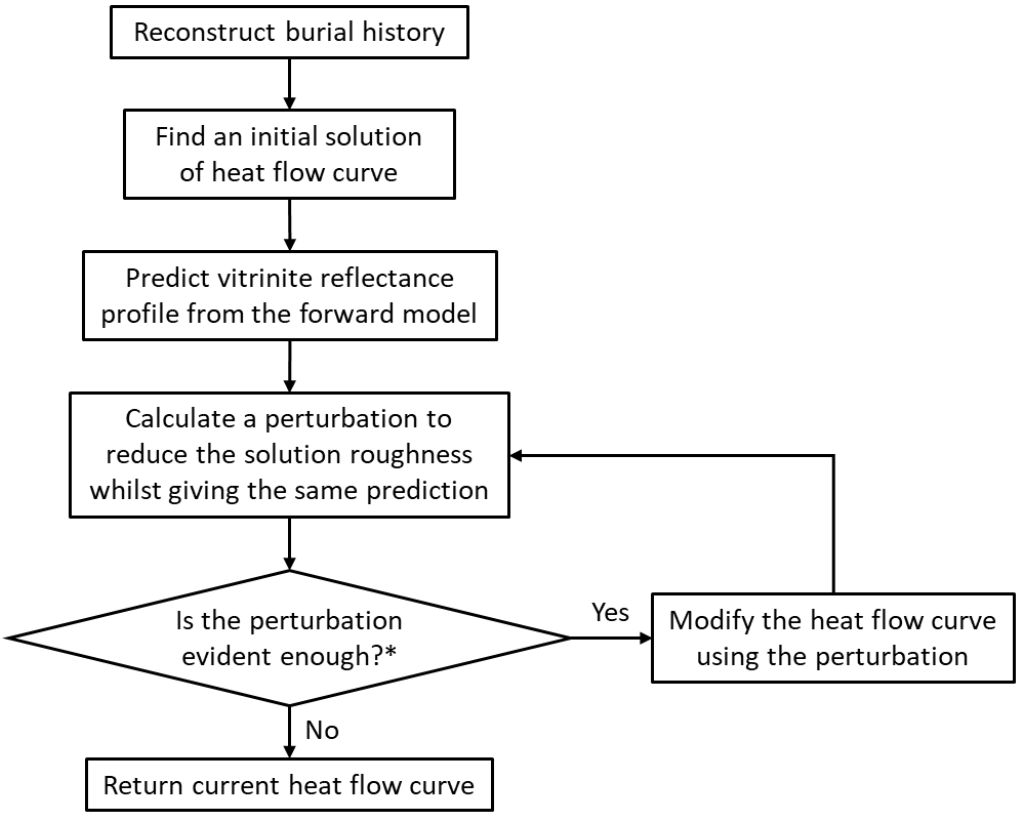

Figure 5.7 Calculation of the smoothest heat flow histories to explain the downhole vitrinite reflectance data at present. *NB: A threshold value is prescribed to determine the significance of the perturbation.

5.5 A Real-data Example

The inverse method, based on the principle of symmetry, is applied to investigate the thermal history in the Sichuan Basin, SW China. The Sichuan Basin is located in the western Yangtze Craton, covering ~2.3×10^5 km^2. The tectonic evolution in the basin has been relatively simple since Neoproterozoic, except for the extensive erosion and uplift during the North China – South China collision in Mid Triassic and the Indo – Asian collision during Cenozoic. Previous studies have supposed a sharp escalation in paleo-heat flow between Mid to Late Permian triggered by mantle plumes beneath the Emeishan region to the southwest of the basin (e.g. Zhu et al., 2010; He et al., 2011;

Jiang et al., 2018). The drastic heat flow variation is suggested as evidence of the ancient mantle plume activity which is thought to trigger the Emeishan large igneous province today (e.g. Chung and Jahn, 1995; Xu et al., 2004; Zhang et al., 2006; Ali et al., 2010). We revisit the heat flow fluctuations in the basin from Early Paleozoic to date with an aim of examining whether the observations at present could be alternatively produced by slowly varying heat flow. If this is the case, then a short, rapid rise in the Mid to Late Permian heat flow might not have happened and thus the reconstruction of paleo-heat flow no longer supports the existence of ancient mantle plumes.

The geological dataset for Well Nvji in the central Sichuan Basin adopted for this study are displayed in fig. 5.8. The data include strata thickness from Yuan et al. (2013), stratigraphic column from Zhang et al. (1988) and estimates of eroded thickness and measurements of vitrinite reflectance for the well from Zhu et al. (2009). The present-day heat flow in the central Sichuan Basin is set at 62 $mW \cdot m^{-2}$ as Xu et al. (2011) suggested. A constant surface temperature of 15°C is assumed for the region. We estimate the decompacted depth of sedimentary layers through time using the general model of Sclater and Christie (1980). The burial paths (fig. 5.8a) indicate two major erosion/uplift events during the basin formation, one of which from Mid Devonian to Early Permian and the other from Late Cretaceous till present. In addition, three minor erosion/uplift events, respectively during Mid Permian, Mid Triassic and Late Triassic, are also identified. The present-day vitrinite reflectance ranges from 0.8% at 1000 m depth to 3.8% at 6000 m depth of the well (fig. 5.8b).

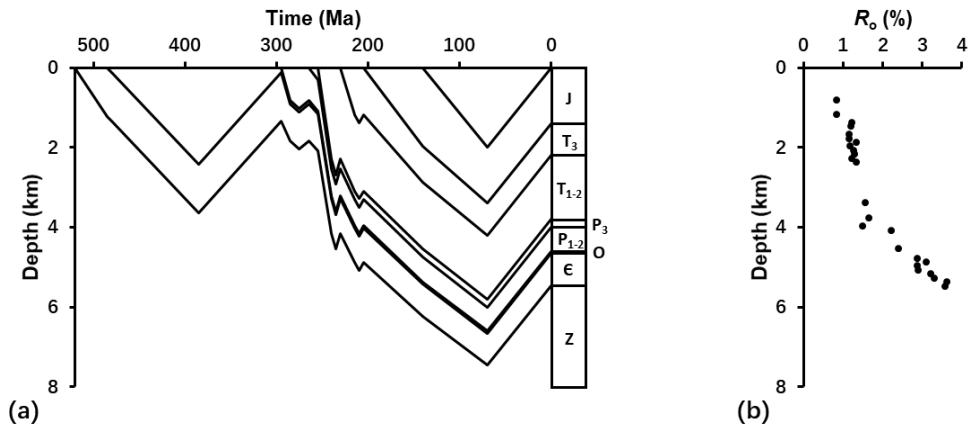

Figure 5.8 Geological dataset for the Well Nvji, central Sichuan Basin. (a) Burial history reconstructed from the well-log data and stratigraphic information. (b) Downhole data of the vitrinite reflectance.

With the influence of tectonic uplift and erosion on heat flow ignored, an apparent heat flow curve is first generated from the forward model by fitting the *in-situ* data. The apparent heat flow curve and the resulting model are illustrated in fig. 5.9, where it is shown that, the heat flow (fig. 5.9b) in the region remained ~50 $mW \cdot m^{-2}$ from Early Cambrian to Mid Permian and then rose sharply to ~82 $mW \cdot m^{-2}$ during Late Permian, tightly followed by a rapid drop until it reached ~68 $mW \cdot m^{-2}$ in Mid Triassic and slowly went down to date. As shown in fig. 5.9d, the associated vitrinite reflectance profile, predicted from the apparent heat flow curve, proves to be compatible with borehole measurements.

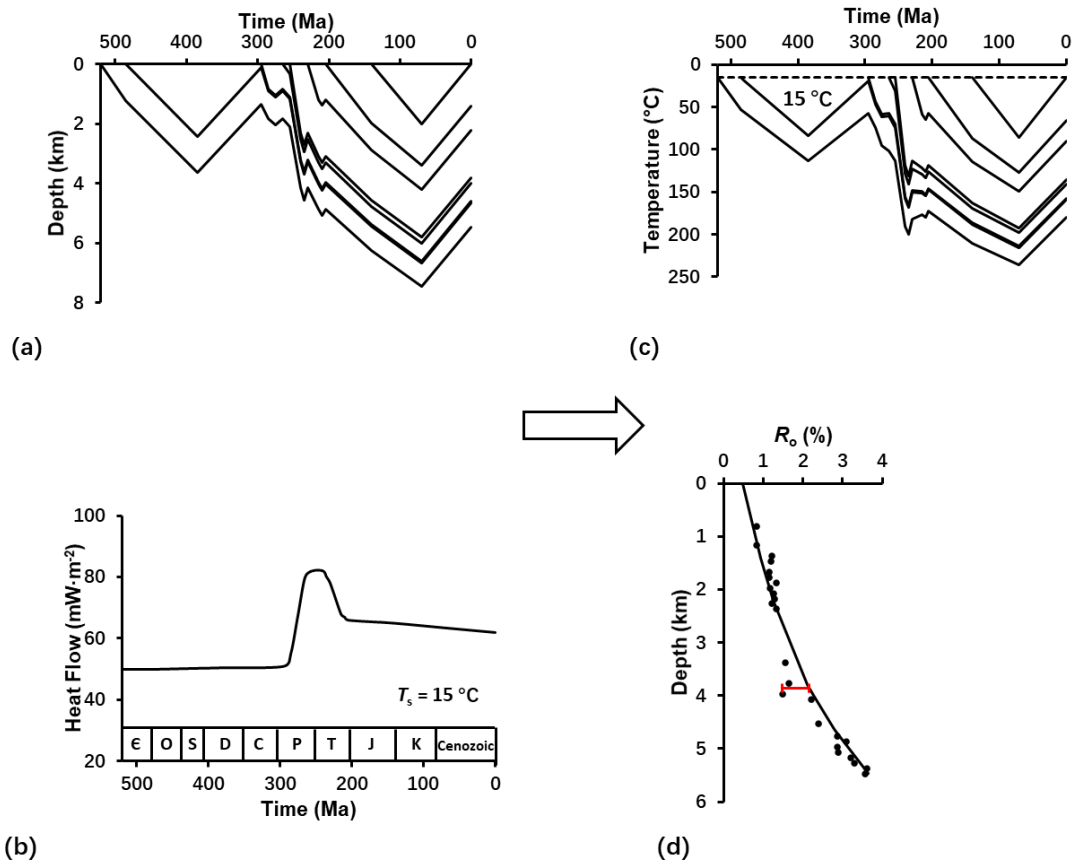

Figure 5.9 An initial solution to thermal history modelling for Well Nvji. (a) Burial history in the well. (b) A possible heat flow history inferred from borehole data and the forward model with variations caused by erosion/uplift excluded and surface temperature set at 15℃ over time. (c) Predicted subsurface temperature variations through time. (d) Predicted vitrinite reflectance profile (solid curve) and real measurements (markers). This is the globally best-fit prediction of downhole vitrinite reflectance though misfits are observed at *c*. 4000 m depth (with an error bar attached).

Next, we calculate additional solutions to the model. Application of the symmetry transformation approach discovers a series of alternative heat flow curves, all of which can reproduce the same vitrinite reflectance profiles. All these heat flow curves show very similar variations from Triassic until present but differ significantly in the earlier periods. The end member solutions with the smallest 1st and 2nd derivatives are

displayed in fig. 5.10 and fig. 5.11, respectively. The 1st derivative smoothest solution suggests the heat flow in Well Nvji remained at ~45 $mW \cdot m^{-2}$ through Cambrian before it gradually increased and peaked at 82 $mW \cdot m^{-2}$ by the end of Cretaceous. The abnormal heat flow lasted until Late Permian when it suddenly decreased. In contrast, the 2nd derivative smoothest solution suggests the heat flow initiated at ~25 $mW \cdot m^{-2}$ in Cambrian and increased continuously until it peaked at ~82 $mW \cdot m^{-2}$ in Mid Permian, followed by a sharp decrease. Therefore, it is almost certain that the region underwent unusually high temperature during Mid to Late-Permian. However, it remains unclear whether the temperature anomaly was resulting from a dramatic heat flow spike between Mid to Late Permian or a slow, continuous heat flow elevation that had begun much earlier. Note that the whole set of solutions can reproduce exactly the same present-day vitrinite reflectance profiles but different historical subsurface temperature.

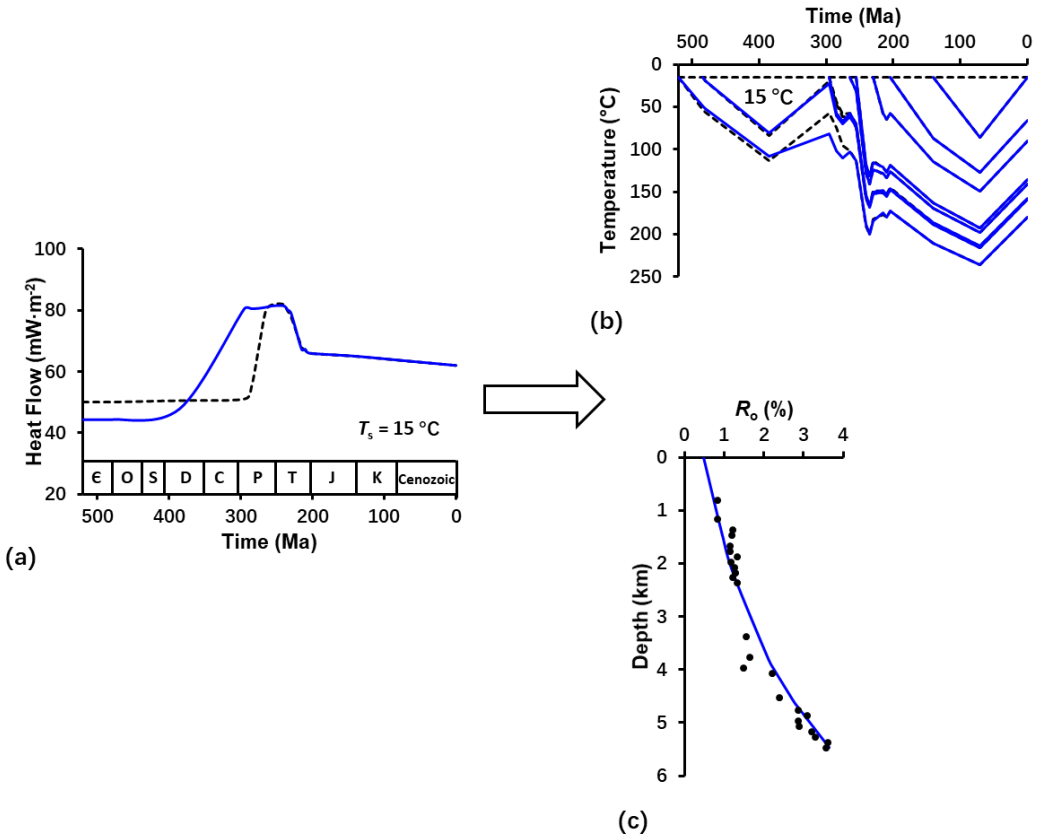

Figure 5.10 (a) An end-member solution (blue solid curve), with the smallest 1st derivative, derived from the initial solution (black dashed curve). (b)Subsurface temperature variations modelled from the end-member solution (blue solid curve) and the initial solution (black dashed curve). (c) Vitrinite reflectance profile modelled from the end-member solution is identical to the initial model. Other details as in fig. 5.9.

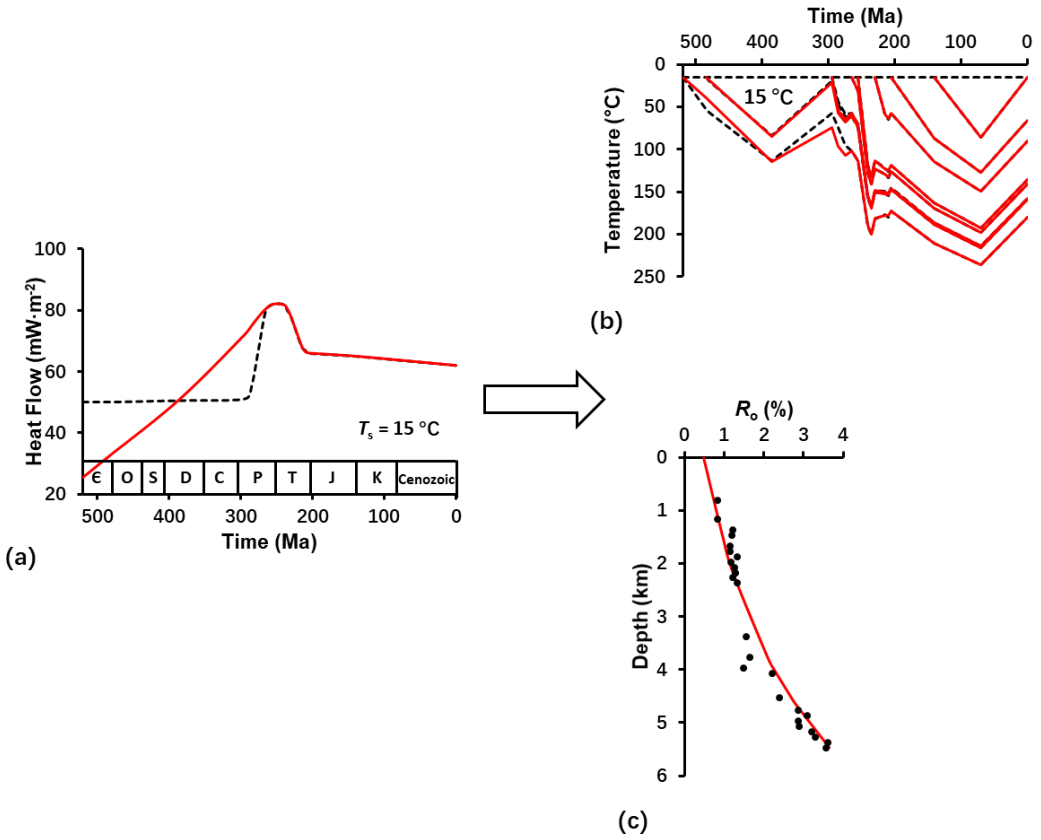

Figure 5.11 (a) An end-member solution (red solid curve), with the smallest 2nd derivative, derived from the initial solution (black dashed curve). (b)Subsurface temperature variations modelled from the end-member solution (red solid curve) and the initial solution (black dashed curve). (c) Vitrinite reflectance profile modelled from the end-member solution is identical to the initial model. Other details as in fig. 5.9.

5.6 Discussion

The model work presented here shows that application of vitrinite reflectance data to thermal history reconstruction should be cautiously reconsidered. Inverse problems in thermal history modelling are not only ill-conditioned as small errors in the observations produce large changes in the model prediction, but are hampered by non-uniqueness as more than one result is compatible with the observations. Using

quantitative basin modelling techniques, the observational errors are often dealt with sensitivity analysis (e.g. Cao and Lerche, 1990; Nielsen, 1996) and yet the problem of non-uniqueness is often been neglected. Though the non-uniqueness in geophysical inverse problems has been highlighted since Backus and Gilbert (1970), the majority of thermochronological studies are still in favour of particular interpretations.

However, as it is shown that, the use of vitrinite reflectance data is inadequate to deduce the paleohistory, since the identical thermal indicators could be reproduced by infinitely many solutions. Each of the solutions appears to be feasible and hence it is not possible to pick out the real solution even in a geological sense. It has been suggested that thermal maturity of a sample is primarily determined by the maximum temperature the sample experienced (Price, 1983) or the duration of the maximum temperature lasted (Hood et al., 1975), rather than individual events in the thermal history. As a result, the thermal history prior to the episode of maximum temperature is often poorly constrained. In fact, not a single type of paleothermometers offers complete record of the thermal history. Another example of these can be apatite fission-track analysis, which reveals the recent cooling stage but often fail to deduce history in the earlier periods (Green et al., 1989; Gallagher, 1995).

To avoid over-interpreting the data observed, the conventional inverse theory tends to use the smoothest solutions. However, two fundamental problems exist for this method. First, determining the smoothest solutions has remained challenging, as the calculation has typically relied on stochastic algorithms that depend on *a priori* constraints and are often trapped in local optima. Solutions given by such approaches

are apparently smooth but may still engage unnecessary complexities. Secondly, the smoothest solution should not be thought of as the real solution. As presented above, the smoothest solutions have notably less complexities compared to the initial solution generated using traditional approaches. Interpretation built upon the smoothest solutions may overlook some dramatic changes in the thermal history and thus are misleading.

Nevertheless, it is possible to give firm statements regarding the thermal history despite the non-uniqueness. In this study, the principle of symmetry proves to be a powerful tool for determining the past heat flow variations. An initial solution of the heat flow history can be easily generated from a forward model given simplifying assumptions. The changes in the model can be linearized by considering small enough changes to the parameters. The linear approximation reveals the correlation between multiple solutions and hence an existing solution can be directly transformed into additional solutions that do not rely on the unrealistic assumptions. Repetitive transformation allows end-member solutions to the model to be derived. By comparing the multiple solutions, we are able to discover what properties are in common to the ensemble of solutions.

In this work, we examined the subsurface temperature variations in the Sichuan Basin from Early Cambrian. With the burial history, lithologies and surface temperature fixed, infinitely many heat flow histories are found to account for the same vitrinite reflectance models. All heat flow histories discovered overlap each other from Triassic to present, but differ significantly in the early ages. However, every possible solution

indicates that the region suffered from particularly high heat flow (~82 $mW \cdot m^{-2}$) through Mid to Late Permian. This discovery agrees with previous studies which suggested the Permian heat flow in the Sichuan Basin ranged from 60 $mW \cdot m^{-2}$ in the north to over 100 $mW \cdot m^{-2}$ in the southwest (e.g. Lu et al., 2005; Zhu et al., 2010; He et al., 2011). Estimates of paleo-heat flow, together with the facies analysis of outcrops, were previously applied to studies of ancient mantle plumes (e.g. He et al., 2006; Li et al., 2017). However, the model work suggests that the temperature anomaly might be generated by slow, continuing heat flow variations, rather than a short-lived event. As a consequence, the influence of the mantle plumes on paleoclimate (e.g. the end-Guadalupian mass extinction event) might be much smaller than would be expected from a drastic heat flow spike within a few million years.

It is worth noting that the concepts of symmetry and the resulting inversion techniques can be extensively applicable in thermal history modelling. In this paper, we primarily investigated the paleo-heat flow variations. Other factors that affect the thermal histories, including the thickness of erosion, surface temperature and thermal conductivities were set to be constant employed from supplementary datasets. However, estimates of eroded thickness can vary up to a few hundred meters even in the same region. The temperature at seafloor or subaerial interface may fluctuate for tens of °C over million years. The measurements of thermal conductivities play a crucial role in estimating the subsurface geothermal gradients. Taking these complications into account can introduce extra non-uniqueness into the models. Moreover, instead of a steady-state equation as applied here, modern basin modelling

software frequently implements transient solutions, in particular for the areas where rapid sedimentation took place. Furthermore, a number of studies have suggested reaction kinetic models of vitrinite reflectance evolution as a replacement of TTI calculation (Burnham and Sweeney, 1989; Sweeney and Burnham, 1990; Nielsen and Dahl, 1991; Nielsen et al., 2017). However, a forward model can be extended to include these additional factors and the proposed inversion scheme still applies. If adapted in more sophisticated models, the inverse method can produce more robust information regarding thermal conditions.

5.7 Conclusions

Thermal history reconstruction suffers from the fundamental challenge of non-uniqueness. The inversion scheme, based on the implicit symmetries of numerical models, is effective in generating a representative ensemble of solutions that account for the vitrinite reflectance data observed at present. The rules of symmetry can enable an initial solution to be easily produced and additional solutions to be rapidly derived from the initial solution. Calculation of multiple solutions allows universal properties and end-member possibilities of the ensemble to be deduced. Application of the symmetry method can offer more complete solutions to thermal history modelling and hence more reliable reconstructions of paleo-history. Application of the symmetry method can also provide more predictive power for subsurface thermal structures and hence more accurate information of hydrocarbon generation.

6 An Inversion Approach for Analysing the Physical Properties of a Seismic Low-velocity Layer in the Upper Mantle

Jie Xiao[a, b, c, *], Saswata Hier-Majumder[b], Benoit Tauzin[d, e], Dave Waltham[b]

(a) State Key Laboratory of Organic Geochemistry, Guangzhou Institute of Geochemistry, Chinese Academy of Sciences, Guangzhou, 510640, China

(b) Department of Earth Sciences, Royal Holloway, University of London, Egham, TW20 0EX, United Kingdom

(c) University of Chinese Academy of Sciences, Beijing 100049, China

(d) Université de Lyon, UCBL, ENS Lyon, CNRS, Laboratoire de Géologie de Lyon, Terre, Planètes, Environnement, Villeurbanne, France

(e) Research School of Earth Sciences, Australian National University, Canberra, Australian Capital Territory 0200, Australia

* Corresponding author (Jie.Xiao.2016@live.rhul.ac.uk)

Author statement

This chapter is a reprint of the article as appears in: Xiao, J., Hier-Majumder S., Tauzin, B. & Waltham, D., 2020. An inversion approach for analysing the physical properties of a seismic low-velocity layer in the upper mantle. Physics of the Earth and Planetary Interiors, https://doi.org/10.1016/j.pepi.2020.106502. The thesis author was

the primary investigator and lead author of this work. His contributions to this work are summarized as follows:

(1) Conceptualization: formulation of the overarching research objectives and aims;

(2) Methodology: development of the methodology; creation of the inverse model;

(3) Software: designing the computer programs;

(4) Investigation: application of the proposed modelling techniques to seismic shear-wave velocity data from western US; inferring thermal and compositional properties of the 350-km depth low-velocity layer beneath the region;

(5) Writing: creation of a complete first draft.

6.1 Abstract

In this article, we propose a new inversion scheme to calculate the melt volume fractions from observed seismic anomalies in a low-velocity layer (LVL) located atop the mantle transition zone. Our method identifies the trade-offs in the seismic signature caused by temperature, solid composition, melt volume fraction, and dihedral angle at the solid-melt interface. Using the information derived from the amplitude of P-to-S conversions beneath the western US, we show that the multiple permissible solutions for melt volume fractions are correlated to each other. Any possible solution can be directly transformed into alternative solutions whilst leaving the model output unchanged. Hence, the additional solutions can be rapidly derived given an initial solution. The calculation of multiple solutions reveals the universal properties of the whole range of solutions. A regional-averaged melt volume fraction of at least 0.5% occurs in every solution, even though a unique interpretation does not exist.

Keywords: Shear wave, low-velocity layer, partial melting, inverse problem, non-uniqueness

6.2 Introduction

The mantle transition zone (MTZ) – marked by a drastic change in the physical properties of the silicate mineral phases – plays a crucial role in the convective flow of the mantle. The sharp changes in density and volatile storage capacity across the

boundaries of the MTZ can act as impediments to mass transfer and as sites of partial melting (Bercovici and Karato, 2003; Morra et al., 2010). Seismic observations also provide evidence of partial melting atop the MTZ; a low-velocity layer (LVL) located at ~350 km depth has been identified just above the mantle transition zone in numerous regions around the world, with lateral thickness from tens to several hundred kilometres (e.g. Song et al., 2004; Gao et al., 2006; Courtier and Revenaugh, 2007; Schaeffer and Bostock, 2010; Huckfeldt et al., 2013). The 2 – 3% reductions in shear wave velocities demarcate a sharp interface between the LVL and the overlying mantle, indicating the likely presence of a chemical anomaly and, in particular, partial melting. However, quantifying the fraction of melt has remained challenging because environmental and chemical parameters, such as the mantle temperature, bulk solid composition and melt geometry, are not clearly understood.

The LVL has frequently been interpreted as a small fraction of melt triggered by volatile elements released from subduction zones (Revenaugh and Sipkin, 1994; Sun et al., 2020) or mantle plumes (Vinnik and Farra, 2007). Since melts, characterized by zero shear modulus, disproportionately reduce shear wave velocities, seismic anomalies with low velocities are often qualitatively attributed to melting. Indirect evidence of mass transfer between subducting slabs and surrounding mantle are obtained from 'superdeep diamonds' which bear geochemical signature of oxygen and carbon isotopic ratios that can be generated by mixing between mantle and subducting slabs at these depths.

The residual anomaly, defined as the difference between the observed shear velocity and the reference velocity, can be attributed to the presence of melting and used as a basis for calculating the volume fraction of melt in the LVL. Hence, calculation of the melt fraction requires accurate estimation of the reference seismic velocities, i.e. velocities in the absence of melting for given temperature and solid composition. However, interpreting the origin of the seismic velocity anomalies in the LVL is complicated by the competing influence of several additional factors. An increase in temperature typically leads to seismic velocity reductions even without melting whilst the influence of bulk mantle composition on seismic velocities also varies with depth (Xu et al., 2008). The multiple factors also likely affect each other. Furthermore, melting may leave a strong impact on the bulk solid composition, in particular the amount of basalt.

Non-uniqueness in LVL interpretations also arises from the fact that, in a partially molten layer, the seismic velocity reductions depend on both the degree of melting and the microstructure of the melt-bearing aggregates (Mavko, 1980; von Bargen and Waff, 1986; Takei, 1998, 2002). The dihedral angle (also known as wetting angle) at the solid-melt interface, controls the geometry of the load-bearing framework of partially molten rocks (Hier-Majumder and Abbott, 2010), trading off with inferred melt volume fraction. Chemical composition is also found to play a moderate role in reducing the seismic speeds (Wimert and Hier-Majumder, 2012; Hier-Majumder et al., 2014), and may alter the dihedral angle (Yoshino et al., 2005). The numerical experiment of Hier-

Majumder et al. (2014) indicated the difficulties in distinguishing different types of melt from the seismic observations as the fraction of melt is very small.

A number of previous studies mitigated the issue of competing influences by carrying out computationally expensive brute-force search to create lookup tables for inferred melt volume fractions corresponding to different controlling factors (e.g. Hier-Majumder and Courtier, 2011; Hier-Majumder et al., 2014; Hier-Majumder and Tauzin, 2017). While a brute-force search can produce a particular scenario of inversion, application of the approach is unable to ascertain if alternative solutions exist in the parameter space. Although, in principle, the entire range of solutions could be discovered through repetitive use of the algorithm given different combinations of the parameters, it fails to rigorously tackle the nature of variations in the inferred melt volume fractions caused by changes in the other factors. Therefore, a new inversion scheme is required to interpret these geophysical observations and to address the theoretical drawback of previous studies.

Here we present a mathematical formulation that uses the implicit symmetry of a petrologic model to understand the non-uniqueness in the melt fraction inference. The principle of symmetry has been successfully applied in a sedimentological problem (Xiao and Waltham, 2019), showing that multiple solutions can be closely linked even when an inverse problem is non-linear. When symmetries exist, an existing solution can be directly transformed into another solution that leaves modelling products unchanged, in the same way that rotating a square by 90° produces an identical geometry. In this way, the search for all possible solutions can begin with an initial

solution generated through standard inversion techniques. Application of the symmetry method then allows additional solutions to be calculated from the initial solution.

This paper uses the resultant inversion scheme to revisit the 350-km LVL beneath the western US. A seismically anomalous layer in this region has been reported underneath the Oregon-Washington border (e.g. Song et al., 2004), Yellowstone (e.g. Fee and Dueker, 2004; Jasbinsek and Dueker, 2007), the Northern Rocky Mountains (e.g. Jasbinsek and Dueker, 2007; Zhang et al., 2018), the Colorado Plateau/Rio Grande Rift (e.g. Jasbinsek et al., 2010), and California (e.g. Vinnik et al., 2010). Once the complete set of solutions has been derived, the lowest possible fractions of melt within the LVL can be easily determined. As such, we can generate a robust, lower-bound estimate of amount of partial melting in the LVL that does not rely on assumed values of the other parameters. The calculation also offers more reliable information about the solid mantle, such as the plausible ranges of temperature and basalt fraction. For example, the estimates of melt content and associated parameters can be used to infer the budget of volatile elements in the mantle and the excess temperature of the mantle plumes beneath the region.

6.3 The 350-km LVL Beneath the Western US

6.3.1 Seismic observations

The seismic data used here are teleseismic *P*-to-*S* conversions recorded on receiver functions from the Transportable Array of seismic stations in the western US

(fig. 6.1). Shear wave velocity contrasts at a depth of around 350 km have been derived for 583 sites over a 0.5° x 0.5° grid in latitude and longitude. The seismically anomalous layer covers an area of 1.8×10^6 km^2, with lateral thickness from 25 to 90 km (Hier-Majumder and Tauzin, 2017).

6.3.2 Calculating shear wave velocities

To invert the shear wave speeds in the LVL from the seismic observations, we follow the computational approach outlined in Hier-Majumder et al. (2014). We use the results of mode-conversion amplitudes at the top and the base of the LVL to estimate the velocity variations. To eliminate systematic variations in the amplitude of converted arrivals caused by differences in seismic wave incidence, we normalize the observed seismic amplitudes prior to computation. The normalized amplitude is calculated from the ratio of amplitudes of arrivals converted at the top of the LVL over arrivals converted at the olivine-wadsleyite mineralogical phase change at 410 km depth:

$$R_{\mathrm{norm}} = \frac{A_{\mathrm{LVL}}}{A_{410}} < 0 \qquad (6.1)$$

, where A_{LVL} is the frequency-averaged amplitude at the top of the LVL recorded at each cell on the grid, and A_{410} is the frequency-averaged amplitude at the 410-km discontinuity in the same cell. Using R_{norm}, we then calculate the shear wave velocity (V_S^{obs}) at each location from the normalized contrast between the shear velocity immediately above the 350-km LVL (V_S^{350}) and the velocity immediately below the 410-km discontinuity (V_S^{410}):

$$V_S^{\text{obs}} = V_S^{350}\left(1 + R_{\text{norm}}\frac{V_S^{410} - V_S^{350}}{V_S^{350}}\right) \tag{6.2}$$

We calculate V_S^{350} and V_S^{410} as the shear wave velocities at the depths of 350 km and 410 km, respectively, from the Preliminary Reference Earth Model (PREM, Dziewonski and Anderson, 1981). Compared to the global predictions from the PREM (~4735 m/s at 350 km depth), the estimated shear-velocities yield an average reduction of 1.6%.

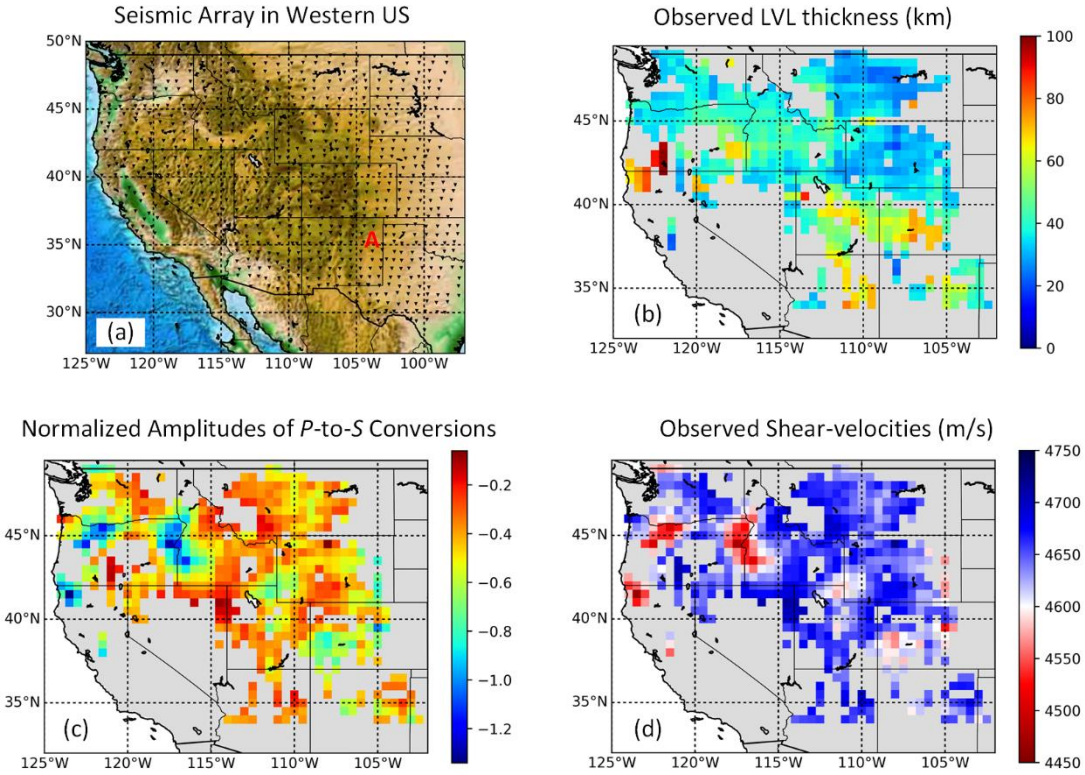

Figure 6.1 Seismic observations of the 350-km LVL below the western US. (a) A map of the dense seismic array of 820 sites (black triangles, from Tauzin et al., 2013). The seismic cell (106.5°W, 38°N) discussed later in this paper is labelled 'A'. (b) The thickness of the LVL beneath 583 sites

(from Hier-Majumder and Tauzin, 2017). (c) Normalized amplitudes of *P*-to-*S* converted arrivals. (d) Shear wave velocities in the LVL estimated from the seismic data.

6.3.3 Evaluating temperature variations

We then evaluate the thermal variations in the LVL using the method outlined in Tauzin and Ricard (2014). In this method, the temperature variations (ΔT) are related to the observed thickness of the MTZ (δh) and the Clapeyron slopes (i.e. the change in pressure of phase transition with respect to the change in temperature at which the phase transition occurs) for the olivine-wadsleyite phase transitions at 410 km (γ_{410}) and 660 km (γ_{660}). We employ the data of spatial variations in MTZ thickness beneath the western half of the US from Tauzin et al. (2013). We also set the reference MTZ thickness at 250 km calculated by Tauzin and Ricard (2014) using the IASP91 spherical model of Kennett and Engdahl (1991). We follow the empirical scheme of Tauzin and Ricard (2014) and set γ_{410} = 3.0 MPa/K and γ_{660} = 0.64 γ_{410} – 1.17. The uncertainties associated with the supplementary parameters will be discussed in later sections. Using these methods, we calculate the temperature variations in the LVL from the MTZ thickness beneath the seismic array (see fig. 6.2).

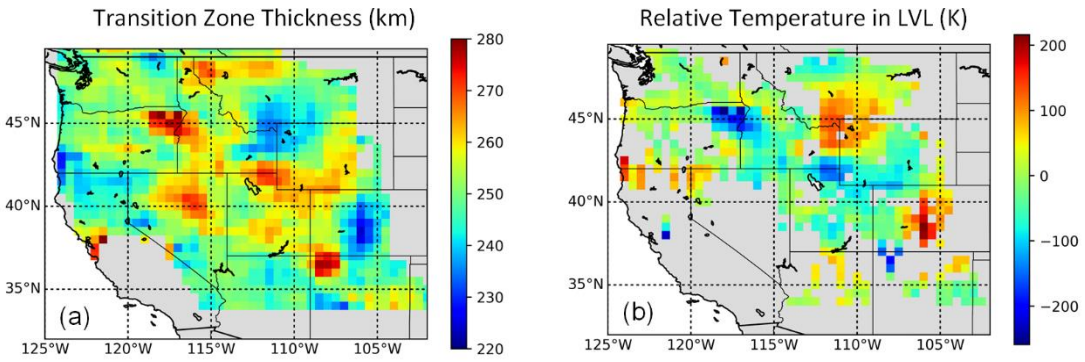

Figure 6.2 Thickness of MTZ (a) and temperature variations in the LVL (b) estimated from the MTZ thickness (after Tauzin and Ricard, 2014).

6.4 Forward Modelling

The forward model of shear-velocities presented here incorporates four primary controls, including the mantle potential temperature, bulk solid composition, melt volume fraction and dihedral angle at the solid-melt interface. The simulation of shear wave speeds in the LVL consists of two independent steps. Firstly, we estimate the reference velocities from the properties of the solid mantle. Secondly, we calculate the changes in velocities as waves travelling through a melt-bearing aggregate using a micromechanical model that involves both the fraction and geometry of the melt.

6.4.1 Estimating reference velocities

We estimate the reference shear wave speeds in the solid mantle accounting for the thermal and compositional properties of the mineral. The mantle temperature below each site can be expressed as

$$T = T_0 + \frac{\mathrm{d}T}{\mathrm{d}z} z_{\mathrm{LVL}} + \Delta T \tag{6.3}$$

, where T_0 is the potential temperature of the reference mantle, $\mathrm{d}T/\mathrm{d}z$ is the adiabatic temperature gradient which is suggested as 0.4 – 0.5 K/km in the upper mantle (Katsura et al., 2010), z_{LVL} is the depth of LVL and ΔT is the temperature variation at a given location. We set z_{LVL} at the average depth of 352 km as observed from the seismic profiles. To quantify the mantle composition, we follow the definition from Xu et al. (2008) which parameterizes the mantle as a mechanical mixture of mid-ocean ridge basalt and harzburgite. In this formulation, the composition of the solid mantle can be expressed as the fraction of basaltic component. We can then formulate the reference shear wave velocities as $V_{\mathrm{S}}^{\mathrm{ref}} = V_{\mathrm{S}}^{\mathrm{ref}}(T_0, C)$, where T_0 and C are the potential temperature and basalt fraction of the mantle, respectively.

Reference shear wave speeds applied here are derived from the mineral physics database of Xu et al. (2008), in which seismic velocities are tabulated with associated combinations of potential temperatures and basalt fractions. In the database, potential temperatures range from 1000 to 2000 K with increments of 100 K whereas basalt fractions range from 0 to 100% with increments of 5%. While we can select a given value of C for the calculation, the temperature at any point on the seismic grid is determined from the MTZ thickness as discussed above. As a result, we interpolate the value of seismic velocity for the temperature evaluated at each location using a second-order polynomial interpolation between two tabulated values. Using this interpolation, we are able to calculate the value of reference shear wave speed at each point for a given bulk basalt volume fraction and a given reference potential temperature. Figure 6.3 presents the predictions of regional-average shear wave

speeds for a range of potential temperatures and basalt fractions at a constant pressure of 11.7 GPa. The Thermal and compositional effects can trade off each other and thus different combinations of the two variables may lead to the same velocities.

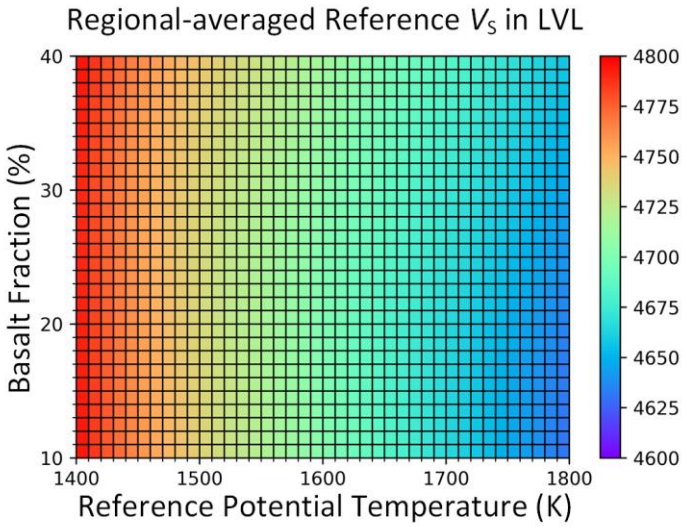

Figure 6.3 Predicted regional-averaged reference shear wave velocities at 11.7 GPa in response to different combinations of reference potential temperature and basalt fraction in the LVL beneath the western US.

6.4.2 Partial melting and velocity reductions

To simulate the influence of partial melting on seismic velocities, we employ the modelling scheme of Takei (2002), where the shear wave speed variation ξ is governed by the effective elastic moduli of the aggregate:

$$\xi = \sqrt{\frac{N/\mu}{\bar{\rho}/\rho_s}} \tag{6.4}$$

, where N is the effective shear modulus of the intergranular skeletal framework that indicates the strength of contact between the neighbouring grains, μ is the shear

modulus of the solid devoid of a melt phase, ρ_s is the density of the solid bulk and $\bar{\rho}$ is the volume-averaged density of the entire aggregate which is calculated as:

$$\bar{\rho} = \rho_{\mathrm{m}}\varphi + \rho_{\mathrm{s}}(1-\varphi) \tag{6.5}$$

, where ρ_m is the density of the melt; φ is the volume fraction of melt within the aggregate.

In eq. 6.4, the elastic modulus N is determined by both the melt volume fraction φ and the contiguity (ψ, i.e. the area fraction of the intergranular contact) of the melt:

$$N = \mu(1-\varphi)[1-(1-\psi)^n] \tag{6.6}$$

The contiguity ψ depends on the melt volume fraction φ and the dihedral angle θ between the solid grains and the melt; and n is an exponent also depending on ψ (Takei, 2002). The simulations of contiguity applied here are based on the micro-structural model of von Bargen and Waff (1986) which formulates the contiguity ψ as the proportion that the contact area of grains occupy among the total contact area in a partial molten aggregate:

$$\psi = \frac{2A_{\mathrm{gg}}}{2A_{\mathrm{gg}} + A_{\mathrm{gm}}} \tag{6.7}$$

, where A_{gg} and A_{gm} are the grain-grain contact area and grain-melt contact area per unit volume, respectively. The values of A_{gg} and A_{gm} are calculated from the given melt volume fraction and dihedral angle using polynomial functions:

$$\begin{cases} A_{\mathrm{gg}} = \pi - b_{\mathrm{gg}}\mathrm{power}(\varphi, p_{\mathrm{gg}}) \\ A_{\mathrm{gm}} = b_{\mathrm{gm}}\mathrm{power}(\varphi, p_{\mathrm{gm}}) \end{cases} \tag{6.8}$$

The required constants b_{gg}, b_{gm}, p_{gg} and p_{gm} are approximated from quadratic polynomials of the dihedral angle (in degree), of which the values are outlined in von Bargen and Waff (1986). Wimert and Hier-Majumder (2012) demonstrated this approximation of contiguities can produce satisfactory fits with experimental measurements from partially molten aggregates with melt volume fractions below 5%.

Combining equations 6.3 – 6.7 enables the contiguity to be expressed as a function of the melt volume fraction φ and dihedral angle θ, i.e. $\psi = \psi(\varphi, \theta)$. Moreover, shear wave speed anomalies ξ caused by partial melting can be formulated as a function with respect to melt volume fraction and dihedral angle:

$$\xi(\varphi, \theta) = \sqrt{\frac{(1-\varphi)\left[1-\left(1-\psi(\varphi,\theta)\right)^{n}\right]}{1-\varphi(1-\rho_{\mathrm{m}}/\rho_{\mathrm{s}})}} \tag{6.9}$$

We estimate the densities of solid bulk ρ_{s} and melt ρ_{m} using the third-order Birch-Murnaghan equation of state (EOS), as Ghosh et al. (2007) suggested for carbonated peridotite melt. We implement the mathematic approximations using MuMaP_fwd (Hier-Majumder, 2017), a Python computational toolkit for microscale geodynamic study. The modelled shear wave velocity reductions in response to a variety of melt volume fractions and dihedral angles are illustrated in fig. 6.4. The curves show that the velocity in the partially molten aggregates decreases rapidly as the fraction of melt increases. The curves also show that, for the same melt volume fraction, a smaller dihedral angle results in greater reductions in the shear wave speed. Hence, different combinations of dihedral angles and melt volume fractions produce the same shear-velocity reductions.

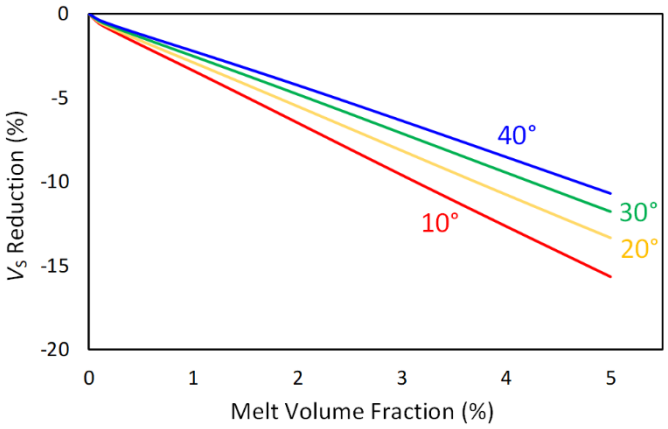

Figure 6.4 Predicted shear wave velocity reductions for different melt volume fractions and dihedral angles. Each curve shows the velocity reductions caused by changes in melt volume fraction at the indicated dihedral angle.

6.5 Model Inversion

The forward modelling approach described in the preceding section predicts the shear wave velocity reductions in response to associated parameters. Alternatively, it is possible to calculate the velocity reductions as a ratio of the observed velocity over the reference velocities:

$$\xi = \frac{V_S^{\mathrm{obs}}}{V_S^{\mathrm{ref}}(T_0, C)} \tag{6.10}$$

When embedded with an inversion scheme, the numerical model can be used to deduce the controls on seismic velocities. The inversion procedure can begin with an initial solution that is built upon petrologic and seismological constraints. We then investigate how to exploit and utilize the symmetry of the model, which can allow us to alter the initial solution directly into another solution whilst giving the same

observations. In this way, the additional solutions to the inverse problem can be rapidly derived by repeated use of the transformation.

6.5.1 An initial solution based on a priori knowledge

To incorporate the forward model and the observed data in a single framework, we firstly combine eq. 6.9 and 6.10:

$$\sqrt{\frac{(1-\varphi)\cdot\left[1-\left(1-\psi(\varphi,\theta)\right)^{n}\right]}{1-\varphi(1-\rho_{\mathrm{m}}/\rho_{\mathrm{s}})}}=\frac{V_{\mathrm{S}}^{\mathrm{obs}}}{V_{\mathrm{S}}^{\mathrm{ref}}(T_0,C)} \tag{6.11}$$

, which gives four unknowns (i.e. T_0, C, θ and φ) in one equation. To solve for melt volume fraction φ from eq. 6.11, the reference potential temperature T_0, basalt fraction C and dihedral angle θ need to be specified. We initially assume the reference potential temperature to be 1500 K in the region. We set the basalt fraction at 18%, as suggested in Xu et al. (2008) for common peridotite. The dihedral angle at the grain-melt interface varies with the chemical composition of the melt. For example, Minarik and Watson (1995) proposed dihedral angles varying from 25° to 30° at the interface between carbonate melt and molten aggregates; Mei et al. (2002) suggested a dihedral angle of 28° for molten aggregates with hydrous basalt melt. Here we initially assume a dihedral angle of θ = 25°. Given these *a priori* assumptions, T_0, C and θ are specified, and hence the melt volume fraction can be solved from eq. 6.11.

We then calculate the corresponding melt volume fraction φ using a modified Newton-Raphson root-search algorithm (Press et al., 2007, chap. 9.1), as previously

demonstrated by Hier-Majumder and Tauzin (2017). The algorithm begins with a bracket for the melt volume fraction between 1×10^{-4}% and 10% and iterates the searching process until a convergence of 10^{-4}% is achieved in the inferred fraction. Figure 6.5 shows the initial solution derived from the inversion using the seismic observations and the constraints on T_0, C and θ. The melt fractions in the region vary spatially and yields an average of 0.72%. As a check, synthetic velocities reproduced from the forward model (fig. 6.5c) are a good match to the original observations (fig. 6.1d).

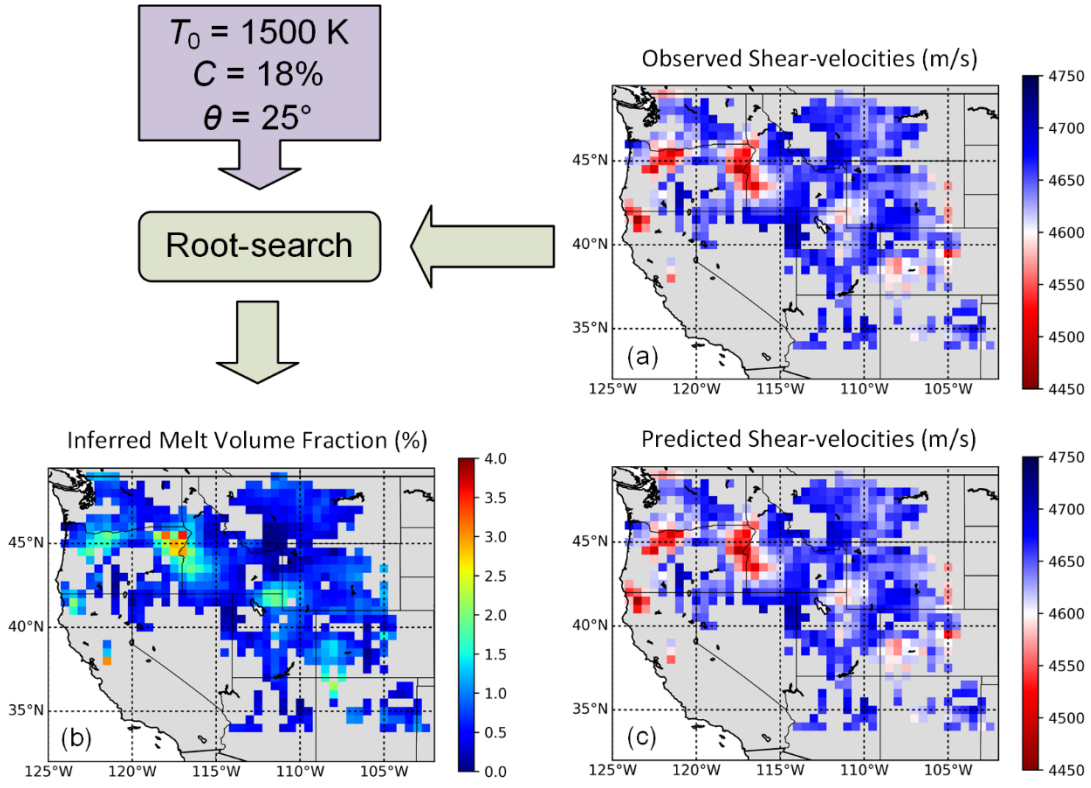

Figure 6.5 An initial solution to the inverse problem of 350-km LVL. The observed shear wave velocities (a) and reference values of $\boldsymbol{T_0}$, $\boldsymbol{C}$ and $\boldsymbol{\theta}$ are used to provide constraints on the inversion. A particular solution for the melt vol. % within the LVL (b) is then generated using the root-search approach. The regional-averaged fraction is calculated as 0.72% for $\boldsymbol{T_0}$ = 1500 K, $\boldsymbol{C}$ =

18% and $\boldsymbol{\theta}$ = 25°. Using the inferred melt vol. % and the reference values, shear wave velocities (c) can be reproduced from the forward model.

6.5.2 Symmetric transformation

The above calculation generates a single solution to the inverse problem. Since the inverse problem is non-unique with respect to the input parameters T_0, C and θ, there are, in principle, an infinite number of alternative solutions that can reproduce identical seismic observations. Here we develop a quantitative approach to prove the non-uniqueness and, more crucially, the transformation from an existing solution to an alternative solution. The symmetry of the numerical model is found by modifying the input parameters to obtain an unchanged output model. To start with, we formulate the forward model of shear wave speed as:

$$\boldsymbol{V}_{\mathrm{S}} = F(T_0, C, \theta, \boldsymbol{\varphi}) \tag{6.12}$$

, where $\boldsymbol{V}_{\mathrm{S}}$ is the shear wave speeds in the LVL beneath the seismic sites; F denotes a general, non-linear function (in this work, F is the forward model from the code MuMaP_fwd) and $\boldsymbol{\varphi}$ is a vector of melt volume fractions in the LVL. Note that 583 seismic sites are analysed in this study, and hence the vector lengths are 583 for both $\boldsymbol{V}_{\mathrm{S}}$ and $\boldsymbol{\varphi}$. We then generate three perturbations δT_0, δC and $\delta\theta$. These small changes in the model inputs give rise to residuals in the modelled velocities, i.e. $\Delta\boldsymbol{V}_{\mathrm{S}}$. This can be written as:

$$\Delta\boldsymbol{V}_{\mathrm{S}} = F(T_0 + \delta T_0, C + \delta C, \theta + \delta\theta, \boldsymbol{\varphi}) - F(T_0, C, \theta, \boldsymbol{\varphi}) \tag{6.13}$$

, which may be approximated in a linear form using the first-order Taylor's series:

$$\frac{\partial F}{\partial T_0}\delta T_0 + \frac{\partial F}{\partial C}\delta C + \frac{\partial F}{\partial \theta}\delta\theta = \Delta \boldsymbol{V}_{\mathrm{S}} \tag{6.14}$$

, where $\partial F/\partial T_0$, $\partial F/\partial C$ and $\partial F/\partial \theta$ are finite derivatives of the function F with respect to T_0, C and θ. We then calculate changes required in the melt volume fractions (i.e. $\delta\boldsymbol{\varphi}$) to compensate the changes in velocities resulting from the perturbations. This can be expressed as:

$$F(T_0 + \delta T_0, C + \delta C, \theta + \delta\theta, \boldsymbol{\varphi} + \delta\boldsymbol{\varphi}) = F(T_0, C, \theta, \boldsymbol{\varphi}) \tag{6.15}$$

Approximation based on the Taylor's series gives:

$$\frac{\partial F}{\partial T_0}\delta T_0 + \frac{\partial F}{\partial C}\delta C + \frac{\partial F}{\partial \theta}\delta\theta + \frac{\partial F}{\partial \boldsymbol{\varphi}}\delta\boldsymbol{\varphi} = 0 \tag{6.16}$$

, where $\partial F/\partial\boldsymbol{\varphi}$ is the finite derivative of the function F with respect to $\boldsymbol{\varphi}$. We then solve $\delta\boldsymbol{\varphi}$ by combining eq. 6.14 and 6.16:

$$\delta\boldsymbol{\varphi} = -\frac{\Delta \boldsymbol{V}_{\mathbf{S}}}{\partial F/\partial\boldsymbol{\varphi}} \tag{6.17}$$

In this equation, $\partial F/\partial\boldsymbol{\varphi}$ can be calculated from the forward model. The new solution can then be used as a basis for another transformation. Iterative transformation can therefore derive all the additional solutions to the inverse problem.

6.5.3 Calculating multiple solutions

Using the forward model and symmetric transformation, we then examine the entire parameter space and calculate alternative solutions. The parameter space can be considered as a 3-D space with basis vectors potential temperature (T_0), basalt fraction (C) and dihedral angle (θ). We define the ranges of the parameters as 1400 to

1800 K in potential temperature, 10 to 40% in basalt fraction and 10° to 40° in dihedral angle. We also set the increments at 10 K in potential temperature, 1% in basalt fraction and 1° in dihedral angle, sampling the parameter space in small intervals. Each position in the parameter space can be described using the coordinates in the 3-D space. If a solution exists in position (T_0, C, θ), then the corresponding melt volume fraction vector can be written as $\boldsymbol{\varphi}(T_0, C, \theta)$. Once a solution is found, the solutions in neighbouring positions can also be determined. Because the transformation can be applied both forward and backward, six neighbouring solutions should be examined, including $\boldsymbol{\varphi}(T_0 + \delta T_0, C, \theta)$, $\boldsymbol{\varphi}(T_0 - \delta T_0, C, \theta)$, $\boldsymbol{\varphi}(T_0, C + \delta C, \theta)$, $\boldsymbol{\varphi}(T_0, C - \delta C, \theta)$, $\boldsymbol{\varphi}(T_0, C, \theta + \delta\theta)$ and $\boldsymbol{\varphi}(T_0, C, \theta - \delta\theta)$. We calculate the additional solutions through the following procedure:

(1) Create an empty list. Add the coordinate of the initial solution into the list.

(2) For each solution in the list, calculate the solutions in the neighbouring positions that are inside of the parameter space but not existing in the list.

(3) Add the solutions found in step (2) into the list.

(4) Return to step (2) and repeat the workflow until no new solution can be added into the list.

Note that this is different from a brute-force search which involves a root-searching approach for calculating the melt volume fraction beneath every location given different combinations of T_0, C and θ. In contrast, the symmetric transformation is straightforward as it can simultaneously derive the melt volume fraction beneath the whole area. Since this method works directly on the behaviour of the solution with

respect to perturbations, it also allows us to predict regions where melting does not exist and to predict the solution containing the lowest possible average melt fractions, which was intractable with the method described by Hier-Majumder et al. (2014).

6.5.4 Complete solutions to the inverse problem

Using the above computational procedure, we derive all the solutions in the parameter space. All the possible solutions can reproduce the same synthetic shear wave velocities from the forward model. Significant spatial variations in the inverted melt volume are found in every solution. Because the melt volume fraction should always be non-negative, the calculated vectors of $\boldsymbol{\varphi}$ where one or more negative values exist should be excluded. Given this requirement, limits can be placed to bound the symmetric transformation, i.e. not every combination of potential temperatures, basalt fractions and dihedral angles in the parameter space requires the presence of melting to explain the seismic anomaly. Example of the variations in calculated melt volume fractions and the transformation limits in the multiple controlling factors are demonstrated in fig. 6.6.

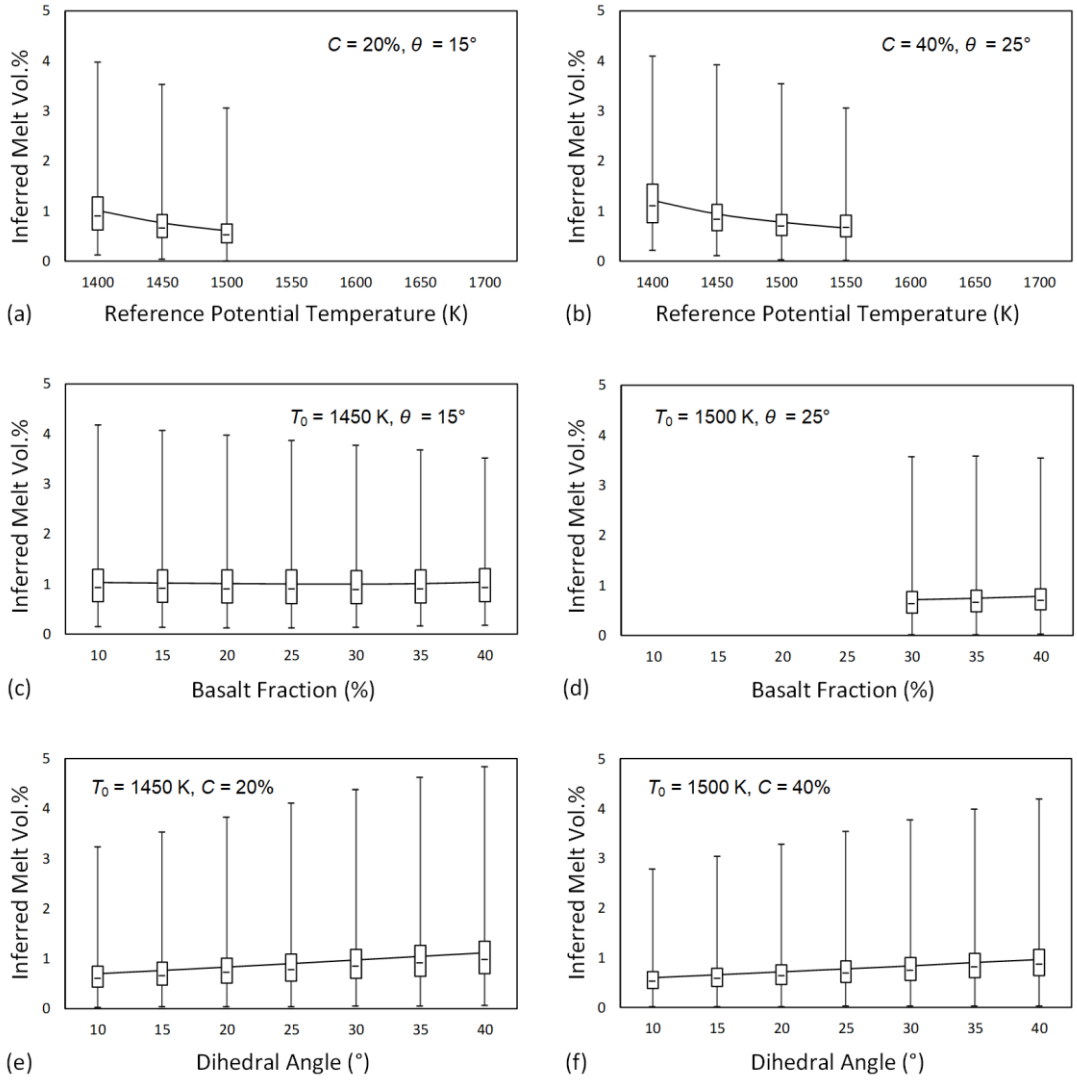

Figure 6.6 Estimated melt volume fractions beneath all locations with median indicated by the horizontal line within each box, upper/lower quartiles indicated by the upper/lower edges of the box and maximum/minimum indicated by whiskers of the boxes. (a) & (b) Inferred melt vol.% as a function of reference potential temperature with fixed basalt fraction and dihedral angles. (c) & (d) Inferred melt vol.% as a function of basalt fractions with fixed reference potential temperature and dihedral angle. (e) & (f) Inferred melt vol.% as a function of dihedral angle with fixed reference potential temperature and basalt fractions. Note that no solution can be found given $\boldsymbol{T_0}$ ≥ 1500 in (a), $\boldsymbol{T_0}$ ≥ 1550 K in (b) and $\boldsymbol{C}$ ≤ 30% in (d).

The model output illustrated in fig. 6.7 is an end-member solution showing that the lowest possible averaged melt volume fraction is 0.51%, associated with T_0 = 1550 K, C = 40% and θ = 10°. In this solution, melting is not predicted beneath some regions, for instance at the triple border between Idaho, Montana and Wyoming. Considering the sharp boundary atop the LVL, this may just be an artefact because the variations in solid bulk are unlikely to produce rapid velocity reductions. However, this solution is still meaningful since it places a lower-bound below the regional-averaged melt volume fraction within the observed LVL. In contrast, the highest possible averaged melt volume fraction that exists in the parameter space yields 1.47%, associated with T_0 = 1400 K, basalt fraction C = 10% and dihedral angel θ = 10°, as shown in fig. 6.8. Examples of the trade-offs between the estimated melt volume fraction below a given location and the multiple controls are displayed in fig. 6.9 by cross-plotting the estimates and the corresponding controlling factors. Whilst the forward model used here is non-linear, application of the proposed method has indicated the trajectories that link together the multiple solutions in the parameter space.

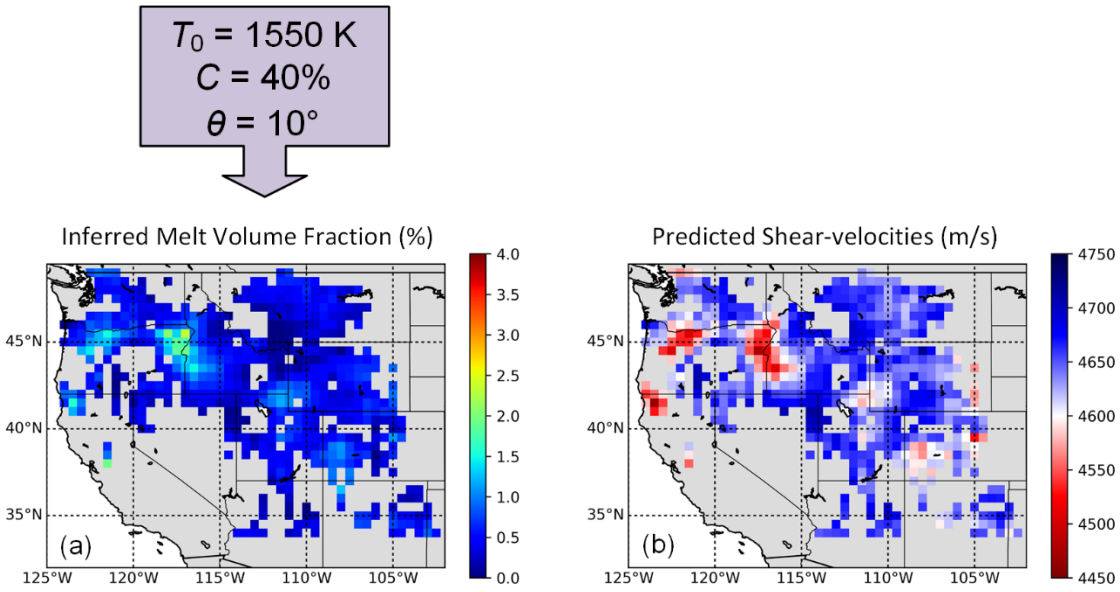

Figure 6.7 An end-member solution with the minimum melt vol. % within the LVL beneath the western US. The regional averaged melt vol. % is 0.51% given $\boldsymbol{T_0}$ = 1550 K, $\boldsymbol{C}$ = 40% and $\boldsymbol{\theta}$ = 10°. Note that this solution is directly derived from the initial solution, rather than from a brute-force search.

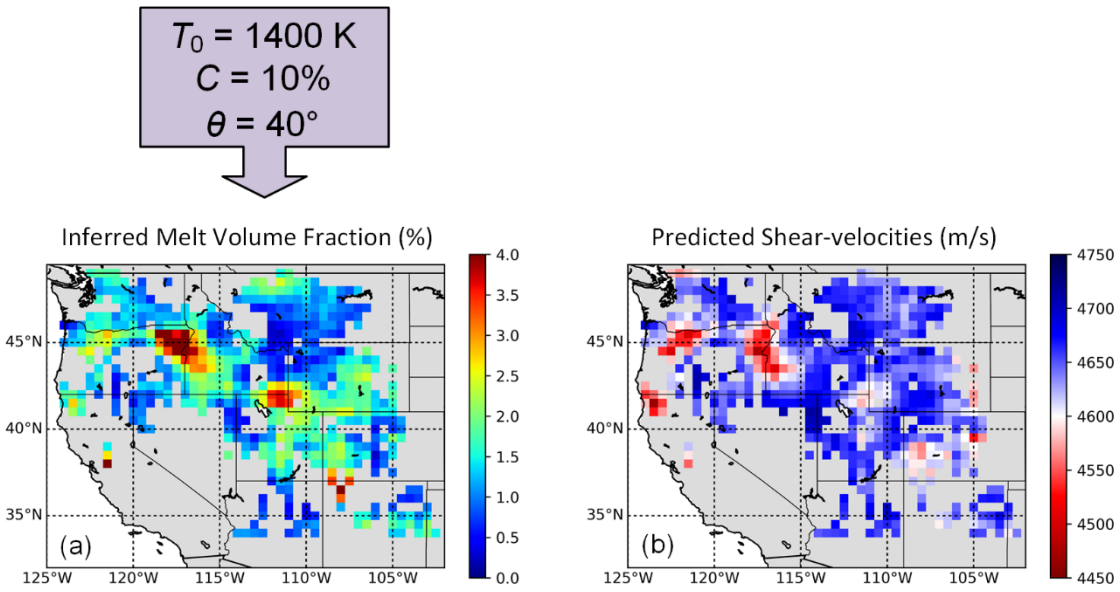

Figure 6.8 An end-member solution with the maximum melt vol. % within the LVL beneath the region. The regional averaged melt vol. % is 1.47% given $\boldsymbol{T_0}$ = 1400 K, $\boldsymbol{C}$ = 10% and $\boldsymbol{\theta}$ = 40°.

Note that this solution is directly derived from the initial solution, rather than from a brute-force search.

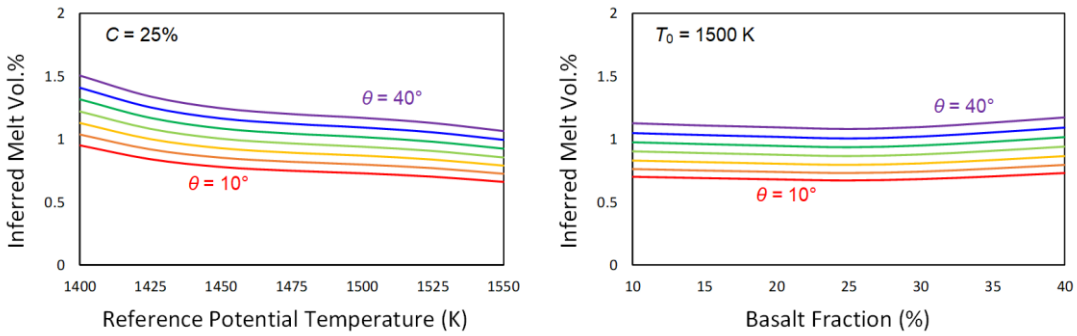

Figure 6.9 Inferred melt volume fractions beneath 106°W, 35°N (label A in fig. 6.1a) versus (a) the reference potential temperature for different dihedral angles ranging from 10° to 40° with constant intervals of 5° given a fixed basalt composition and (b) the basalt fraction in the bulk composition for a range of different dihedral angles given a fixed potential temperature.

6.6 Discussion

Using a numerical inversion approach, we have examined the LVL at 350 km underneath the western US. The shear-velocity anomalies and impedance contrasts in this zone are thought to indicate a small fraction of volatile-rich melt (Hier-Majumder and Tauzin, 2017) released either by decarbonation during the Farallon slab subduction (Thomson et al., 2016) or by dehydration from the upwelling of the Yellowstone mantle plume or small-scale convection within the MTZ (Bercovici and Karato, 2003; Richard and Bercovici, 2009; Zhang et al., 2018). Despite the presence of petrological and geochemical evidences of melting near the MTZ, determination of the quantity of melting from seismic signatures remains challenging owing to the trade-

offs that exist between various controlling factors. Due to the lack of geophysical and geochemical constraints, it is difficult, if not impossible, to distinguish the individual effects of temperature, composition and partial melting. A recent study has further suggested that these multiple controls are strongly correlated, leading to a disagreement between experimental measurements and theoretical estimates (Freitas et al., 2019).

Our numerical scheme based on a symmetry is able to cover all solutions. Using a forward model, we firstly generate an arbitrary solution assuming T_0 = 1500 K, C = 18% and θ = 25°. This is a successful solution as the shear wave velocities it predicts are consistent with the observations. The inverse problem is then linearized to find neighbouring solutions to the initial solution. As the controlling parameters have only a limited range of plausible values (in this work 1400 ≤ T_0 ≤ 1800 K, 10% ≤ C ≤ 40% and 10° ≤ θ ≤ 40°), the symmetry gives a quasi-complete set of solutions subject to the necessary constraint that the melt volume fraction in the upper mantle must always be non-negative. This constraint can be justified as the effects of temperature and composition are already taken into account. Given the above treatment, it is then a simple matter to find the combinations of parameters that reveals the end-member possibilities (e.g. maximum and minimum degrees of partial melting).

The modelling results show that a regional-averaged melt volume fraction of at least 0.51% is necessary to explain the sharp shear-velocity reductions at 350 km beneath the western US. This is the minimum extent of melting required to produce the observed LVL, whatever the solid mantle conditions and the geometry of the melt

are. As no solution has been found to be associated with a reference potential temperature higher than 1550 K, this is an upper-bound on the variations in the reference potential temperature. The modelling output also shows that the range of variations in basalt fraction depends on the assumed reference potential temperature. At a low reference potential temperature (e.g. 1400 K), the basalt fraction may vary from 10% to 40%. In contrast, at a higher reference potential temperature, solutions can only be in the basaltic-rich zone (e.g. fig. 6.6d). For instance, Hier-Majumder and Tauzin (2017) estimated the reference potential temperature as approximately 1550 K. If this is the case, then we can make a statement that the basalt fraction in the LVL beneath the western US is no less than 40%. Hence, whilst the thermal and compositional conditions are still under-constrained, our model work offers more reliable information about mantle physical properties.

In addition, our inverse method unravels trade-offs between parameters. As the forward model is nonlinear, there is no simple analytical tool for determining these competing effects. The numerical approach proposed here estimates the rates of change in the inferred melt volume fraction caused by changes in other parameters. The trade-offs between inferred melt volume fractions and other parameters can be summarized as:

(1) For a given dihedral angle and a given basalt fraction, the inferred melt volume fractions show a negative correlation with the assumed reference potential temperatures (fig. 6.6a & b).

(2) For a given reference potential temperature and a given dihedral angle, the

inferred melt volume fractions are insensitive to the assumed basalt fractions (fig. 6.6c & d).

(3) For a given reference potential temperature and a given basalt fraction, the inferred melt volume fractions show a modest positive correlation with the assumed dihedral angles (fig. 6.6e & f).

Another issue that needs to be addressed while deducing the physical properties of the LVL arises from the estimation of spatial variations in temperatures. This study calculates the temperature variations from the thickness of the MTZ using the empirical correlation proposed by Tauzin and Ricard (2014). The empirical model relies on several assumptions, for example that only temperature controls MTZ thickness and that no vertical variation occurs in temperature from the MTZ to the LVL. As observed from tomographic models (with low vertical resolution), the MTZ has consistent structures over the whole range of depth, in particular the stalled Juan de Fuca/Farallon slab (Burdick et al., 2008; Schmandt et al., 2011; Hier-Majumder and Tauzin, 2017). Although an entirely consistent MTZ should not be expected, dealing with the absolute topography of discontinuities to infer the temperatures would likely introduce more uncertainties, and would require a precise correction of the effect of shallow velocity heterogeneities from 3-D tomographic models, which have their own limitations. Another assumption involved here is that one can extract reliable MTZ thickness from receiver functions, while interference effects on the base of MTZ can be neglected. In fact, the move-out of interfering phases at the base of the MTZ is rather different from the one from direct conversions (Guan and Niu, 2017). Stacking along

move-out curves for direct conversions is efficient in removing the effect of these interfering phases. Besides, slant-stack diagrams and slowness weighted stacking (e.g. Guan and Niu, 2017; Hier-Majumder and Tauzin, 2017) show no evidence for any potential interference effects in several locations of the western US. As a consequence, the assumptions applied in the empirical model are tenable for calculating the temperature variations in the LVL.

Apart from the primary controls on the seismic velocities we have investigated, there are other factors that can influence the seismic wave speeds. In this work, the Clapeyron slopes γ are set to values from a compilation of experimentally obtained values (Tauzin and Ricard, 2014). The values of matrix density ρ_s and melt density ρ_m are set to constants as suggested in previous studies. The thickness of MTZ applied here are also from supplementary dataset whereas alternative empirical models (e.g. Keifer and Dueker, 2019) would produce different scenarios. These additional complications can lead to substantial uncertainties in estimated melt volume fractions. However, the inversion technique presented here is independent from the forward model and can easily be adapted to include these factors. While in this paper the application of the inversion has been demonstrated using 1-D column simulation, the technique could be applied to more sophisticated models that are spatially 2-D or 3-D. For future work, we intend to apply our modelling approach to investigating the LVL identified in other regions that differ in tectonic settings, for example, the Hawaii Islands (Huckfeldt et al., 2013) which are dominated by mantle plumes.

6.7 Conclusions

The interpretation of the observed seismic structures in the upper mantle, like many other geophysical inverse problems, is hampered by the fundamental challenge of non-uniqueness. In this work, we investigate the influence of thermal, compositional and melting effects on the pervasive LVL at 350 km beneath the western US. We develop an inversion scheme, based on the principle of symmetry, for generating the full range of solutions in the parameter space. Although a unique solution is not present, the calculation of an ensemble of solutions allows extraction of the properties that are common to all solutions. A key result of our inversion is that a minimum fraction of ~0.5% melt by volume is necessary to explain the seismically anomalous layer in the region. The scheme also encapsulates the ranges of variations in the thermal and compositional factors. Consequently, application of the proposed inversion technique can provide more robust interpretation of seismic velocity reductions within the mantle.

6.8 Acknowledgement

The authors would like to thank Editor Mark Jellinek and two anonymous reviewers for their constructive comments. Jie Xiao acknowledges support from the Strategic Priority Research Program of the Chinese Academy of Sciences (XDA14010103) and China National Major S&T Program (2017ZX05008-002-030). Jie Xiao also wishes to thank China Scholarship Council (CSC) for funding his PhD research.

7 Discussion

The examples displayed in Chapter 4 to 6 have demonstrated inverse problems from different aspects of geology and their implicit symmetries. As it is shown that, the principle of symmetry generally exists in geology and, once revealed by the proposed method, can bring four principle benefits:

1. It provides a generation rule. Using the underlying symmetry, a solution can be altered into another solution. Additional solutions to an inverse problem can be calculated given an existing solution.
2. It simplifies the inversion. Using simplifying assumptions, an initial solution can be generated first, which allows more realistic solutions to be found by applying the generation rule.
3. It reveals universal properties. Inspection of multiple solutions allows features that are common to all possible solutions (and hence the unknown, real solution) to be discovered.
4. It bounds the parameters. Some parameters are physically unreasonable. Excluding these from the ensemble of solutions leads to hard limits on the other controls of a geologic system.

This chapter revisits the applications presented earlier with further thoughts in terms of their symmetries and in terms of the advantages described above. Instead of concentrating on narrow issues relating to the specific geological problems tackled in

the individual cases, this chapter aims to demonstrate the commonalities that emerge when applying symmetry concepts to the disparate inverse problems.

7.1 The Stratigraphic Modelling Example

The example illustrated in Chapter 4 investigated non-unique interpretations of sequence architectures formed on continental margins. This initiated with a simple stratigraphic forward model of clastic delta controlled only by the interplay between (relative) sea-level and (cumulative) sediment supply, whereas complications such as multiple grain-sizes, subaerial erosion, compaction of sediment and transport out of the plane were ignored. As demonstrated in fig. 4.1, exactly the same sequence architectures can be modelled from more than one set of sea-level curve and sediment supply curve. The key to producing these identical architectures is that the sea-level vs. sediment supply curves are the same (Waltham et al., 2003). Hence, the symmetry is that the cross-section is unaltered by changes in sea-level and sediment supply provided these are changed in ways that conserve the sea level versus sediment supply curve.

Additional complications, for example multiple grain-sizes and subaerial erosion, were then introduced into the deltaic model and the simple symmetry given by the sea-level vs. sediment supply curve broke down. Nevertheless, for this more sophisticated model a symmetry still exists but is less straightforward than that in the previous model. This idea has been illustrated in fig. 4.5, showing identical results of model runs for two different sets of parameters. The first run was produced using an

arbitrary set of sediment supply curve, sea-level curve and coarse-to-fine ratio curve, assuming no erosion. The second model output has an identical cross-section but a non-zero subaerial erosion rate with altered sediment supply curve, sea-level curve and coarse-to-fine ratio curves.

The second run achieved by adding incremental change to the subaerial erosion rate and then adjusting the time-varying sediment supply, sea-level and coarse-to-fine ratio so that the model output matched the original output. Using a small increment of erosion ensures that the problem is linearized so that the new time-varying factors can be obtained from the old ones in a single step. The erosion rate was then increased again and the procedure repeated. The mathematical tool, developed for calculating the required changes in other factors to compensate the change in erosion rate, displayed an example of symmetric transformation. With this symmetry defined, the benefits of utilizing the symmetry, as outlined in the beginning of this chapter, can be described as follows.

Generation Rule

Given any solution (i.e. a sea-level vs. time curve *sl(t)* and a sediment supply vs. time curve ss(*t*) with single grain-size that successfully reproduce the desired architecture from a non-erosive model), the corresponding sea-level vs. sediment supply curve *sl(ss)* is first constructed. Then, one may invent a new *ss(t)*, subject to the constraints that it begins at zero, ends at the same final amount and is non-negative in its gradient at all times. This new *ss(t)* is then combined with the *sl(ss)* to produce a

new *sl(t)*. These ideas are illustrated in fig. 5.2. Then, using the iterative procedure outlined in fig. 4.4, each of these non-erosive models can be used to generate an associated series of erosive models. Note that the iterative procedure can be extended to more complicated models, as discussed in Chapter 4.

Inversion Simplification

An initial model can be built by assuming a simple sediment supply curve (e.g. sediment supply rate is constant with time) with no subaerial erosion. The generation rules described above can then be used to discover solutions that involve more realistic sediment supply history, sea-level oscillations, multiple grain-sizes and subaerial erosion. As presented in fig. 4.9, this method was adopted in the real-data example by generating a model match to deltaic architecture and well-constraints in the Neogene stratigraphy of Baltimore Canyon Trough, New Jersey, US.

Universal Properties

For a single grain-size, non-erosive model, the symmetry provided by the apparent *sl(ss)* guarantees that all resulting *sl(t)* are simply horizontally deformed versions compared to one-another, where the extents of stretch and compression vary in all solutions. As shown in fig. 4.2, all possible sea-level histories possess the same sequences of highstands and lowstands with the same amplitudes at each peak and trough; they just vary in the durations of these events. When subaerial erosion is

included, the sea-level peaks have to be higher, as can be seen in fig. 4.5 to 4.7. These patterns will not be discussed further here.

Transferable Limits

If age estimates (with errors) are available for at least some stratal surfaces in the deltaic cross-section, these limit the possible sediment supply curves and, hence, produce limits on possible sea-level curves (fig. 4.9). Another useful limiting factor is that it is not possible to supply a negative amount of sediment. As erosion increased, the sediment supply responds by having a sharp step-up, near to times of sea-level peaks, followed by a compensating reduction in the gradient of the sediment supply curve. Since the sediment supply rate must be non-negative, the upper limit can be found on the subaerial erosion rate beyond which the sediment supply curve has one, or more, negative-slope portions. Hence, there is also a maximum possible modification to sea-level. The points are demonstrated in fig. 4.9.

7.2 The Thermal History Modelling Example

The principle of symmetry, as discovered from the stratigraphic model, provides a general method for tackling inverse problems. Another application of the method is given in Chapter 5, where the symmetry of a downhole vitrinite maturation model was used to determine the heat flow history in a sedimentary basin. This work began with an inspection of the conventional thermal backstripping approach that had been previously invented for inferring thermal history from thermal indicator data. As

illustrated in fig. 5.1, the heat flow history can be unequivocally determined by the approach when tectonic evolution of the basin consists of only subsidence but no erosion or uplift. However, the approach produces non-unique solutions when erosion and uplift are involved in the burial paths of sedimentary layers, as shown in fig. 5.2. In this work, the symmetry of the model lies in that an existing heat flow curve can be properly altered with small changes to leave the vitrinite reflectance predicted from the model unchanged. Given this insight, the benefits of the symmetry method can be realized as follows:

Generation Rule

An iterative procedure, similar to that applied to the deltaic models, is proposed. Considering small changes in the vitrinite reflectance model allows the initial heat flow curve to be transformed into a smoother neighbouring solution (i.e. a heat flow curve with less complications) that gives the same model. In other words, some of the heat flow variations that are inessential to explain the observed data (this does not mean they did not happen) are removed from the initial heat flow curve. The new heat flow curve then gives a basis for further smoothing and the procedure repeats.

Inversion Simplification

Recognition of the fundamental of non-uniqueness in thermal history reconstruction leads to the symmetry-based inversion strategy as presented in fig. 5.7. With the influence of erosion or uplift on paleo-heat flow temporally ignored, an

apparent heat flow (vs. time) curve was first generated by thermal backstripping. Heat flow variations resulted from the erosion or uplift were then introduced into the model. Iterative application of the symmetry transformation allowed the end-member solutions that present the least variations (i.e. the smoothest possible heat flow curve to explain the vitrinite reflectance data) to be generated.

Universal Properties

In this specific application, benefits of inspecting universal properties of all solutions comes from an interesting way. That is, some paleo-heat flow variations that were suggested are shown not necessarily to be the case as they are absent in the end-member solutions. The real-case study in Chapter 5 examined a suspected heat flow spike during Mid to Late Permian in the Sichuan Basin, SW China. Application of the symmetry method showed that the vitrinite reflectance measured from a borehole in the basin can be well explained either by a short-live heat flow spike (fig. 5.9) or a long-term event (fig. 5.10 and fig. 5.11). As a consequence, the vitrinite reflectance data at present are insufficient to support a Permian heat flow anomaly in the region. In other words, a short-lived heat-flow flux is NOT a universal property of all solutions.

Transferable Limits

As presented in fig. 5.7, the iterations of symmetry transformation terminate when the approach fails to produce significant enough changes to the current solution. By definition, an end-member solution with the smoothest structure contains no

unwarranted information. Hence, the current heat flow curve can be thought of as the smoothest heat flow history ever possible. Note that this is different from the more conventional approach of generating the smoothest solution to avoid over-interpreting the data (e.g. Constable et al., 1987). All heat flow curves produced by the symmetry method can replicate the identical results and just vary in their appearance.

7.3 The Geophysical Example

This chapter now concludes with the geophysical example shown in Chapter 6. The key element to explore in this case was a widespread, but poorly continuous, seismically anomalous layer with lateral thickness ranged from tens to over a hundred kilometres atop the mantle transition zone below the western US. The sharp seismic velocity reductions observed at the upper-boundary of this layer were ascribed to the compositional heterogeneity caused by partial melting of the upper mantle. However, quantifying the partial melting effect is hampered by non-uniqueness. Specifically, the estimated degree of melting depends upon the assumed temperature in the mantle, basalt fraction of the bulk solid composition and geometry of melt-bearing aggregates. Hier-Majumder and Tauzin (2017) produced an estimate of the partial melting extent by making their best guess at the parameter values but Chapter 6 took this further by using the symmetry concepts to produce the full range of possible solutions. The results of this study can be described using the same set of benefits as used above for the other applications:

Generation Rule

A numerical approach, in a similar manner to the iterative procedures applied in the preceding examples, was developed for the geophysical problem. Then, using estimate from Hier-Majumder and Tauzin (2017) in fig. 6.5 as an initial solution, solutions for other values of mantle potential temperature (T_0), basalt fraction (C), dihedral angle of grain-melt contact (θ) and volume fraction of melt (φ) can be derived.

Inversion Simplification

In this specific application, this benefit is from an unexpected direction. A range of different solutions could, in principle, be generated using a conventional root-search approach as applied in Hier-Majumder and Tauzin (2017) which did not make explicit reference to symmetry ideas. However, such an approach is computationally prohibitive for more than a small number of parameter-sets. In contrast, the numerical procedure presented here for tracking the symmetry trajectories through the parameters space shows greater efficiency and many outputs can be rapidly calculated.

Universal Properties

Though the whole set of solutions differ with each other in the regional-averaged degrees of melt, all the inferred maps of melts show very similar spatial distribution of the relative variations of melt volume fractions. Unsurprisingly, all maps of melts (fig.

6.5c, 6.7c & 6.8c) are closely related to the map of shear-velocities observed (fig. 6.1d) as the greatest degrees of melting always occur in the location where shear-velocity is lowest. This discovery confirms a dominant control on the low-velocity layer by melting rather than by thermal anomaly. Inspection of the trade-off between multiple parameters in fig. 6.6 shows that, the melt volume fraction has a strong negative correlation with the mantle temperature and a modest positive correlation with the grain-melt dihedral angle. In comparison, the melt volume fraction appears to be insensitive to the basalt fraction.

Transferable Limits

The controlling potential parameters T_0, C and θ have only a limited range of plausible values (i.e. 1400 ≤ T_0 ≤ 1800 K, 10% ≤ C ≤ 40% and 10° ≤ θ ≤ 40°). Hence, symmetry can give a quasi-complete set of solutions (i.e. solutions on a closely spaced grid in the parameter space). In addition, because it is impossible to produce a negative degree of melting beneath any location, any solution that involves negative melt volume fractions should be excluded. Given these constraints, it is then a simple matter to find the combinations of parameters that give the minimum (fig. 6.7) and maximum (fig. 6.8) degrees of partial melting. An extent of at least ~0.5 vol.% melt is found to be essential to the low-velocity layer beneath the western US. The symmetry method also encapsulates the variations in the solid mantle properties. In particular, an upper-bound of 1550 K is placed upon the potential temperature in the region.

8 Conclusions

Inverse problems in geology are to deduce paleohistory from observations at present or, alternatively, to deduce structure at depth from data collected at the surface. A fundamental challenge, both for real-world geology and for computer models, is the non-uniqueness as there could be more than one interpretation for same data. The principle of symmetry provides a powerful tool for tackling non-uniqueness but was previously used only in simple inverse problems where analytical expressions are available. This thesis invented a numerical algorithm which enables the symmetry concepts to be easily adapted to non-linear, more complicated problems. This algorithm has shown to be applicable in various quantitative models from a wide spectrum of geology. The symmetry of an inverse problem indicates trajectories in the parameter space that connect possible solutions, i.e. they describe transformations that do not alter the predictions of a model. Exploring symmetries of computer models provides useful insights into inverse problems in that it allows easy generation of an initial starting model, rapid calculation of multiple solutions, clear understanding of the common features of all solutions and firm statements to be made concerning the whole range of possible solutions. Applications of the proposed method in real-world geology and resulting benefits in specific cases can be summarized as follows:

1. *An application in sedimentology*. This work interpreted the Neogene stratigraphy of Baltimore Canyon Trough in New Jersey, US. The symmetry

method was applied to a stratigraphic model that incorporates relative sea-level, sediment supply, coarse-to-fine ratio, subaerial erosion and tectonic rotation. As it was shown that, whilst the sequence architecture observed corresponds to an infinite number of interpretations, these are very similar to each other. In particular, the relative sea-level history in every possible solution indicates the same sequence of oscillations. Calculation of multiple solutions also allows variations in the multiple stratal controls, in particular the amplitudes of relative sea-level, the magnitudes of sediment supply and the rates of subaerial erosion, to be encapsulated. Hence, application of the method can offer more robust interpretations of the stratal controls and hence better understanding of depositional sequences. Application of the method can also provide more reliable information of the sedimentary record and hence more precise evidence of paleoclimate.

2. *An application in thermochronology*. This work looked at the thermal history, in particular the paleo-heat flow in the Sichuan Basin, Southwestern China. The symmetry method was applied to a vitrinite reflectance model, where the thermal maturities of organic matters are simulated from prescribed tectonic and thermal events. The model work showed that thermal histories reconstructed for the basin are poorly constrained especially for the periods prior to the Permian. However, all scenarios inferred suggest that the basin underwent abnormally high temperature during Mid to Late Permian, though it remains unclear whether this was caused by a short-lived event or

by permanent variations in the heat flow. This suggests that the previously suspected ancient mantle plumes near the Sichuan Basin during Permian might not necessarily be true. However, the complete set of solutions can allow more accurate assessment of hydrocarbon generation beneath the basin to reduce exploration risk.

3. *An example in geophysics*. This work explored the thermal anomalies and compositional heterogeneity of a seismically low-velocity layer atop the mantle transition zone. The symmetry method is applied to a petrologic model that predicts velocities reductions the as seismic waves transport into a partially molten rock. The model work showed that the seismic velocity reductions are a consequence of the interplay between mantle temperature, bulk solid composition and partial melting. A unique inversion of the seismic properties is unavailable because the control factors can trade off with each other. However, modelling results indicate that a minimum of 0.5 vol.% volatile-induced melt is essential to reproduce the LVL below the western US. The calculation also bounds limits on the thermal and compositional conditions of the solid mantle beneath the region. These discoveries can enable more reliable estimate of volatile amount within the low-velocity layer, which advances understanding of volatile transport from the mantle transition zone.

There do not appear to be any limits to the inverse problems that could benefit from exploration of the problem's symmetries. Any inverse problem can be linearized

by considering small enough increments of change and, once this has been done, the numerical procedure proposed here for finding a neighboring solution, given an initial solution, can be applied. The calculation will find families of solutions whenever they are connected by a smooth trajectory through the problem's parameter space. One can anticipate that applying the symmetry method will offer all of the benefits demonstrated by the examples illustrated in this thesis. Given all these benefits, the symmetry method should take its place amongst the battery of techniques used to address inverse problems.

Appendix 1 Pseudocode for Determining Symmetries in Numerical Models

A Python-like computer program is presented here to display implementation of the numerical algorithm, as proposed in Chapter 3, for determining symmetries in forward models. The program involves three scripts: 1. 'Main.py' that offers an entry to the program; 2. 'Model.py' that builds a general framework to allow development of specific forward models and 3. 'Tansform.py' that calculates multiple solutions for a forward model.

```
##########################################################################
Main.py:
from Model import *
from Transform import *
if __name__ == '__main__':
    # Enter length of input and output vectors
    global para_len, model_len = User_Input()
    # Input time and time-varying variables x and y
    t, x, y = User_Input()
    # Check the length of input vectors
    if not(len(t) == para_len and len(x) == para_len and len(y) == para_len):
```

```
        System_exit("Parameter length are not aligned.")
    # Iteration for calculating additional solutions of variables x, y
    while user_condition == true:
        # Run default model
        z = Model(t, x, y)
        z.Run()
        # Give small changes to variable y and run the model again
        delta_y = User_Input()
        zp = Model(t, x, y + delta_y)
        zp.Run()
        # Calculate residual caused in the model
        delta_z = zp.value - z.value
        # Calculate partial derivatives of the model with respect to x
        dzdx = Get_dfdx(t, x, y, z)
        # Calculate changes required in y to restore the model
        delta_x = Solve(t, dfdx, x, -1.0 * delta_z)
        # Update variables
        x = x+ delta_x
        y = y + delta_y
```

##

Model.py:

```
# Class 'Model' defines a general function z = f(x, y)
    class Model:
    # Arguments t, x and y indicate input vectors of time, variable x and variable y
    def __init__(self, t, x, y):
        self.time = t
        self.varx = x
        self.vary = y
        self.value = np.zeros(model_len, dtype = float)
        self.Run()
    del Run(self):
        # Run the forward model
        User_Process()


#########################################################################
Transform.py:
import numpy as np
from Model import *


# Calculate partial derivatives
def Get_dzdx(t, x, y, z):
    # Give small changes to variable x and see changes in the model
    delta_x = x * 1e-3
```

```
        zp = Model(t, x + delta_x, y)
        zp.Run()
        dfdx = (zp.value - z.value) / delta_x
        return dfdx


# Solve delta_x
def Solve(t, A, x, delta_z):
        N, M = A.shape
        Nt = len(t)
        if M == N:
                delta_x = np.linalg.solve(A, delta_z)
        elseif M < N:
                # Find the least-square solution
                delta_x = np.linalg.solve(np.dot(A.T, A), np.dot(A.T, delta_z))
        else:
                # Storage for matrix of coefficients given by first derivatives
                D = np.zeros((Nt - 1, Nt - 1), dtype = float)
                # Input user options
                opt = User_Input()
                if opt == 0: """ Find minimum-norm adjustment
                        Lambda = -2 * np.linalg.solve((np.dot(A, A.T), delta_z)
                        delta_x = -0.5 * np.dot(A.T, Lambda)
```

```
    else:
        # Penalty parameter
        theta = 1e6
        if opt == 1: """ Find first derivative smoothest adjustment
            # Construct matrix of coefficients given by first derivatives
            for i in range(1, Nt - 2):
                D[i][i - 1] = 1 / (t[i - 1] - t[i])
                D[i][i] = 1 / (t[i] - t[i - 1])
        elif opt == 2: """ Find second derivative smoothest adjustment
            # Construct matrix of coefficients given by second derivatives
            for i in range(1, Nt - 2):
                D[i][i - 1] = 1 / (t[i] - t[i - 1])
                D[i][i] = (t[i - 1] - t[i + 1]) / ((t[i + 1] - t[i]) * (t[i] - t[i - 1]))
                D[i][i + 1] = 1 / (t[i + 1] - t[i])
        else:
            System_exit("Invalid option.")
        DTD = np.dot(D.T, D)
        ATA = np.dot(A.T, A)
        delta_x = -1 * np.linalg.solve(theta**2 * ATA + DTD,\
            theta * np.dot(A.T, delta_z) - np.dot(DTD, x))
return delta_x
```

Appendix 2 Using Symmetry to Calculate Multiple Solutions to a Simple Stratigraphic Model

A stratigraphic forward model controlled by sediment supply, sea-level and subaerial erosion can be formulated as $\boldsymbol{h} = \boldsymbol{F}(\boldsymbol{ss}, \boldsymbol{sl}, \boldsymbol{e})$, where $\boldsymbol{h} = (\boldsymbol{h_{11}}, \boldsymbol{h_{12}}, \dots, \boldsymbol{h_{1N}}, \boldsymbol{h_{21}}, \boldsymbol{h_{22}}, \dots, \boldsymbol{h_{2N}}, \boldsymbol{h_{M1}}, \boldsymbol{h_{M2}}, \dots, \boldsymbol{h_{MN}})^{\mathbf{T}}$ is an observed stratal geometry described by the heights of the $\boldsymbol{M}$ stratal surfaces at $\boldsymbol{N}$ horizontal positions; $\boldsymbol{ss} = (\boldsymbol{ss_1}, \boldsymbol{ss_2}, \dots, \boldsymbol{ss_M})^{\mathbf{T}}$ and $\boldsymbol{sl} = (\boldsymbol{sl_1}, \boldsymbol{sl_2}, \dots, \boldsymbol{sl_M})^{\mathbf{T}}$ are sediment supply and sea-level accounting for the stratal surfaces, respectively; $\boldsymbol{e}$ is subaerial erosion rate.

When a perturbation ($\Delta\boldsymbol{e}$) is given to the subaerial erosion rate, a residual is subsequently caused in the model. The residual, however, may be compensated by appropriate adjustments in sediment supply ($\Delta\boldsymbol{ss}$) and sea-level ($\Delta\boldsymbol{sl}$). Using first-order Taylor Series, this can be expressed as:

$$\boldsymbol{d} + \nabla_{\boldsymbol{ss}}\boldsymbol{F}(\boldsymbol{ss}, \boldsymbol{sl}, e) \cdot \Delta\boldsymbol{ss} + \nabla_{\boldsymbol{sl}}\boldsymbol{F}(\boldsymbol{ss}, \boldsymbol{sl}, e) \cdot \Delta\boldsymbol{sl} = \boldsymbol{\rho} \qquad \text{(A.1)}$$

, where $\boldsymbol{d} = \boldsymbol{F}(\boldsymbol{ss}, \boldsymbol{sl}, e + \Delta e) - \boldsymbol{F}(\boldsymbol{ss}, \boldsymbol{sl}, e)$ is the residual caused by Δe; $\nabla_{\boldsymbol{ss}}\boldsymbol{F}(\boldsymbol{ss}, \boldsymbol{sl}, e)$, $\nabla_{\boldsymbol{sl}}\boldsymbol{F}(\boldsymbol{ss}, \boldsymbol{sl}, e)$ are partial derivatives with respect to $\boldsymbol{ss}$ and $\boldsymbol{sl}$ and can be calculated from the forward model using finite difference method; $\boldsymbol{\rho}$ is the term of remainder. If $\boldsymbol{d}$ could be well compensated by $\Delta\boldsymbol{ss}$ and $\Delta\boldsymbol{sl}$ then $\boldsymbol{\rho} \to \mathbf{0}$. Note that $\boldsymbol{d}$ is a matrix in size of $M \times N$, whilst $\Delta\boldsymbol{ss}$ and $\Delta\boldsymbol{sl}$ are both vectors with a length of M. Every element in $\Delta\boldsymbol{ss}$ and $\Delta\boldsymbol{sl}$ can make a difference in the model

and hence $\nabla_{\boldsymbol{ss}}\boldsymbol{F}(\boldsymbol{ss},\boldsymbol{sl},e)$ and $\nabla_{\boldsymbol{sl}}\boldsymbol{F}(\boldsymbol{ss},\boldsymbol{sl},e)$ are both matrices in size of $M \times N \times M$.

Let $\mathrm{A} = \nabla_{\boldsymbol{ss}}\boldsymbol{F}(\boldsymbol{ss},\boldsymbol{sl},e)$ and $\mathrm{B} = \nabla_{\boldsymbol{sl}}\boldsymbol{F}(\boldsymbol{ss},\boldsymbol{sl},e)$. Writing the equation in full gives:

$$\sum_{i=1}^{M\times N}\left(d_i + \sum_{j=1}^{M} A_{ij}\,\Delta ss_j + \sum_{j=1}^{M} B_{ij}\,\Delta sl_j\right) = \sum_{i=1}^{M\times N}\rho_i \tag{A.2}$$

Thus, there are $M \times N$ equations and $M \times 2$ unknowns (i.e. the M elements in $\Delta\boldsymbol{ss}$ and the M elements in $\Delta\boldsymbol{sl}$). Provided $N \gg 2$, the problem of solving $\Delta\boldsymbol{ss}$ and $\Delta\boldsymbol{sl}$ from eq. A-2 is over-determined. Using least square solution, the square error can be calculated as:

$$\boldsymbol{\rho}^2 = \sum_{i=1}^{M\times N}\rho_i^2 = \sum_{i=1}^{M\times N}\left(d_i + \sum_{j=1}^{M} A_{ij}\Delta ss_j + \sum_{j=1}^{M} B_{ij}\Delta sl_j\right)^2 \tag{A.3}$$

To minimize $\boldsymbol{\rho}$, set $\partial\boldsymbol{\rho}^2/\,\partial\Delta ss_k = 0$ and $\partial\boldsymbol{\rho}^2/\,\partial\Delta sl_l = 0$ $(k,l = 1,2,\dots,M)$:

$$\begin{cases} 2\cdot\sum_{i=1}^{M\times N}\left(d_i + \sum_{j=1}^{M} A_{ij}\Delta ss_j + \sum_{j=1}^{M} B_{ij}\Delta sl_j\right)\cdot A_{ik} = 0 \\ 2\cdot\sum_{i=1}^{M\times N}\left(d_i + \sum_{j=1}^{M} A_{ij}\Delta ss_j + \sum_{j=1}^{M} B_{ij}\Delta sl_j\right)\cdot B_{il} = 0 \end{cases} \tag{A.4}$$

, which may be rearranged as:

$$\begin{cases} \sum_{i=1}^{M\times N} A_{ik}d_i + \sum_{j=1}^{M}\sum_{i=1}^{M\times N} A_{ik}A_{ij}\Delta ss_j + \sum_{j=1}^{M}\sum_{i=1}^{M\times N} A_{ik}B_{ij}\Delta sl_j = 0 \\ \sum_{i=1}^{M\times N} B_{il}d_i + \sum_{j=1}^{M}\sum_{i=1}^{M\times N} B_{il}A_{ij}\Delta ss_j + \sum_{j=1}^{M}\sum_{i=1}^{M\times N} B_{il}B_{ij}\Delta sl_j = 0 \end{cases} \tag{A.5}$$

Equation A-5 may be written in matrix notation:

$$\begin{cases} \mathrm{A}^{\mathrm{T}}\boldsymbol{d} + \mathrm{A}^{\mathrm{T}}\mathrm{A} \cdot \Delta\boldsymbol{ss} + \mathrm{A}^{\mathrm{T}}\mathrm{B} \cdot \Delta\boldsymbol{sl} = \mathbf{0} \\ \mathrm{B}^{\mathrm{T}}\boldsymbol{d} + \mathrm{B}^{\mathrm{T}}\mathrm{A} \cdot \Delta\boldsymbol{ss} + \mathrm{B}^{\mathrm{T}}\mathrm{B} \cdot \Delta\boldsymbol{sl} = \mathbf{0} \end{cases} \tag{A.6}$$

Therefore, the least square solution to eq. A.1 is:

$$\begin{cases} \Delta\boldsymbol{ss} = [(\mathrm{B}^{\mathrm{T}}\mathrm{B})^{-1}\mathrm{B}^{\mathrm{T}}\mathrm{A} - (\mathrm{A}^{\mathrm{T}}\mathrm{B})^{-1}\mathrm{A}^{\mathrm{T}}\mathrm{A}]^{-1} \cdot [(\mathrm{A}^{\mathrm{T}}\mathrm{B})^{-1}\mathrm{A}^{\mathrm{T}} - (\mathrm{B}^{\mathrm{T}}\mathrm{B})^{-1}\mathrm{B}^{\mathrm{T}}] \cdot \boldsymbol{d} \\ \Delta\boldsymbol{sl} = [(\mathrm{A}^{\mathrm{T}}\mathrm{A})^{-1}\mathrm{A}^{\mathrm{T}}\mathrm{B} - (\mathrm{B}^{\mathrm{T}}\mathrm{A})^{-1}\mathrm{B}^{\mathrm{T}}\mathrm{B}]^{-1} \cdot [(\mathrm{B}^{\mathrm{T}}\mathrm{A})^{-1}\mathrm{B}^{\mathrm{T}} - (\mathrm{A}^{\mathrm{T}}\mathrm{A})^{-1}\mathrm{A}^{\mathrm{T}}] \cdot \boldsymbol{d} \end{cases} \tag{A.7}$$

Given the above $\Delta\boldsymbol{ss}$ and $\Delta\boldsymbol{sl}$, $\boldsymbol{F}(\boldsymbol{ss} + \Delta\boldsymbol{ss}, \boldsymbol{sl} + \Delta\boldsymbol{sl}, e + \Delta e) = \boldsymbol{F}(\boldsymbol{ss}, \boldsymbol{sl}, e)$

and hence the model remains unaltered.

References

Ali, J. R., Fitton, J. G., and Herzberg, C., 2010, Emeishan large igneous province (SW China) and the mantle-plume up-doming hypothesis: Journal of the Geological Society, v. 167, no. 5, 953-959.

Allen, P. A., and Allen, J. R., 2013, Thermal history, Basin analysis: Principles and application to petroleum play assessment: United Kingdom, Wiley-Blackwell, pp. 345-370.

Backus, G., and Gilbert, F., 1970, Uniqueness in the inversion of inaccurate gross earth data: Philosophical Transactions of the Royal Society of London. Series A, Mathematical and Physical Sciences, v. 266, no. 1173, 123-192.

Barker, C. E., and Pawlewicz, M. J., 1994, Calculation of vitrinite reflectance from thermal histories and peak temperatures: a comparison of methods, ACS Publications.

Barrell, J., 1917, Rhythms and the measurements of geologic time: Bulletin of the Geological Society of America, v. 28, no. 1, 745-904.

Beck, A., 1976, An improved method of computing the thermal conductivity of fluid-filled sedimentary rocks: Geophysics, v. 41, no. 1, 133-144.

Beck, A., Anglin, F., and Sass, J., 1971, Analysis of heat flow data-In situ thermal conductivity measurements: Canadian Journal of Earth Sciences, v. 8, no. 1, 1-19.

Bercovici, D., and Karato, S.-i., 2003, Whole-mantle convection and the transition-zone water filter: Nature, v. 425, no. 6953, 39.

Best, J. L., and Ashworth, P. J., 1997, Scour in large braided rivers and the recognition of sequence stratigraphic boundaries: Nature, v. 387, no. 6630, 275.

Bornholdt, S., Nordlund, U., and Westphal, H., 1999, Inverse stratigraphic modeling using genetic algorithms.

Boylan, A., Waltham, D., Bosence, D., Badenas, B., and Aurell, M., 2002, Digital rocks: linking forward modelling to carbonate facies: Basin Research, v. 14, no. 3, 401-415.

Bray, R., Green, P., and Duddy, I., 1992, Thermal history reconstruction using apatite fission track analysis and vitrinite reflectance: a case study from the UK East Midlands and Southern North Sea: Geological Society, London, Special Publications, v. 67, no. 1, 3-25.

Bullard, E. C., 1954, The flow of heat through the floor of the Atlantic Ocean: Proceedings of the Royal Society of London. Series A. Mathematical and Physical Sciences, v. 222, no. 1150, 408-429.

Burdick, S., Li, C., Martynov, V., Cox, T., Eakins, J., Mulder, T., Astiz, L., Vernon, F. L., Pavlis, G. L., and van der Hilst, R. D., 2008, Upper mantle heterogeneity beneath North America from travel time tomography with global and USArray transportable array data: Seismological Research Letters, v. 79, no. 3, 384-392.

Burgess, P., and Allen, P., 1996, A forward-modelling analysis of the controls on sequence stratigraphical geometries: Geological Society, London, Special Publications, v. 103, no. 1, 9-24.

Burgess, P. M., 2012, A brief review of developments in stratigraphic forward modelling, 2000–2009: Regional Geology and Tectonics: Principles of Geologic Analysis, v. 1, 379-404.

Burgess, P. M., Lammers, H., van Oosterhout, C., and Granjeon, D., 2006, Multivariate sequence stratigraphy: Tackling complexity and uncertainty with stratigraphic forward modeling, multiple scenarios, and conditional frequency maps: AAPG bulletin, v. 90, no. 12, 1883-1901.

Burgess, P. M., and Prince, G. D., 2015, Non-unique stratal geometries: implications for sequence stratigraphic interpretations: Basin Research, v. 27, no. 3, 351-365.

Burgess, P. M., and Steel, R. J., 2017, How To Interpret, Understand, and Predict Stratal Geometries Using Stratal-Control Spaces and Stratal-Control-Space Trajectories: Journal of Sedimentary Research, v. 87, no. 4, 325-337.

Burnham, A. K., and Sweeney, J. J., 1989, A chemical kinetic model of vitrinite maturation and reflectance: Geochimica et Cosmochimica Acta, v. 53, no. 10, 2649-2657.

Burton, R., Kendall, C. G. S. C., and Lerche, I., 1987, Out of our depth: on the impossibility of fathoming eustasy from the stratigraphic record: Earth-Science Reviews, v. 24, no. 4, 237-277.

Cao, S., and Lerche, I., 1990, Basin modelling: applications of sensitivity analysis: Journal of Petroleum Science and Engineering, v. 4, no. 2, 83-104.

Carrapa, B., DeCelles, P. G., Reiners, P. W., Gehrels, G. E., and Sudo, M., 2009, Apatite triple dating and white mica 40Ar/39Ar thermochronology of syntectonic detritus in the Central Andes: A multiphase tectonothermal history: Geology, v. 37, no. 5, 407-410.

Carvajal, C., Steel, R., and Petter, A., 2009, Sediment supply: the main driver of shelf-margin growth: Earth-Science Reviews, v. 96, no. 4, 221-248.

Catuneanu, O., and Zecchin, M., 2013, High-resolution sequence stratigraphy of clastic shelves II: controls on sequence development: Marine and Petroleum Geology, v. 39, no. 1, 26-38.

Chamberlin, T. C., 1890, The method of multiple working hypotheses: Science, v. 15, no. 366, 92-96.

Charvin, K., Gallagher, K., Hampson, G. L., and Labourdette, R., 2009a, A Bayesian approach to inverse modelling of stratigraphy, part 1: Method: Basin Research, v. 21, no. 1, 5-25.

Charvin, K., Hampson, G. J., Gallagher, K., and Labourdette, R., 2009b, A Bayesian approach to inverse modelling of stratigraphy, part 2: Validation tests: Basin Research, v. 21, no. 1, 27-45.

Chung, S.-L., and Jahn, B.-m., 1995, Plume-lithosphere interaction in generation of the Emeishan flood basalts at the Permian-Triassic boundary: Geology, v. 23, no. 10, 889-892.

Conaway, J. G., and Beck, A., 1977, Fine-scale correlation between temperature gradient logs and lithology: Geophysics, v. 42, no. 7, 1401-1410.

Constable, S. C., Parker, R. L., and Constable, C. G., 1987, Occam's inversion: A practical algorithm for generating smooth models from electromagnetic sounding data: Geophysics, v. 52, no. 3, 289-300.

Corrigan, J., 1991, Inversion of apatite fission track data for thermal history information: Journal of Geophysical Research: Solid Earth, v. 96, no. B6, 10347-10360.

Courtier, A. M., Jackson, M. G., Lawrence, J. F., Wang, Z., Lee, C.-T. A., Halama, R., Warren, J. M., Workman, R., Xu, W., and Hirschmann, M. M., 2007, Correlation of seismic and petrologic thermometers suggests deep thermal anomalies beneath hotspots: Earth and Planetary Science Letters, v. 264, no. 1-2, 308-316.

Courtier, A. M., and Revenaugh, J., 2007, Deep upper-mantle melting beneath the Tasman and Coral Seas detected with multiple ScS reverberations: Earth and Planetary Science Letters, v. 259, no. 1-2, 66-76.

Cross, T. A., and Lessenger, M. A., 1999, Construction and application of a stratigraphic inverse model.

Crowley, K. D., 1993, Lenmodel: a forward model for calculating length distributions and fission-track ages in apatite: Computers & Geosciences, v. 19, no. 5, 619-626.

De Bremaecker, J.-C., 1983, Temperature, subsidence, and hydrocarbon maturation in extensional basins: a finite element model: AAPG Bulletin, v. 67, no. 9, 1410-1414.

Dziewonski, A. M., and Anderson, D. L., 1981, Preliminary reference Earth model: Physics of the earth and planetary interiors, v. 25, no. 4, 297-356.

Elliott, J., and Dawber, P., 1979, Symmetry in Physics, Volume 1 and 2, Macmillan Press, London.

Fee, D., and Dueker, K., 2004, Mantle transition zone topography and structure beneath the Yellowstone hotspot: Geophysical Research Letters, v. 31, no. 18.

Ferrero, C., and Gallagher, K., 2002, Stochastic thermal history modelling. 1. Constraining heat flow histories and their uncertainty: Marine and Petroleum Geology, v. 19, no. 6, 633-648.

Flemings, P. B., and Grotzinger, J. P., 1996, STRATA: Freeware for analyzing classic stratigraphic problems: GSA Today, v. 6, no. 12, 1-7.

Freitas, D., Manthilake, G., Chantel, J., Bouhifd, M., and Andrault, D., 2019, Simultaneous measurements of electrical conductivity and seismic wave velocity of partially molten geological materials: effect of evolving melt texture: Physics and Chemistry of Minerals, 1-17.

Frostick, L. E., and Jones, S. J., 2002, Impact of periodicity on sediment flux in alluvial systems: grain to basin scale: Geological Society, London, Special Publications, v. 191, no. 1, 81-95.

Gallagher, K., 1988, The subsidence history and thermal state of the Eromanga and Cooper Basins: PhD thesis, Australian National University.

Gallagher, K., 1995, Evolving temperature histories from apatite fission-track data: Earth and Planetary Science Letters, v. 136, no. 3-4, 421-435.

Gallagher, K., 2012, Transdimensional inverse thermal history modeling for quantitative thermochronology: Journal of Geophysical Research: Solid Earth, v. 117, no. B2.

Gallagher, K., Charvin, K., Nielsen, S., Sambridge, M., and Stephenson, J., 2009, Markov chain Monte Carlo (MCMC) sampling methods to determine optimal models, model resolution and model choice for Earth Science problems: Marine and Petroleum Geology, v. 26, no. 4, 525-535.

Gallagher, K., and Sambridge, M., 1992, The resolution of past heat flow in sedimentary basins from non-linear inversion of geochemical data: the smoothest model approach, with synthetic examples: Geophysical Journal International, v. 109, no. 1, 78-95.

Gao, W., Matzel, E., and Grand, S. P., 2006, Upper mantle seismic structure beneath eastern Mexico determined from P and S waveform inversion and its implications: Journal of Geophysical Research: Solid Earth, v. 111, no. B8.

George, A. D., Marshallsea, S. J., Wyrwoll, K.-H., Jie, C., and Yanchou, L., 2001, Miocene cooling in the northern Qilian Shan, northeastern margin of the Tibetan Plateau, revealed by apatite fission-track and vitrinite-reflectance analysis: Geology, v. 29, no. 10, 939-942.

Ghosh, S., Ohtani, E., Litasov, K., Suzuki, A., and Sakamaki, T., 2007, Stability of carbonated magmas at the base of the Earth's upper mantle: Geophysical research letters, v. 34, no. 22.

Granjeon, D., and Joseph, P., 1999, Concepts and applications of a 3-D multiple lithology, diffusive model in stratigraphic modeling.

Green, P. F., Duddy, I. R., Gleadow, A. J., and Lovering, J. F., 1989, Apatite fission-track analysis as a paleotemperature indicator for hydrocarbon exploration, Thermal history of sedimentary basins, Springer, pp. 181-195.

Guan, Z., and Niu, F., 2017, An investigation on slowness-weighted CCP stacking and its application to receiver function imaging: Geophysical Research Letters, v. 44, no. 12, 6030-6038.

Gubbins, D., 2004, Time series analysis and inverse theory for geophysicists, Cambridge University Press, pp. 17-18.

Guillot, B., and Sator, N., 2007, A computer simulation study of natural silicate melts. Part II: High pressure properties: Geochimica et Cosmochimica Acta, v. 71, no. 18, 4538-4556.

Hardy, S., Dart, C. J., and Waltham, D., 1994, Computer modelling of the influence of tectonics on sequence architecture of coarse-grained fan deltas: Marine and Petroleum Geology, v. 11, no. 5, 561-574.

Hardy, S., and Waltham, D., 1992, Computer modeling of tectonics, eustacy, and sedimentation using the Macintosh: Geobyte, v. 7, 42-42.

He, B., Xu, Y.-G., Wang, Y.-M., and Luo, Z.-Y., 2006, Sedimentation and lithofacies paleogeography in southwestern China before and after the Emeishan flood volcanism: new insights into surface response to mantle plume activity: The Journal of Geology, v. 114, no. 1, 117-132.

He, L., Xu, H., and Wang, J., 2011, Thermal evolution and dynamic mechanism of the Sichuan Basin during the Early Permian-Middle Triassic: Science China Earth Sciences, v. 54, no. 12, 1948-1954.

Helland-Hansen, W., and Gjelberg, J. G., 1994, Conceptual basis and variability in sequence stratigraphy: a different perspective: Sedimentary Geology, v. 92, no. 1-2, 31-52.

Helland-Hansen, W., and Hampson, G., 2009, Trajectory analysis: concepts and applications: Basin Research, v. 21, no. 5, 454-483.

Heller, P. L., Burns, B. A., and Marzo, M., 1993, Stratigraphic solution sets for determining the roles of sediment supply, subsidence, and sea level on transgressions and regressions: Geology, v. 21, no. 8, 747-750.

Hier-Majumder, S., 2017, MuMaP_fwd-1.0, Version: (Version 1.0). Zenodo, http://doi.org/10.5281/zenodo.1040971.

Hier-Majumder, S., and Abbott, M. E., 2010, Influence of dihedral angle on the seismic velocities in partially molten rocks: Earth and Planetary Science Letters, v. 299, no. 1-2, 23-32.

Hier-Majumder, S., and Courtier, A., 2011, Seismic signature of small melt fraction atop the transition zone: Earth and Planetary Science Letters, v. 308, no. 3-4, 334-342.

Hier-Majumder, S., Keel, E. B., and Courtier, A. M., 2014, The influence of temperature, bulk composition, and melting on the seismic signature of the low-velocity layer above the transition zone: Journal of Geophysical Research: Solid Earth, v. 119, no. 2, 971-983.

Hier-Majumder, S., and Tauzin, B., 2017, Pervasive upper mantle melting beneath the western US: Earth and Planetary Science Letters, v. 463, 25-35.

Hood, A., Gutjahr, C., and Heacock, R., 1975, Organic metamorphism and the generation of petroleum: AAPG bulletin, v. 59, no. 6, 986-996.

Hopcroft, P. O., Gallagher, K., and Pain, C. C., 2007, Inference of past climate from borehole temperature data using Bayesian Reversible Jump Markov chain Monte Carlo: Geophysical Journal International, v. 171, no. 3, 1430-1439.

Huckfeldt, M., Courtier, A. M., and Leahy, G. M., 2013, Implications for the origin of Hawaiian volcanism from a converted wave analysis of the mantle transition zone: Earth and Planetary Science Letters, v. 373, 194-204.

Jasbinsek, J., and Dueker, K., 2007, Ubiquitous low-velocity layer atop the 410-km discontinuity in the northern Rocky Mountains: Geochemistry, Geophysics, Geosystems, v. 8, no. 10.

Jasbinsek, J. J., Dueker, K. G., and Hansen, S. M., 2010, Characterizing the 410 km discontinuity low-velocity layer beneath the LA RISTRA array in the North American Southwest: Geochemistry, Geophysics, Geosystems, v. 11, no. 3.

Jiang, Q., Qiu, N., and Zhu, C., 2018, Heat flow study of the Emeishan large igneous province region: Implications for the geodynamics of the Emeishan mantle plume: Tectonophysics, v. 724, 11-27.

Katsura, T., Yoneda, A., Yamazaki, D., Yoshino, T., and Ito, E., 2010, Adiabatic temperature profile in the mantle: Physics of the Earth and Planetary Interiors, v. 183, no. 1-2, 212-218.

Keifer, I., and Dueker, K., 2019, Testing the hypothesis that temperature modulates 410 and 660 discontinuity topography beneath the eastern United States: Earth and Planetary Science Letters, v. 524, 115723.

Kennett, B., and Engdahl, E., 1991, Traveltimes for global earthquake location and phase identification: Geophysical Journal International, v. 105, no. 2, 429-465.

Ketcham, R. A., Carter, A., Donelick, R. A., Barbarand, J., and Hurford, A. J., 2007, Improved modeling of fission-track annealing in apatite: American Mineralogist, v. 92, no. 5-6, 799-810.

Ketcham, R. A., Donelick, R. A., and Donelick, M. B., 2000, AFTSolve: A program for multi-kinetic modeling of apatite fission-track data: Geological Materials Research, v. 2, no. 1, 1-32.

Lawrence, D. T., Doyle, M., and Aigner, T., 1990, Stratigraphic Simulation of Sedimentary Basins: Concepts and Calibration (1): Aapg Bulletin, v. 74, no. 3, 273-295.

Leahy, G. M., and Bercovici, D., 2007, On the dynamics of a hydrous melt layer above the transition zone: Journal of Geophysical Research: Solid Earth, v. 112, no. B7.

Lerche, I., Yarzab, R., and Kendall, C. S. C., 1984, Determination of paleoheat flux from vitrinite reflectance data: AAPG Bulletin, v. 68, no. 11, 1704-1717.

Li, H., Zhang, Z., Santosh, M., Lü, L., Han, L., and Liu, W., 2017, Late Permian basalts in the Yanghe area, eastern Sichuan Province, SW China: Implications for the geodynamics of the Emeishan flood basalt province and Permian global mass extinction: Journal of Asian Earth Sciences, v. 134, 293-308.

Lu, Q., Hu, S., Guo, T., and Li, Z., 2005, The background of geothermal field for the formation of abnormal high pressure in northeastern Sichuan basin: Chinese Journal of Geophysics, v. 48, no. 5, 1184-1191.

Ma, M., Zhou, X., Xu, Z., Li, G., Li, Y., and Zhou, Y., 2020, The melt content of the low velocity layer in the eastern South China: Implications for the subduction process of the Western Pacific plate: Physics of the Earth and Planetary Interiors, v. 298, 106321.

Mackenzie, A., and McKenzie, D., 1983, Isomerization and aromatization of hydrocarbons in sedimentary basins formed by extension: Geological Magazine, v. 120, no. 5, 417-470.

Martin, M., 2011, Cutadapt removes adapter sequences from high-throughput sequencing reads: EMBnet. journal, v. 17, no. 1, 10-12.

Mavko, G. M., 1980, Velocity and attenuation in partially molten rocks: Journal of Geophysical Research: Solid Earth, v. 85, no. B10, 5173-5189.

McKenzie, D., 1978, Some remarks on the development of sedimentary basins: Earth and Planetary science letters, v. 40, no. 1, 25-32.

McKenzie, D., 1981, The variation of temperature with time and hydrocarbon maturation in sedimentary basins formed by extension: Earth and Planetary Science Letters, v. 55, no. 1, 87-98.

Mei, S., Bai, W., Hiraga, T., and Kohlstedt, D., 2002, Influence of melt on the creep behavior of olivine–basalt aggregates under hydrous conditions: Earth and Planetary Science Letters, v. 201, no. 3-4, 491-507.

Miall, A. D., 1997, The geology of stratigraphic sequences, Berlin, Springer-Verlag.

Miller, K. G., Mountain, G. S., Browning, J. V., Kominz, M., Sugarman, P. J., Christie-Blick, N., Katz, M. E., and Wright, J. D., 1998, Cenozoic global sea level, sequences, and the New Jersey transect: results from coastal plain and continental slope drilling: Reviews of Geophysics, v. 36, no. 4, 569-601.

Minarik, W. G., and Watson, E. B., 1995, Interconnectivity of carbonate melt at low melt fraction: Earth and Planetary Science Letters, v. 133, no. 3-4, 423-437.

Morra, G., Yuen, D. A., Boschi, L., Chatelain, P., Koumoutsakos, P., and Tackley, P., 2010, The fate of the slabs interacting with a density/viscosity hill in the mid-mantle: Physics of the Earth and Planetary Interiors, v. 180, no. 3-4, 271-282.

Neal, J., and Abreu, V., 2009, Sequence stratigraphy hierarchy and the accommodation succession method: Geology, v. 37, no. 9, 779-782.

Nielsen, S., Clausen, O. R., and McGregor, E., 2017, Basin% Ro: a vitrinite reflectance model derived from basin and laboratory data: Basin Research, v. 29, 515-536.

Nielsen, S. B., 1995, An upper limit to palaeo heat flow: theory and examples from the Danish Central Graben: Tectonophysics, v. 244, no. 1-3, 137-152.

Nielsen, S. B., 1996, Sensitivity analysis in thermal and maturity modelling: Marine and Petroleum Geology, v. 13, no. 4, 415-425.

Nielsen, S. B., and Dahl, B., 1991, Confidence limits on kinetic models of primary cracking and implications for the modelling of hydrocarbon generation: Marine and petroleum geology, v. 8, no. 4, 483-492.

Noether, E., 1918, Invariante Variationsprobleme, Göttingen, Nachr.v. d. Ges. d. Wiss. zu, pp. 235-257.

Pittion, J., and Pradier, B., Reflectance of vitrinite as a control of thermal history of sediments, *in* Proceedings Thermal Modeling in Sedimentary Basins: 1st IFP Exploration Research Conference, Carcans, France, June 3-7, 19851986, Editions Technip, 441.

Plint, A. G., and Nummedal, D., 2000, The falling stage systems tract: recognition and importance in sequence stratigraphic analysis: Geological Society, London, Special Publications, v. 172, no. 1, 1-17.

Posamentier, H., Jervey, M., and Vail, P., 1988, Eustatic controls on clastic deposition I—conceptual framework.

Posamentier, H. W., Allen, G. P., James, D. P., and Tesson, M., 1992, Forced regressions in a sequence stratigraphic framework: concepts, examples, and exploration significance: AAPG bulletin, v. 76, no. 11, 1687-1709.

Poulsen, C. J., Flemings, P. B., Robinson, R. A., and Metzger, J. M., 1998, Three-dimensional stratigraphic evolution of the Miocene Baltimore Canyon region: Implications for eustatic interpretations and the systems tract model: Geological Society of America Bulletin, v. 110, no. 9, 1105-1122.

Press, W. H., Teukolsky, S. A., Vetterling, W. T., and Flannery, B. P., 2007, Numerical recipes 3rd edition: The art of scientific computing, Cambridge university press, pp. 445.

Price, L. C., 1983, Geologic time as a parameter in organic metamorphism and vitrinite reflectance as an absolute paleogeothermometer: Journal of Petroleum Geology, v. 6, no. 1, 5-37.

Prince, G. D., and Burgess, P. M., 2013, Numerical modeling of falling-stage topset aggradation: implications for distinguishing between forced and unforced regressions in the geological record: Journal of Sedimentary Research, v. 83, no. 9, 767-781.

Revenaugh, J., and Sipkin, S., 1994, Seismic evidence for silicate melt atop the 410-km mantle discontinuity: Nature, v. 369, no. 6480, 474.

Richard, G. C., and Bercovici, D., 2009, Water-induced convection in the Earth's mantle transition zone: Journal of Geophysical Research: Solid Earth, v. 114, no. B1.

Ritchie, B. D., Gawthorpe, R. L., and Hardy, S., 2004, Three-dimensional numerical modeling of deltaic depositional sequences 2: influence of local controls: Journal of Sedimentary Research, v. 74, no. 2, 221-238.

Ritter, U., 1984, The influence of time and temperature on vitrinite reflectance: Organic Geochemistry, v. 6, 473-480.

Royden, L., Sclater, J., and Von Herzen, R., 1980, Continental margin subsidence and heat flow: important parameters in formation of petroleum hydrocarbons: AAPG Bulletin, v. 64, no. 2, 173-187.

Sambridge, M., Bodin, T., Gallagher, K., and Tkalčić, H., 2013, Transdimensional inference in the geosciences: Philosophical Transactions of the Royal Society A: Mathematical, Physical and Engineering Sciences, v. 371, no. 1984, 20110547.

Sass, J., Stone, C., and Munroe, R. J., 1984, Thermal conductivity determinations on solid rock—a comparison between a steady-state divided-bar apparatus and a commercial transient line-source device: Journal of Volcanology and Geothermal Research, v. 20, no. 1-2, 145-153.

Schaeffer, A., and Bostock, M., 2010, A low-velocity zone atop the transition zone in northwestern Canada: Journal of Geophysical Research: Solid Earth, v. 115, no. B6.

Schlager, W., 1993, Accommodation and supply—a dual control on stratigraphic sequences: Sedimentary Geology, v. 86, no. 1-2, 111-136.

Schmandt, B., Dueker, K., Hansen, S., Jasbinsek, J. J., and Zhang, Z., 2011, A sporadic low-velocity layer atop the western US mantle transition zone and short-

wavelength variations in transition zone discontinuities: Geochemistry, Geophysics, Geosystems, v. 12, no. 8.

Schroeder, F. W., and Greenlee, S. M., 1993, Testing eustatic curves based on Baltimore Canyon Neogene stratigraphy: An example application of basin-fill simulation: AAPG Bulletin, v. 77, no. 4, 638-656.

Schumm, S., 1993, River response to baselevel change: implications for sequence stratigraphy: The Journal of Geology, v. 101, no. 2, 279-294.

Sclater, J. G., and Christie, P. A., 1980, Continental stretching: An explanation of the post-Mid-Cretaceous subsidence of the central North Sea Basin: Journal of Geophysical Research: Solid Earth, v. 85, no. B7, 3711-3739.

Shen, P., Wang, K., Beltrami, H., and Mareschal, J.-C., 1992, A comparative study of inverse methods for estimating climatic history from borehole temperature data: Global and planetary change, v. 6, no. 2-4, 113-127.

Sloss, L., 1962, Stratigraphic models in exploration: Journal of Sedimentary Research, v. 32, no. 3.

Song, T.-R. A., Helmberger, D. V., and Grand, S. P., 2004, Low-velocity zone atop the 410-km seismic discontinuity in the northwestern United States: Nature, v. 427, no. 6974, 530.

Stach, E., Murchison, D., Taylor, G. H., and Zierke, F., 1982, Stach's textbook of coal petrology, Volume 535, Borntraeger Berlin, pp. 286.

Steckler, M., Reynolds, D., Coakley, B., Swift, B., and Jarrard, R., 1993, Modelling passive margin sequence stratigraphy: Sequence stratigraphy and facies associations, 19-41.

Steckler, M. S., Mountain, G. S., Miller, K. G., and Christie-Blick, N., 1999, Reconstruction of Tertiary progradation and clinoform development on the New Jersey passive margin by 2-D backstripping: Marine Geology, v. 154, no. 1-4, 399-420.

Sun, Y., Hier-Majumder, S., Xu, Y., and Walter, M., 2020, Stability and migration of slab-derived carbonate-rich melts above the transition zone: Earth and Planetary Science Letters, v. 531, 116000.

Sweeney, J. J., and Burnham, A. K., 1990, Evaluation of a simple model of vitrinite reflectance based on chemical kinetics (1): AAPG bulletin, v. 74, no. 10, 1559-1570.

Swenson, J. B., and Muto, T., 2007, Response of coastal plain rivers to falling relative sea-level: allogenic controls on the aggradational phase: Sedimentology, v. 54, no. 1, 207-221.

Takei, Y., 1998, Constitutive mechanical relations of solid-liquid composites in terms of grain-boundary contiguity: Journal of Geophysical Research: Solid Earth, v. 103, no. B8, 18183-18203.

Takei, Y., 2002, Effect of pore geometry on Vp/Vs: From equilibrium geometry to crack: Journal of Geophysical Research: Solid Earth, v. 107, 2043.

Tarantola, A., 2006, Popper, Bayes and the inverse problem: Nature physics, v. 2, no. 8, 492.

Tauzin, B., Debayle, E., and Wittlinger, G., 2010, Seismic evidence for a global low-velocity layer within the Earth's upper mantle: Nature Geoscience, v. 3, no. 10, 718.

Tauzin, B., and Ricard, Y., 2014, Seismically deduced thermodynamics phase diagrams for the mantle transition zone: Earth and Planetary Science Letters, v. 401, 337-346.

Tauzin, B., Van Der Hilst, R. D., Wittlinger, G., and Ricard, Y., 2013, Multiple transition zone seismic discontinuities and low velocity layers below western United States: Journal of Geophysical Research: Solid Earth, v. 118, no. 5, 2307-2322.

Tetzlaff, D. M., 2004, Input uncertainty and conditioning in siliciclastic process modelling: Geological Society, London, Special Publications, v. 239, no. 1, 95-109.

Tetzlaff, D. M., and Harbaugh, J. W., 1989, Simulating clastic sedimentation.

Thomson, A. R., Walter, M. J., Kohn, S. C., and Brooker, R. A., 2016, Slab melting as a barrier to deep carbon subduction: Nature, v. 529, no. 7584, 76.

Tissot, B., Pelet, R., and Ungerer, P., 1987, Thermal history of sedimentary basins, maturation indices, and kinetics of oil and gas generation: AAPG bulletin, v. 71, no. 12, 1445-1466.

Tissot, B., and Welte, D., 1984, Petroleum Formation and Occurrence, Springer, Berlin, pp. 699.

Uličný, D., Nichols, G., and Waltham, D., 2002, Role of initial depth at basin margins in sequence architecture: field examples and computer models: Basin Research, v. 14, no. 3, 347-360.

Uysal, I. T., Glikson, M., Golding, S. D., and Audsley, F., 2000, The thermal history of the Bowen Basin, Queensland, Australia: vitrinite reflectance and clay mineralogy of Late Permian coal measures: Tectonophysics, v. 323, no. 1-2, 105-129.

Vail, P. R., 1977, Seismic stratigraphy and global changes of sea level: Bull. Am. Assoc. Petrol. Geol., Mem., v. 26, 49-212.

Van Wagoner, J. C., Mitchum, R., Campion, K., and Rahmanian, V., 1990, Siliciclastic sequence stratigraphy in well logs, cores, and outcrops: concepts for high-resolution correlation of time and facies.

Vasseur, G., Brigaud, F., and Demongodin, L., 1995, Thermal conductivity estimation in sedimentary basins: Tectonophysics, v. 244, no. 1-3, 167-174.

Vinnik, L., and Farra, V., 2007, Low S velocity atop the 410-km discontinuity and mantle plumes: Earth and Planetary Science Letters, v. 262, no. 3-4, 398-412.

Vinnik, L., Ren, Y., Stutzmann, E., Farra, V., and Kiselev, S., 2010, Observations of S410p and S350p phases at seismograph stations in California: Journal of Geophysical Research: Solid Earth, v. 115, no. B5.

von Bargen, N., and Waff, H. S., 1986, Permeabilities, interfacial areas and curvatures of partially molten systems: results of numerical computations of equilibrium microstructures: Journal of Geophysical Research: Solid Earth, v. 91, no. B9, 9261-9276.

Waltham, D., and Gröcke, D. R., 2006, Non-uniqueness and interpretation of the seawater 87Sr/86Sr curve: Geochimica et Cosmochimica Acta, v. 70, no. 2, 384-394.

Waltham, D., and Hardy, S., 1995, The velocity description of deformation. Paper 1: theory: Marine and petroleum geology, v. 12, no. 2, 153-163.

Waltham, D., Udofia, M., and Nichols, G., 2003, Non-unique sequence stratigraphic architectures, [online] Available from: http://basinmodelling.geo.uu.nl/pages/walthab.htm (Accessed 11 Sep, 2019).

Wang, J., and Zabaras, N., 2004, Hierarchical Bayesian models for inverse problems in heat conduction: Inverse Problems, v. 21, no. 1, 183.

Waples, D. W., 1980, Time and temperature in petroleum formation: application of Lopatin's method to petroleum exploration: AAPG bulletin, v. 64, no. 6, 916-926.

Waples, D. W., 1994, Maturity Modeling: Thermal Indicators, Hydrocarbon Generation, and Oil Cracking: Chapter 17: Part IV. Identification and Characterization, 285-306.

Welte, D. H., Horsfield, B., and Baker, D. R., 2012, Thermal history of sedimentary basin, Petroleum and basin evolution: insights from petroleum geochemistry, geology and basin modeling: Berlin Heidelberg, Springer -Verlag, pp. 96-115.

Wijns, C., Poulet, T., Boschetti, F., Dyt, C., and Griffiths, C., 2004, Interactive inverse methodology applied to stratigraphic forward modelling: Geological Society, London, Special Publications, v. 239, no. 1, 147-156.

Willett, S. D., 1997, Inverse modeling of annealing of fission tracks in apatite; 1, A controlled random search method: American Journal of Science, v. 297, no. 10, 939-969.

Wimert, J., and Hier-Majumder, S., 2012, A three-dimensional microgeodynamic model of melt geometry in the Earth's deep interior: Journal of Geophysical Research: Solid Earth, v. 117, no. B4.

Xiao, J., and Waltham, D., 2019, Non-uniqueness and symmetry in stratigraphic interpretations: A quantitative approach for determining stratal controls: Sedimentology, v. 66, no. 5, 1700-1715.

Xu, M., ZHU, C. Q., TIAN, Y. T., Rao, S., and HU, S. B., 2011, Borehole temperature logging and characteristics of subsurface temperature in the Sichuan Basin: Chinese Journal of Geophysics, v. 54, no. 2, 224-233.

Xu, W., Lithgow-Bertelloni, C., Stixrude, L., and Ritsema, J., 2008, The effect of bulk composition and temperature on mantle seismic structure: Earth and Planetary Science Letters, v. 275, no. 1-2, 70-79.

Xu, Y.-G., He, B., Chung, S.-L., Menzies, M. A., and Frey, F. A., 2004, Geologic, geochemical, and geophysical consequences of plume involvement in the Emeishan flood-basalt province: Geology, v. 32, no. 10, 917-920.

Yoshino, T., Takei, Y., Wark, D. A., and Watson, E. B., 2005, Grain boundary wetness of texturally equilibrated rocks, with implications for seismic properties of the upper mantle: Journal of Geophysical Research: Solid Earth, v. 110, no. B8.

Yuan, Y., Sun, D., and Li, S., 2013, Caledonian erosion thickness reconstruction in the Sichuan Basin.

Zhang, Y., Luo, Y., and Yang, C., 1988, The Panxi Rift, Beijing, China, Geological Publishing House.

Zhang, Z., Dueker, K. G., and Huang, H.-H., 2018, Ps mantle transition zone imaging beneath the Colorado Rocky Mountains: Evidence for an upwelling hydrous mantle: Earth and Planetary Science Letters, v. 492, 197-205.

Zhang, Z., Mahoney, J. J., Mao, J., and Wang, F., 2006, Geochemistry of picritic and associated basalt flows of the western Emeishan flood basalt province, China: Journal of Petrology, v. 47, no. 10, 1997-2019.

Zhao, M.-W., Behr, H.-J., Ahrendt, H., Wemmer, K., Ren, Z.-L., and Zhao, Z.-Y., 1996, Thermal and tectonic history of the Ordos Basin, China: evidence from apatite fission track analysis, vitrinite reflectance, and K-Ar dating: AAPG bulletin, v. 80, no. 7, 1110-1133.

Zhu, C., Xu, M., Shan, J., Yuan, Y., Zhao, Y., and Hu, S., 2009, Quantifying the denudations of major tectonic events in Sichuan basin: Constrained by the paleothermal records: Geology in China, v. 36, no. 6, 1268-1277 (in Chinese with English abstract).

Zhu, C., Xu, M., Yuan, Y., Zhao, Y., Shan, J., He, Z., Tian, Y., and Hu, S., 2010, Palaeogeothermal response and record of the effusing of Emeishan basalts in the Sichuan basin: Chinese Science Bulletin, v. 55, no. 10, 949-956.